Ferromagnetic (Ga,Mn)As Layers and Nanostructures:

Control of Magnetic Anisotropy by Strain Engineering

Dissertation

zur Erlangung des
naturwissenschaftlichen Doktorgrades
der Julius-Maximilians-Universität Würzburg

vorgelegt von
Jan Wenisch
aus Würzburg

Würzburg 2008

Eingereicht am:

bei der Fakultät für Physik und Astronomie

Gutachter der Dissertation:

1. Gutachter: Prof. Dr. K. Brunner

2. Gutachter: Prof. Dr. R. Claessen

3. Gutachter: Prof. Dr. B. Trauzettel

Prüfer im Promotionskolloquium:

1. Prüfer: Prof. Dr. K. Brunner

2. Prüfer: Prof. Dr. R. Claessen

3. Prüfer: Prof. Dr. B. Trauzettel

Tag des Promotionskolloquiums:

Doktorurkunde ausgehändigt am:

Contents

Zusammenfassung

Ferromagnetische Halbleiter (ferromagnetic semiconductors, FS) versprechen die Integration magnetischer Datenspeicherung und Datenverarbeitung auf Halbleiterbasis innerhalb eines einzigen Materialsystems. Das Modellsystem für diese Klasse von Materialien ist der FS (Ga,Mn)As. Als solches ist dieses Modellsystem in den letzten Jahren in den Mittelpunkt intensiver Forschungsbemühungen gerückt. Die Kopplung seiner magnetischen und halbleitenden Eigenschaften durch Spin-Bahn Wechselwirkung ist die Ursache vieler neuartiger Phänomene mit breit gefächertem Anwendungspotential im Bereich der Spintronik. Seit der ersten ausführlichen Beschreibung des Materialsystems 1998 durch H. Ohno [Ohno 98] ist das Wissen um seine experimentellen und theoretischen Aspekte rapide gewachsen. Das Ziel dieser Arbeit ist es, eine umfassende Einführung in die Eigenschaften dieses Materialsystems und den technologischen Stand der Molekularstrahlepitaxie (molecular beam epitaxy, MBE), die dazu dient (Ga,Mn)As Schichten höchster Qualität herzustellen, zu liefern. Der experimentelle Teil dieser Arbeit konzentriert sich auf eine Technik, mit der es möglich ist, lokale Kontrolle über die magnetische Anisotropie des Materials mittels lithographisch bedingter Veränderung der Verspannung zu erreichen.

Das (Ga,Mn)As Materialsystem ist eine neue Anwendung der MBE Technologie, die aus den späten 1960er Jahren stammt. Das erfolgreiche epitaktische Wachstum von Halbleitern erfordert die präzise Kontrolle mehrerer Wachstumsparameter. Dazu zählen die Temperatur der Effusionszellen, die Wachstumstemperatur, das Verhältnis der Materialflüsse sowie die Wachstumsrate. Wegen seiner niedrigen Löslichkeit unter thermischen Gleichgewichtsbedingungen muss das Wachstum von (Ga,Mn)As bei sehr niedrigen Temperaturen (270 °C verglichen mit 580 °C für GaAs) stattfinden. Zu den wichtigsten Charakterisierungsmethoden des epitaktischen Wachstums zählen in-situ Elektronenstrahlbeugung (reflection high energy electron diffraction, RHEED) und ex-situ hochauflösende Röntgenstrahlbeugung (high resolution x-ray diffraction, HRXRD). Ein weiteres hilfreiches Werkzeug ist die Nomarksi-Mikroskopie zur Beurteilung der Qualität des Wachstums und einer Reihe von Oberflächendefekten, die durch den Wachstumsprozess bedingt sind.

(Ga,Mn)As wird typischerweise unter kompressiver Verspannung auf einem GaAs Substrat gewachsen. In der Vergangenheit lag der Schwerpunkt der Untersuchungen auf ausgedehnten Schichten mit vergleichsweise einfacher Verspannung. Obwohl schon seit einiger Zeit bekannt ist, dass die Verspannung des Gitters eine der treibenden Kräfte ist, die das Verhalten der komplexen magnetischen Anisotropie von (Ga,Mn)As bestimmen [Diet 01, Abol 01], ist die detaillierte Untersuchung der Bedeutung dieses Parameters eine neue Entwicklung. Aktuelle Forschung, wie die Technik, die im Mittelpunkt dieser Arbeit steht, macht sich anisotrope Verspannungen zunutze, um Einfluss auf die magnetische Anisotropie zu nehmen. Experimentell wird anisotrope

Verspannung entweder durch lithographische Strukturierung (wie in dieser Arbeit beschrieben), oder durch piezoelektrische Kräfte erzeugt [Over 08]. In jedem Fall ist es von zentraler Bedeutung, zu verstehen, wie die Verspannung im Inneren des Materials verteilt ist und wie Strukturierung oder mechanische Kräfte die Verspannung des Kristalls beeinflussen. Um diese Aufgabe zu Lösen, haben wir eine dreidimensionale finite Elemente Simulation entwickelt. Die Software ist in der Lage, die Elastizitätsgleichungen der klassischen Kontinuumsmechanik auf einem 3D Gitter in einem beliebig geometrisch definierten Gebilde zu lösen. Mit diesem Werkzeug ist es möglich, die Verspannung in komplexen Strukturen zu simulieren und diese Strukturen im Hinblick auf Parameter wie Ätztiefe, Aspektverhältnisse und Ausrichtung zu den Kristallachsen zu optimieren. Eine Struktur, die einfach herzustellen ist und dabei eine besonders große Anisotropie der Gitterverspannung in zwei orthogonalen Kristallrichtungen aufweist, ist ein schmaler aber sehr langer Streifen. In seiner einfachsten Form wird die anisotrope Verspannung durch selektive Relaxation des komprimierten Gitters der(Ga,Mn)As Schicht senkrecht zur Streifenachse erreicht. Ein komplizierter Schichtaufbau entsteht durch das Einfügen einer hoch verspannten (In,Ga)As Schicht unter dem (Ga,Mn)As. Mittels dieser Stressorschicht ist es möglich, in der (Ga,Mn)As Schicht tensile Verspannung senkrecht zur Streifenrichtung zu induzieren. Entlang des Streifens bleibt der pseudomorphe (kompressiv verspannte) Zustand bestehen.

Die Genauigkeit der Vorhersagen der Verspannungssimulation wurde mit zwei hochauflösenden Röntgenbeugungsmethoden an verschiedenen Streifenfeldern bestätigt. Es hat sich gezeigt, dass die Streifen eine deutliche Veränderung der magnetischen Konfiguration als Reaktion auf die durch die Strukturierung hervorgerufene anisotrope Verspannung zeigen. Sowohl SQUID als auch Magnetotransport Messungen offenbaren, dass bei [100] orientierten Streifen die in-plane biaxiale Anisotropie der ursprünglichen Schicht durch eine einzige globale weiche Achse entlang der Streifenrichtung ersetzt wird. In Streifen, die entlang der [1$\bar{1}$0] Richtung orientiert sind, beobachten wir, dass die weiche Achse von ihrer ursprünglichen Position in der Mutterschicht in Richtung der Streifenachse rotiert. Dieses Verhalten wird durch Ausheizen der Probe für mehrere Stunden zur Erhöhung der Ladungsträgerdichte weiter verstärkt. Durch Vergleich zwischen verschiedenen Streifen sowie der Berechnung der zu erwartenden Größenordnung kann Formanisotropie als nennenswerter Beitrag zur magnetischen Anisotropie von (Ga,Mn)As ausgeschlossen werden. Das beobachtete Verhalten für beide Streifenrichtungen kann auch theoretisch nachvollzogen werden. Die magnetische Anisotropie kann berechnet werden indem die in einem $\mathbf{k} \cdot \mathbf{p}$ Formalismus berechneten Valenzbänder (unter Berücksichtigung von Spin-Bahn Wechselwirkung sowie der Verspannung) im 3D k-Raum bis zur Fermienergie aufgefüllt werden. Wenn man die resultierende Energielandschaft für einen entlang [100] orientierten Streifen für zunehmende Verspannungszustände aufträgt, zeigt sich, dass die weiche Achse senkrecht zur Streifenrichtung durch eine harte Achse ersetzt wird. der Übergang zu einer einzigen unaxialen weichen Achse ist abgeschlossen, wenn etwa 50% der kompressiven Gitterverspannung relaxiert ist. In allen gezeigten Streifenstrukturen wird dieser Wert überschritten. Wir präsentieren ebenfalls ein einfaches Modell, das qualitativ das Anisotropieverhalten beider Streifenrichtungen beschreibt. Es basiert auf der Berechnung der magnetostatischen Energie [Papp 07b], die modifiziert wird, um einen zusätzlichen Verspannungsterm zu berücksichtigen.

Der abschließende Teil dieser Arbeit zeigt ein Beispiel für eine Anwendung der

Anisotropiekontrolle in (Ga,Mn)As in der From eines nichtflüchtigen Speicherelements, das ausschließlich auf Halbleiterbasis operiert. Zwei orthogonale Streifen werden über eine Verengung and einer Ecke miteinander verbunden. Vier unterschiedliche Magnetisierungszustände können über die Kontrolle der Ausrichtung der Magnetisierung in den Streifen 'geschrieben' werden. Das Auslesen des Speichers erfolgt durch das Messen des Spannungsabfalls über die Verengung. Höher entwickelte Versionen dieses Bauteils sind bereits hergestellt und werden untersucht. Wir erwarten, dass die Technik der lokalen Anisotropiekontrolle mittels lithographisch induzierter Relaxation ein wertvolles Werkzeug in der Entwicklung zukünftiger Generationen von Halbleiterbauteilen sowie der Erforschung der Grundlagen des (Ga,Mn)As Materialsystems darstellen wird.

Summary

The great promise of ferromagnetic semiconductors (FS) is the integration of magnetic memory functionality and semiconductor information processing into one material system. The model system for this class of materials is the FS (Ga,Mn)As. As such, it has become the focus of intense research over the past years. The spin-orbit mediated coupling of magnetic and semiconductor properties in this material gives rise to a large number of phenomena with a vast scope of possible applications in the field of spintronic devices. Ever since the first thorough description of the material system by H. Ohno in 1998 [Ohno 98], the understanding of both its experimental and theoretical aspects has grown rapidly. The objective of this thesis is to give a comprehensive introduction into the properties of the material system and the current technological state of molecular beam epitaxy (MBE) by which highest quality (Ga,Mn)As layers are produced. The experimental part of this work focuses on a technique to attain local control over the magnetic anisotropy of the material by means of lithographically induced strain engineering.

The technology of MBE predates its use in the (Ga,Mn)As material system and originates in the late 1960's. Successful epitaxial growth of semiconductors requires precise control and understanding of several critical growth parameters such as the source cell temperature, the growth temperature, the ratio of the material fluxes, and the growth rate. Due to its low solubility at thermal equilibrium, the growth of (Ga,Mn)As has to take place at very low temperatures (270 °C compared to 580 °C for GaAs). The characterization methods most closely related to epitaxial growth are in-situ reflection high energy electron diffraction (RHEED) and ex-situ high resolution x-ray diffraction (HRXRD). Nomarski microscopy is another helpful tool in identifying a number of surface defects related to the growth procedure and gauging the quality of epitaxial layers.

(Ga,Mn)As is typically grown on GaAs wafers, which puts the material under compressive strain. Traditionally, a lot of research on this material was focused on extensive layers with a comparatively simple strain distribution. Although it has been known for some time, that lattice strain is one of the driving forces behind the complex, anisotropic magnetic behavior of (Ga,Mn)As [Diet 01, Abol 01], a detailed investigation on its influence is only a recent development. Current research, such as the technique which is the focus of this thesis, takes advantage of anisotropic strain to influence the magnetic anisotropy. Experimentally, anisotropic strain is either induced by lithographic pattering (the approach taken in this work) or by piezoelectrical forces [Over 08]. In either case, it is imperative to understand how the strain in the material is distributed and how patterning or mechanical forces on the crystal affect the strain. For this task, we have developed a three-dimensional finite element simulation technique. The simulation software is capable of solving the elasticity equations of

classical continuum mechanics on a 3D grid in an arbitrarily defined geometry. With this tool we can predict the strain in complex structures and optimize them with respect to parameters such as etch depth, aspect ratios, and alignment with respect to crystal axes. One structure which is easy to fabricate and offers a large anisotropy in lattice strain for two orthogonal crystal directions is a narrow but very long stripe. In its most simple form, the anisotropic strain is caused by selective relaxation of the compressive strain of the (Ga,Mn)As layer perpendicular to the stripe axis. A more sophisticated setup is the inclusion of a highly strained (In,Ga)As layer below the (Ga,Mn)As. With this stressor layer it becomes possible to induce tensile strain perpendicular to the stripe direction into the (Ga,Mn)As layer, while still retaining the pseudomorphic (compressively strained) condition along the stripe.

The strain predictions of the finite element simulations are verified to be accurate by two HRXRD techniques on various stripe arrays. Magnetically, the stripes show a very clear response to the patterning induced strain anisotropy. Both SQUID and magnetotransport measurements reveal a replacement of the in-plane biaxial anisotropy of the as-grown layer by a single global uniaxial easy axis along the stripe direction for [100] oriented stripes. For stripes oriented along the [1$\bar{1}$0] direction, the easy axis is tilted away from its original position in the parent layer towards the stripe direction. This behavior is strengthened by annealing the sample for several hours to increase the carrier concentration. By comparison between different stripes as well as calculating its expected contribution, we can rule out shape anisotropy as a significant force in the anisotropy behavior in (Ga,Mn)As. The observations for both stripe directions can also be explained theoretically. After calculating the band structure in a $\mathbf{k} \cdot \mathbf{p}$ formalism (taking into account the spin-orbit coupling and strain), it is possible to determine the magnetic anisotropy by filling up all available bands in the 3D k-space up to the Fermi energy. When the resulting energy landscape for a [100] oriented stripe is plotted for different sets of increasing strain values, we observe that the easy axis perpendicular to the stripe direction is replaced by a hard axis. A single uniaxial easy axis appears when around 50% of the compressive lattice strain is relaxed, which is easily achieved in all the presented stripe structures. We also present a simple model which qualitatively describes the anisotropy behavior for both stripe alignments. The model is based on magnetostatic energy calculations [Papp 07b], modified to take an additional strain term into account.

The final section of this thesis shows an example of an application of engineered anisotropies in (Ga,Mn)As as a non-volatile all-semiconductor memory storage device. Two orthogonal nanobars are connected via a narrow constriction. Four different magnetization states can be 'written' in the form of magnetization alignment in the bars. Readout of the device occurs by measuring the voltage drop over the constriction. More sophisticated versions of this device are under investigation and we expect that the technique of lithographically engineered strain relaxation will prove to be a very valuable tool for future device applications as well as fundamental research in the (Ga,Mn)As material system.

Chapter 1

Introduction

The event considered to be the birth of spintronics was the discovery of the giant magnetoresistance (GMR) effect in 1988 [Baib 88], a feat honored by the award of the Nobel Prize in Physics in 2007. Since then, magnetoelectronic components with functionalities based on the magnetic properties of the device have come to play an integral role in contemporary mainstream and commercially relevant electronics, for example with the introduction of the first GMR based hard drive read head by IBM in 1997 [Thei 03]. A very recent development in spin-electronics is the magnetoresistive random access memory (MRAM), which realizes non-volatile data storage (data is not lost when not powered) [Aker 05]. This new technology has the potential to equal commonly used volatile random access memory (RAM) in speed and capacity, allowing for computers that could be turned on and off almost instantly, bypassing the slow start-up and shutdown procedure. However, MRAM storage devices make use of metallic magnetic elements to store the data, while semiconductor devices are used to process the information.

The vast potential of bridging this gap and uniting data processing, storage, logic operations, and information communication within one material technology has been highlighted in a recent review article [Awsc 07]. Several advantages speak for the development of a hybrid spintronic device. Conventional information processing devices operate by the controlled motion of small pools of charge, where the difference between '0' and '1' is defined by the location of a small quantity of charge. To switch between the two states, the barrier separating the states must be overcome. Information encoded in the electron spin orientation, rather than the position of a pool of charge is not subject to this switching energy. Only a small magnetic field needs to be applied to rotate the orientation of the spins, resulting in a reduction of the energy required in the operation of the device.

Operation speed is another essential concern for next-generation information processing devices. In charge based devices, the processing speed is limited by the capacitance of the device and the drive current. In a semiconductor spintronic device on the other hand, the speed limitations are given by the typical precession frequencies of electron spins in the range form GHz to THz.

A new class of materials, ferromagnetic semiconductors (FS), promises not only to realize these advantages, but also to open the door to a plethora of novel effects with possible device applications. The prototypical FS, on which has been the focus of spintronic research over the past years is (Ga,Mn)As. The material is obtained by doping of

the standard III-V semiconductor GaAs with magnetic Mn acceptors [Ohno 98]. The strong spin-orbit mediated coupling of magnetic and semiconducting properties in this material [Diet 00] gives rise to many novel transport-related phenomena. Previously reported device concepts include strong anisotropic magnetoresistance (AMR) [Baxt 02], planar Hall effect [Tang 03], tunneling AMR (TAMR) [Goul 04, Rüst 05, Papp 06] and Coulomb blockade AMR [Wund 06].

To date, the low ferromagnetic transition temperature limits the use of FS to laboratory applications. For (Ga,Mn)As, the highest obtained Curie temperature is 180 K [Olej 08]. Even though the Curie temperature in this material may never reach room temperature, the insight gained about the aforementioned phenomena is expected to apply to any FS material with strong spin-orbit coupling. Promising material research is ongoing worldwide in the search for alternate room temperature FS.

Most previous demonstrations have been based on structures that have the same magnetic properties, inherited from the unstructured (Ga,Mn)As layer, throughout the device. Recent improvements in lithographic capabilities have opened the way for nanoscale structural patterning of (Ga,Mn)As layers. With this achievement, it has become possible to access locally induced strain relaxation as a means of influencing the magnetic anisotropy properties of the material. This greatly enhances the scope of possible device paradigms, as it allows for devices where the functional element involves transport between regions with different, independently engineered magnetic anisotropy properties.

The objective of this thesis is twofold. The main focus lies on presenting a comprehensive study on the technique of local anisotropy control by strain engineering. Also, the manufacturing of (Ga,Mn)As samples by molecular beam epitaxy (MBE) will be described in detail, including a discussion of all factors which need to be considered in the epitaxial growth of this material system. The outline of this thesis is as follows.

Chapter 2   encompasses a general introduction into the (Ga,Mn)As material system, beginning with the basic concepts of doping and growth-induced lattice strain. The occurrence of ferromagnetism and the magnetic anisotropy properties are explained. Furthermore, an overview of the factors playing a role in $\mathbf{k} \cdot \mathbf{p}$ band structure calculations in this material is provided. The chapter closes with a remark on the influence of annealing on the material system.

Chapter 3   focuses on the epitaxial growth of (Ga,Mn)As, with a detailed examination of the relevant growth parameters and their influence on the material properties. The most important in-situ (RHEED) and ex-situ (HRXRD) characterization techniques are addressed.

Chapter 4   supplies the groundwork needed to understand the structural effect of lithographic nanopatterning of (Ga,Mn)As layers on the crystal. A set of formulas is derived for a 3D finite element simulation. Using the results of such simulations, we examine the influence of several geometrical parameters on the strain relaxation of a stripe structure, either aligned along the [100] or [$1\bar{1}0$] crystal direction.

Chapter 5   contains the characterization of a series of stripe samples, beginning with the structural characterization by HRXRD and GIXRD. The magnetic properties are

investigated with SQUID and magnetotransport measurements, revealing the large impact of anisotropic strain on the magnetic properties of the stripes. Finally, we present a theoretical model based on $\mathbf{k} \cdot \mathbf{p}$ calculations and magnetostatic energy considerations to explain the influence of strain on the magnetic anisotropy of (Ga,Mn)As.

Chapter 6   closes the gap between fundamental studies on strain relaxation in simple stripe structures and device application. Two orthogonal nanobars are electrically coupled via a constriction. The resulting device can act as a nonvolatile memory storage by making use of the relative magnetization states in the stripes. We investigate the strain distribution in the constriction region with simulations and discuss its influence on the constriction properties.

Chapter 2

The (Ga,Mn)As Material System

The ternary material (Ga,Mn)As belongs to the class of so called dilute magnetic semiconductors (DMS). This term is derived from the nature of magnetism in these materials, which will be discussed shortly. Fabrication of this material is done by molecular beam epitaxy at a temperature significantly lower (between 230 °C and 270 °C) than conventional GaAs MBE at around 600 °C. During this low-temperature growth, typically 2–6% of Mn atoms are incorporated into the GaAs lattice, retaining the zinc blende structure of GaAs. This process can happen in two distinct ways. The majority of Mn atoms is incorporated substitutionally into the GaAs lattice, as shown in Fig. 2.1, replacing a Ga atom at its lattice site. Since Mn is not isovalent with Ga, these atoms act as acceptors by contributing one hole to the GaAs valence band, giving the material its p-type doping character. A smaller fraction of atoms is incorporated at interstitial lattice sites. In contrast to the substitutional atoms, they act as double donors which compensate some of the carriers introduced by the majority p-type doping. A very small number may also incorporate as antisites, replacing an As atom and forming another double donor. However, these atoms play no significant role in determining the (Ga,Mn)As properties.
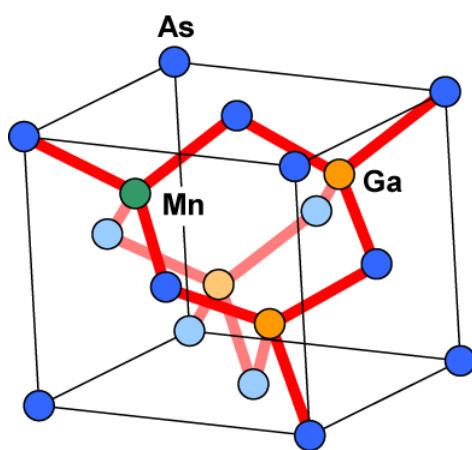

Figure 2.1: Zinc blende GaAs lattice with a substitutional Mn atom at a Ga lattice site.

Adding Manganese to the GaAs crystal increases the lattice constant a of the resulting material due to the larger atomic radius of Mn compared to Ga. The increase
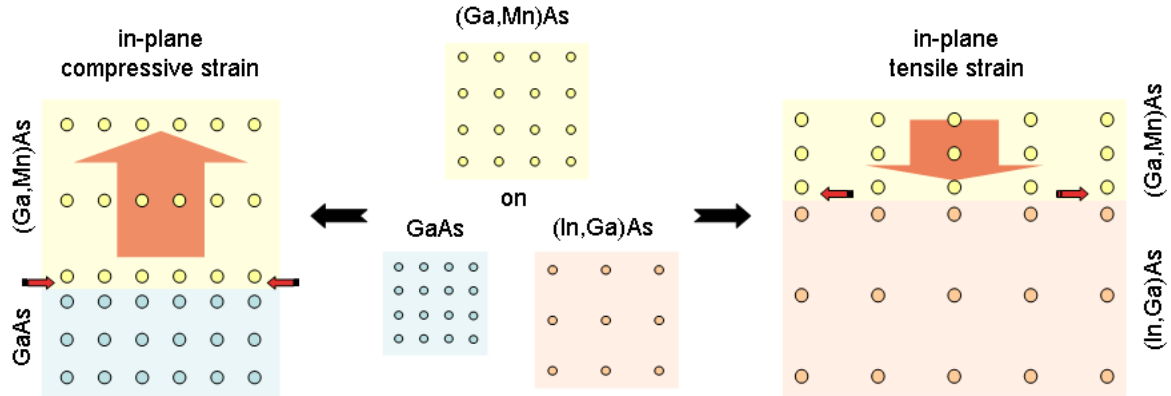
Figure 2.2: The exitaxial growth of (Ga,Mn)As on GaAs (left side) or (In,Ga)As (right side) leads to either compressive or tensile strain in the plane of the layer, as the (Ga,Mn)As grows pseudomorphically on the respective substrate.

in lattice constant due to the admixture of Mn is proportional to the amount of Mn incorporated [Scho 01]. The difference in lattice constant between two layers is given by the lattice mismatch f, defined as

$$f = \frac{a_{layer} - a_{substrate}}{a_{substrate}}. \tag{2.1}$$

During epitaxial growth, the first monolayers of any material are lattice-matched (pseudomorphic) to the underlying crystal structure. As the thickness of the growing layer increases, strain energy is accumulated as more and more deposited material is added to the lattice-matched crystal. At some mismatch-dependent critical layer thickness, strain relaxation begins with the formation of lattice defects, which leads to degradation and roughening of the growth front as the lattice constant of subsequent layers approaches the unstrained value of the bulk material. The most general definition of strain is the relative change in one dimension of a sample, $e = \Delta l / l$. For the case of epitaxial layers, we define the strain as the difference in lattice constant of a strained layer to the bulk lattice constant of the unstrained material:

$$e = \frac{a_{strained} - a_{relaxed}}{a_{relaxed}}. \tag{2.2}$$

From this equation we can immediately see, that a value of $e < 0$ indicates compressed material, while $e > 0$ results from a material under tensile strain. This growth-induced strain present in (Ga,Mn)As can significantly influence its magnetic properties and can act in two different ways, as illustrated in Fig. 2.2:

- Compressive strain in the plane of the layer is the result of growing (Ga,Mn)As on a substrate with a smaller lattice constant than the bulk value of the (Ga,Mn)As layer, usually GaAs.

- Tensile strain is caused by growth of (Ga,Mn)As on a substrate with a larger lattice constant. Examples are InP or thick, relaxed (In,Ga)As buffers.

A deformation Δd in one direction of the sample due to strain leads to a corresponding deformation Δl in the perpendicular direction. The magnitude of this effect is given by the Poisson ratio ν of the material, which is defined by

$$\nu = \frac{\Delta d/d}{\Delta l/l}. \tag{2.3}$$

Here, d and l correspond to the width and length, that an arbitrary volume of material would assume in the absence of strain. The Poisson ratio for GaAs is $\nu = 0.31$, which will also be used for all other layers in this thesis containing only small percentages of incorporated atoms. It is important to keep in mind, that the above definition is only true for deformations in $\langle 100 \rangle$ directions. A more general definition will be introduced in Section 5.1.1.

2.1 Ferromagnetism in (Ga,Mn)As

As mentioned earlier, the primary incorporation mechanism for Mn into a GaAs crystal is the substitution of a Ga atom. In this case, the Mn atoms adopt a Mn^{2+} valence configuration which leads to localized magnetic moments of spin $S = 5/2$. Two such localized moments are coupled via an antiferromagnetic exchange mechanism. However, it is a rather weak coupling due to the high dilution of the Mn dopants and leads to little or no magnetic ordering on its own.

More important is the coupling between the localized moments and the holes provided by the shallow Mn acceptors. This coupling is also antiferromagnetic, but the valence band holes are not strongly localized on a single impurity and tend to spread out over many lattice sites. As a consequence, they can interact with a large number of Mn ions which leads to an alignment of the Mn magnetic moments within the extend of the hole spin wavefunction. This alignment of the magnetic moments is antiparallel with respect to the spin holes and thus parallel to each other, creating regions of ferromagnetic ordering. The transition between isolated regions of aligned domains and long range ferromagnetic ordering takes place around a Mn concentration of 0.5%, when a sufficient number of carriers (holes) is present to mediate the alignment over large distances.

The result of the above leads to an important implication for the Curie temperature, below which ferromagnetic ordering is observed. T_C is not only dependent on the absolute concentration of Mn. The method of incorporation also plays a critical role. In particular, the Curie temperature is given in the Zener model by [Diet 00]:

$$T_C = C N_{Mn} p^{1/3}. \tag{2.4}$$

C is a material constant, N_{Mn} the substitutional Mn concentration and p the hole carrier concentration. To reach a high value of T_C, it is therefore not only necessary to optimize the amount of substitutional Mn, but also maximize the free hole population. Interstitial Mn atom double donor states resulting from imperfect growth thus do not only subtract from the amount of substitutional atoms, but also compensate holes which are critical for the mediation of the ferromagnetic ordering.

2.2   Band Structure Calculations in (Ga,Mn)As

The most widely used theoretical approach to describe ferromagnetism in zinc blende magnetic semiconductors in general and (Ga,Mn)As in particular is the p-d mean field Zener model description of carrier mediated ferromagnetism. This model was originally proposed by T. Dietl in 2000 [Diet 00] and subsequently developed more thoroughly by [Diet 01] and [Abol 01]. A detailed treatise on this subject can also be found in [Schm 06].

We are mainly interested in the valence band structure around the Γ-point ($\mathbf{k} = 0$), which is why we will use a $\mathbf{k} \cdot \mathbf{p}$ technique, which is essentially a theory, that is exact to the order of k^2 near Γ [Lutt 55]. All included effects need to be expressed in the form of Hamiltonians, which we will discuss individually in the following.

Kohn-Luttinger Hamiltonian

The first contribution is the band structure of pure GaAs, without the inclusion of Mn atoms into the lattice. Its valence band structure for the first six valence bands is given by the 6×6 Kohn-Luttinger Hamiltonian H_{KL}, whose full form is provided in Appendix A.1. It contains the three phenomenological Kohn-Luttinger parameters, γ_1, γ_2, and γ_3. Their values are accurately known for common semiconductors and in GaAs are $(\gamma_1, \gamma_2, \gamma_3) = (6.85, 2.1, 2.9)$[Vurg 01]. H_{KL} takes into account the spin-orbit interaction H_{so} for the orbital angular momentum $\mathbf{L}$ and the spin $\mathbf{S}$. This interaction can be expressed as

$$H_{so} = \lambda \, \mathbf{L} \cdot \mathbf{S}, \qquad\qquad (2.5)$$

where λ is the spin-orbit coupling. The eigenfunctions of H_{so} are eigenstates of the total angular momentum $\mathbf{J} = \mathbf{L} + \mathbf{S}$. For the quantum numbers $l = 1$ and $s = \frac{1}{2}$, j can take the values $\frac{3}{2}$ and $\frac{1}{2}$. At the zone center, the spin-orbit interaction splits these two states by a factor $\Delta_{so} = \frac{3\lambda}{2}$, which is determined experimentally. The widely accepted value for the split-off energy gap in GaAs is $\Delta_{so} = 0.341$ eV[Vurg 01]. This splitting leaves the fourfold degenerate heavy-hole (hh) plus light-hole (lh) bands of Γ_8 symmetry with $j = \frac{3}{2}$ and a doubly degenerate split-off (so) band of Γ_7 symmetry with $j = \frac{1}{2}$. The pure Kohn-Luttinger band structure dispersion along k_x for the first six valence bands of GaAs is shown in Fig. 2.3 (a).

pd Exchange Interaction

With the incorporation of Mn atoms into the lattice, we need to consider the exchange interaction between the valence band holes and the localized moments of the Mn^{2+} acceptors. We assume that the effect of the 5d-electrons in the Mn core on the holes can be approximated by an effective field which is proportional to the magnetization $\mathbf{M}$ and couples to the spin angular momentum $\mathbf{S}$ of the valence band holes:

$$H_{pd} = 6B_g \, \mathbf{M} \cdot \mathbf{S} \qquad\qquad (2.6)$$

The coupling constant B_g characterizes the magnitude of the band splitting due to the pd interaction. It has a positive value for antiferromagnetic coupling, which is the case in (Ga,Mn)As, and a negative value for ferromagnetic coupling. In this work we
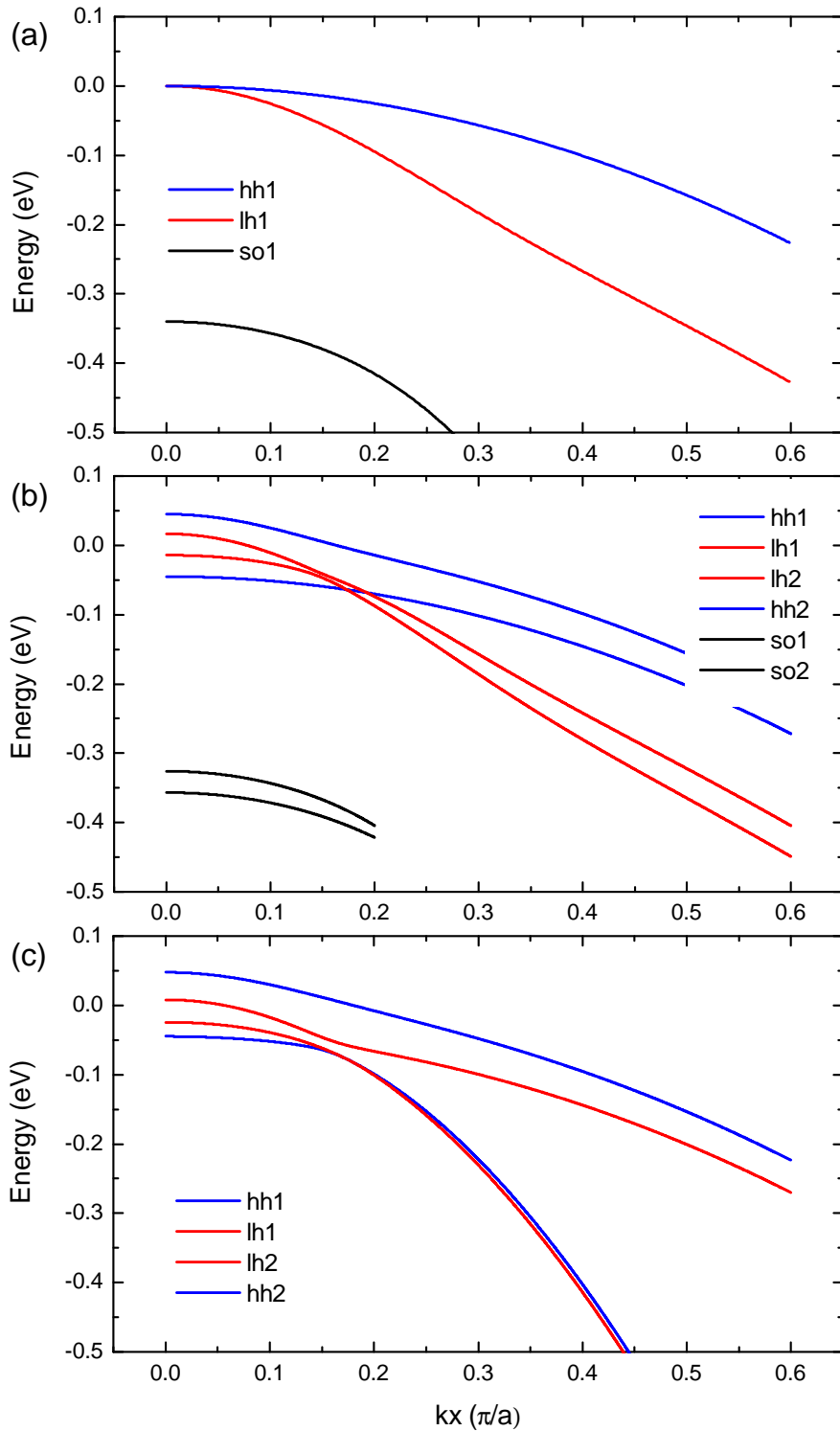
Figure 2.3: Calculated valence band structures with dispersion along k_x. (a) Band structure of GaAs obtained by diagonalizing H_{KL}. (b) Band structure of unstrained (Ga,Mn)As taking into account pd exchange interaction ($H_{KL} + H_{pd}$). The magnetization points in x-direction. (c) Biaxially compressively strained (Ga,Mn)As without split-off band ($H_{KL} + H_{pd} + H_e$). Assumed strain values: $e_{xx} = e_{yy} = -2.60 \cdot 10^{-3}$; $e_{zz} = 2.34 \cdot 10^{-3}$. The carrier density is assumed to be $4 \cdot 10^{20}$ cm^{-3}.

use a value of $B_g = 15$ meV, which gives rise to a total valence band splitting at Γ of 90 meV. The magnetization $\mathbf{M}$ is a classical vector in the mean field approximation :

$$\mathbf{M} = \begin{pmatrix} M_x \\ M_y \\ M_z \end{pmatrix} = M \begin{pmatrix} \sin\theta\cos\phi \\ \sin\theta\sin\phi \\ \cos\theta \end{pmatrix} \tag{2.7}$$

The angles θ and ϕ represent the direction of magnetization. For the 6 band model, H_{pd} reads

$$\mathrm{H}_{pd} = B_g \left(\begin{array}{cccc|cc} 3M_z & \sqrt{3}M_- & 0 & 0 & \sqrt{6}M_- & 0 \\ \sqrt{3}M_+ & M_z & 2M_- & 0 & -2\sqrt{2}M_z & \sqrt{2}M_- \\ 0 & 2M_+ & -M_z & \sqrt{3}M_- & -\sqrt{2}M_+ & -2\sqrt{2}M_z \\ 0 & 0 & \sqrt{3}M_+ & -3M_z & 0 & -\sqrt{6}M_+ \\ \hline \sqrt{6}M_+ & -2\sqrt{2}M_z & -\sqrt{2}M_- & 0 & -M_z & -M_- \\ 0 & \sqrt{2}M_+ & -2\sqrt{2}M_z & -\sqrt{6}M_- & -M_+ & M_z \end{array} \right) \tag{2.8}$$

where

$$M_+ = M_x + iM_y \qquad M_- = M_x - iM_y$$

and M_α is the component of the magnetization unit vector in α-direction.

The effect of the spin orbit coupling is that the states are split by the projection m_j of the total angular momentum $\mathbf{J}$ on the magnetization axis. For states 1 and 4 (the original hh states, now labeled in energetic order at Γ), the spin is completely aligned with the magnetization axis and receives the full strength of H_{pd}, which is $\pm 3B_g$. States 2 and 3 (original lh) show a mixing of spin states and consist of one third (two thirds) spin-down and two thirds (one third) spin-up, respectively. The energy of the four states, labeled in decreasing energetical order, is therefore:

$$\begin{aligned} E_1 &= 3B_g \tag{2.9} \\ E_2 &= \frac{1}{3}(-3B_g) + \frac{2}{3}(3B_g) = B_g \\ E_3 &= \frac{2}{3}(-3B_g) + \frac{1}{3}(3B_g) = -B_g \\ E_4 &= -3B_g \end{aligned}$$

Fig. 2.3 (b) shows the effect of the combined $\mathrm{H}_{KL} + \mathrm{H}_{pd}$ band structure. The original heavy holes are split by 90 meV at the Γ-point, while the splitting of the light hole bands is 30 meV, which leads to a crossing of the lh and hh bands around a k-value of $k_x = 0.18$. The spin-orbit split-off band is also split by 30 meV by the pd interaction. In the following calculations, we will neglect the split-off band and limit ourselves to a four band model. We can do this because the spin-orbit splitting (341 meV) is large enough to raise the split-off band above the Fermi energy of (Ga,Mn)As, which will leave it unoccupied by holes.

Lattice Strain

The final contribution to the band structure which we need to consider is the influence of lattice strain, which is an intrinsic property of (Ga,Mn)As due to the epitaxial

growth on a substrate with different lattice constant. We use the Hamiltonian H_e, as described in [Bir 74], to model the strain contribution to the bands. Its full form is given in Appendix A.2. This representation takes the shear strain into account, which is usually neglected for pseudomorphic layers, but plays a role in the $[1\bar{1}0]$ oriented stripes as will be shown in Chapter 4.

The valence band structure (without split-off band) of (Ga,Mn)As displayed in Fig. 2.3 (c) was calculated by diagonalizing the sum of all three Hamiltonians, $H_{KL} + H_{pd} + H_e$. For this band structure we assume a strain corresponding to a pseudomorphic layer with a Mn concentration of 5.4 %. The influence of biaxial strain in the (Ga,Mn)As layer is obvious when comparing this figure with Fig. 2.3 (b), which corresponds to unstrained (Ga,Mn)As. We note that the light hole band lh1 and the heavy hole band hh2 switch their character in the region of the anticrossing point around $k_x = 0.15$. Therefore, the labeling of the bands as hh and lh is no longer valid in this band structure, as the character of a band is not preserved over the whole Brillouin zone. Instead, we will use an energetic ordering, starting with the highest energy band at the zone center.

Another effect of strain is a small energetic shift of the bands, which changes the amount of splitting due to pd exchange interaction. In Fig. 2.3 (c), at Γ, this shift is

$$\Delta E_1 = 9.65 \text{ meV}, \quad \Delta E_2 = -8.29 \text{ meV}, \quad \Delta E_3 = -9.22 \text{ meV}, \quad \Delta E_4 = 7.91 \text{ meV}.$$

Both original hh bands are shifted to higher energies, while the original lh bands are shifted to lower energies.

2.3 Magnetic Anisotropy

The anisotropy of the crystal is linked to the magnetic properties of the semiconductor via spin-orbit coupling. Considering the T_d symmetry of the zinc blende host lattice, the theoretically predicted magnetocrystalline anisotropy of bulk (Ga,Mn)As is either cubic, with the three symmetrically equivalent $\langle 100 \rangle$ crystal directions as the preferred axes of magnetization (easy axes), or easy axes along the $\langle 111 \rangle$ directions. Experimentally, easy axes along the $\langle 111 \rangle$ directions have never been observed. However, given that (Ga,Mn)As is grown epitaxially, in practice, one never deals with the pure bulk properties. As mentioned earlier, the substrate on which the layer is grown has a significant influence on its crystal structure via growth strain and therefore has an impact on its anisotropy.

It is possible to obtain the magnetic anisotropy from the $\mathbf{k} \cdot \mathbf{p}$ band structure calculations discussed in the previous section. For this, one needs to calculate the band structure over the whole 3D k-space and populate the bands with holes (assuming a known carrier concentration) from the valence band edge up to the Fermi energy. Since the bands do not have rotational symmetry around the z-axis in k-space, some in-plane directions will have lower energy states than others. For compressively strained (Ga,Mn)As, these are the in-plane $\langle 100 \rangle$ directions, which will therefore be the preferred directions of magnetization. In the magnetic anisotropy picture, these directions represent the biaxial easy axes of magnetization.

The case of tensile strained (Ga,Mn)As, achieved by growth on relaxed (In,Ga)As buffers (with $\sim$8% In), leads to an out of plane easy axis and has been investigated

in detail by [Liu 05] and [Xian 05]. Instead of explicitly calculating the magnetic anisotropy from the band structure, we will pursue a phenomenological description in the following.

Compressively strained (Ga,Mn)As has a lowered symmetry D_{2d}. For this case, an easy axis out of the plane has also been observed for low doped layers at very low temperatures [Sawi 04], with the easy axis shifting into the plane for temperatures closer to T_C. However, for high hole concentration samples used in this work, the layers usually show a strong out of the plane hard axis [Sawi 04]. For these samples, the easy axis is found in the plane of the sample, but exhibits a complex, temperature dependent anisotropy behavior resulting from the interplay of three anisotropy components [Goul 04, Papp 07]:

- The strongest biaxial component yields easy axes along [100] and [010].

- A uniaxial anisotropy term with easy axes along [110] or [$\bar{1}$10].

- A much smaller uniaxial contribution with easy axes along [010] or [100].

It has been theoretically predicted by [Call 66] that the biaxial anisotropy scales with the magnetization as M^4 while the uniaxial goes as M^2. As a result, the dominant anisotropy term changes from biaxial to uniaxial as the temperature approaches T_C and M decreases [Wang 05]. As shown by K. Pappert et. al. [Papp 07b], by summing up the anisotropy terms of different symmetry, the magnetostatic energy E of a magnetic domain with magnetization orientation ϑ with respect to the [100] crystal direction in the layer plane can be expressed as:

$$E = \frac{K_{cryst}}{4} \sin^2(2\vartheta) + K_{uni[\bar{1}10]} \sin^2(\vartheta - 135°) + K_{uni[010]} \sin^2(\vartheta - 90°) - MH \cos(\vartheta - \varphi).$$
(2.10)

The first term describes the biaxial crystalline anisotropy contribution, the second and third term the uniaxial contributions, and the last term is the Zeeman energy, where φ is the angle between an external magnetic field and the magnetization direction. The origin of both uniaxial terms is not yet fully understood. While the growth strain breaks the symmetry between in plane and out of plane, no clear mechanism for the symmetry breaking of the in plane $\langle 110 \rangle$ and $\langle 100 \rangle$ directions has been found to date. It is suspected, that surface reconstruction effects on the GaAs buffer surface [Welp 03, Welp 04] or finite thickness of the layer and a difference in the substrate/layer and layer/air interface play a role in the appearance of the $\langle 110 \rangle$ anisotropy contribution.

Plotting the total magnetostatic energy (see Fig. 2.4) reveals the energy landscape in the absence of external fields. For the values of the anisotropy constants, the typical ratio of $K_{cryst} : K_{uni[\bar{1}10]} : K_{uni[010]} = 100 : 10 : 1$ has been used [Goul 08]. The valleys of the energy curve mark the position of the easy axes. $K_{uni[\bar{1}10]}$ affects the difference in height of the energy maxima, while $K_{uni[010]}$ influences the minima of the curve.

From the above, it is obvious that strain plays a critical role in determining the anisotropy behavior of (Ga,Mn)As. To investigate how strain, and strain relaxation in particular, affects the anisotropy in (Ga,Mn)As nanostructures is the main focus of this work and will be discussed extensively in later chapters.
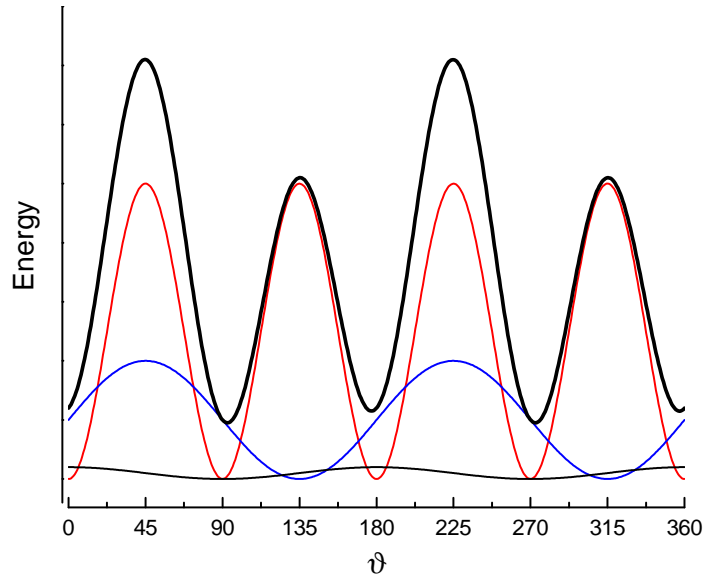
Figure 2.4: Magnetostatic energy landscape at zero field (thick black line) of epitaxial (Ga,Mn)As. The three anisotropy components are plotted as thin lines (red - biaxial; blue - uniaxial along $[\bar{1}10]$; black - uniaxial along $[010]$).

An important quantity in this context is the magnetic field needed to force the magnetization parallel to an external field in the hard axis direction, which is called the anisotropy field H_a. It is a measure of the anisotropy strength and can be calculated from Eqn. (2.10) using the definition of the anisotropy field: H_a is the strength of a field along the hard axis (here 45°) needed to suppress the local minima along the easy axes.

$$H_a = \frac{2K_{cryst}}{M} \tag{2.11}$$

2.3.1 Transport Measurements and AMR

The method of choice to determine the anisotropy constants in Eqn. (2.10) are magnetotransport measurements. To investigate transport properties, we use Hall-bar-like structures, where the longitudinal and transverse four probe resistance can be recorded as a function of an applied magnetic field. Thorough analysis of the obtained data is achieved by the recently developed 'anisotropy fingerprint' technique [Papp 07], which consists of taking magnetotransport measurements for magnetic fields swept in multiple directions.

Ferromagnets in general exhibit anisotropic transport properties. In the following, we will discuss the special case of the ferromagnetic semiconductor (Ga,Mn)As. This material system shows a strong anisotropic magnetoresistance (AMR) effect in the sense, that the resistivity for a current flow perpendicular to the magnetization of the material is larger than parallel to the magnetization [Baxt 02]. The resistivity ρ is thus no longer a number, but rather a tensor, and Ohm's law relating the electric field $\mathbf{E}$ to the current $\mathbf{J}$ can be expressed with the electric field broken up in components parallel and perpendicular to the magnetization $\mathbf{M}$ [Jan 57, McGu 75]:

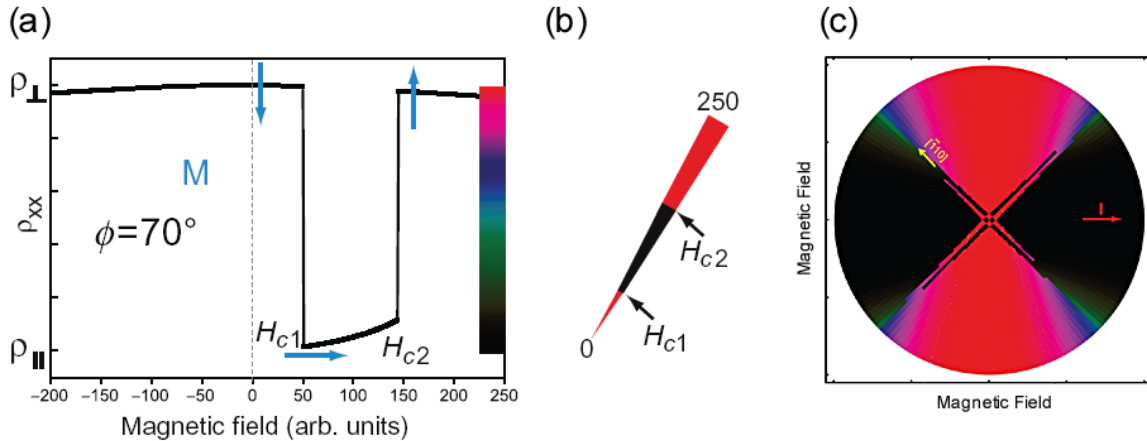$$\mathbf{E} = \rho_{\parallel}\mathbf{J}_{\parallel} + \rho_{\perp}\mathbf{J}_{\perp} \tag{2.12}$$

Figure 2.5: (a) Simulation of a magnetoresistance scan along $\phi = 70°$. The magnetization (blue arrows) undergoes two switching events H_{c1} and H_{c2}, corresponding to two subsequent 90° domain wall propagation events. (b) Conversion of the magnetoresistance scan into a sector of a polar plot. (c) Simulation of a full 360° resistance polar plot composed of multiple single scans. The red arrow indicates the direction of current flow.

A projection onto the current path gives the longitudinal resistivity ρ_{xx}

$$\rho_{xx} = \rho_\perp - (\rho_\perp - \rho_\parallel) \cos^2(\vartheta), \tag{2.13}$$

where ϑ is the angle between **M** and **J**. If the magnetization in a Hall bar sample is rotated in the sample plane by a strong external magnetic field, a sinusoidal behavior of the longitudinal resistance R_{xx} with respect to the field angle is thus expected.

2.3.2 Anisotropy Fingerprints

In the process of compiling an anisotropy fingerprint, a number of four terminal longitudinal resistance measurements are performed (for details on the Hall bar geometry, see [Goul 08]). For each scan, the magnetic field is swept from -300 to $+300$ mT along a given direction with an angle ϕ to the current direction. This procedure is then repeated for multiple angles. Fig. 2.5 (a) shows a simulation of such a scan for the case of $\phi = 70°$. At high negative fields, the magnetization is forced along the field direction. As the field decreases, **M** relaxes through Stoner-Wohlfarth rotation until it is aligned with the closest easy axis, which is perpendicular to the current direction in this case. At positive fields, we observe two switching events, labeled H_{c1} and H_{c2}, which are associated with the two sequential 90° domain wall nucleation/propagation events which account for the magnetization reversal in this material [Welp 03]. In order to analyze the data, the positive half field of each measurement is converted to a sector of a polar plot as shown in Fig. 2.5 (b). The two switching events, indicated in the figure, show up as abrupt color changes. A compilation of all sectors representing a full 360° revolution produces an anisotropy fingerprint resistance polar plot such as the one simulated in Fig. 2.5 (c).

From this polar plot, it is possible to identify all three anisotropy constants in Eqn. (2.10). If we consider the case of a purely biaxial anisotropy without uniaxial contributions, the inner region of the polar plot in Fig. 2.5 (c) would take the form of
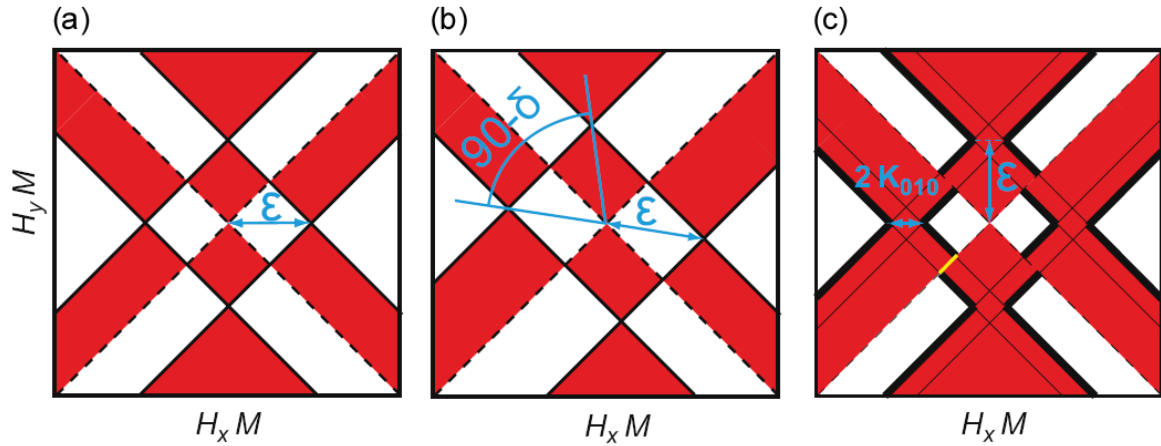
Figure 2.6: Sketches of the shape of the inner region of an anisotropy fingerprint for (a) a sample with only the biaxial crystalline anisotropy resulting in easy axes along [100] and [010], (b) a sample with biaxial plus a $[\bar{1}10]$ uniaxial easy axis and (c) a sample with a biaxial plus a [010] uniaxial easy axis.

a perfect square such as the one simulated in Fig. 2.6. The corners of the square are along the easy axes and the length of the half diagonal is given by ε, the domain wall nucleation energy. The inclusion of a uniaxial anisotropy bisecting two of the biaxial easy axes tilts the resulting easy axis towards the direction of the uniaxial anisotropy by an angle δ [Goen 05] and elongates the square into a rectangle as simulated in Fig. 2.6 (b). The strength of the uniaxial anisotropy constant in the $[\bar{1}10]$ direction $K_{uni[\bar{1}10]}$ relative to the biaxial anisotropy constant K_{cryst} can be extracted from the angle δ by the relationship given by [Papp 07c]:

$$\delta = \arcsin\left(\frac{K_{uni[\bar{1}10]}}{K_{cryst}}\right). \tag{2.14}$$

In practice it is often more convenient to work with the aspect ratio of the width W to the length L of the rectangle, instead of the angle δ, which is related to the anisotropy terms as:

$$\frac{K_{uni[\bar{1}10]}}{K_{cryst}} = \cos\left(2\arctan\left(\frac{W}{L}\right)\right). \tag{2.15}$$

If a uniaxial anisotropy is instead added parallel to one of the uniaxial easy axes, an asymmetry arises in the energy required to switch between the two biaxial easy axes. As shown in Fig. 2.6 (c), the inner pattern is then comprised of parts of an inner and an outer square. The difference in the length of their half diagonal is a measure of the [010] anisotropy constant $K_{uni[010]}$. Due to mixing of the anisotropy terms, a deformation of the fingerprint near the corners of the rectangle is commonly observed. Therefore it is often easier to identify the presence of a [010] uniaxial easy axis by determining the spacing between the sides of the square (or rectangle in the case that a $[\bar{1}10]$ uniaxial term is also present), as indicated by the yellow line in Fig. 2.6 (c). The length of this line is equal to $\sqrt{2}K_{uni[010]}$.

A limitation of the fingerprint technique is, that it cannot be used to reliably extract exact values for K_{cryst}. The value K_{cryst}/M can be estimated to good accuracy from

the shape of the curve as the magnetization rotates away from the easy axis towards the external magnetic field at higher fields. A typical value for this parameter for all examined samples is approximately 100 mT.

2.4   Post Growth Annealing

An important development in the post growth treatment of (Ga,Mn)As was fueled by the discovery that T_C could be significantly increased by thermal annealing of a sample after fabrication [Haya 01, Pota 01]. As indicated earlier, the main goal when aiming to increase T_C, is to increase the carrier concentration by reducing the amount of compensating interstitial Mn impurities. By heating the sample for long times (> 100 h) at temperatures slightly below growth temperature ($T = 190$ °C), one allows the interstitial Mn atoms to diffuse to the surface of the material, where they are passivated.

The activation energy of interstitial Mn of 0.7 eV [Edmo 04] is small enough to allow for segregation even at small thermal energies of $k_B T \approx 40$ meV at $T = 190$ °C at sufficiently long times. During this process, the substitutional Mn remains unaffected. Mn atoms that reach the surface of an uncapped layer by migrating in a random walk, react with atmospheric oxygen and form MnO. Therefore, they no longer act as unwanted donors which compensate hole carriers. It has been shown that annealing increases the thickness of the surface oxide layer and can lead to a fourfold increase in Mn concentration in the surface region of a (Ga,Mn)As layer [Schm 08].

However, caution must be exercised, as this procedure can have undesired side effects. Since the transition temperature at which easy axis reorientation takes place is carrier dependent [Sawi 04], thermal annealing can trigger changes in the magnetic anisotropy as it increases the hole carrier concentration. For this reason, none of (Ga,Mn)As layers of samples presented in this work have been subjected to annealing, and care has been taken to ensure minimal heat load on the samples during processing.

Chapter 3

MBE Growth of Ferromagnetic (Ga,Mn)As Layers

3.1 The UHV MBE Chamber

All samples presented in this work were grown in an ultra high vacuum (UHV) molecular beam epitaxy (MBE) chamber dedicated to the growth of GaAs-based III–V semiconductors. The geometry of the chamber and the arrangement of its components (see Fig. 3.1 for a schematic) was designed in the department and has been custombuilt to fit the requirements of the clean room laboratory. A special feature of this chamber is its compact design with ca. 1/3 of the pumping volume of a standard RIBER MBE–32 chamber.

The chamber is equipped with effusion cells in which high purity material is heated in PBN (pyrolytic boron nitride) crucibles to achieve a homogeneous flux of atomic or molecular particles directed towards the sample. The flux, which is measured prior to growth with a Bayard-Alpert pressure gauge mounted on the manipulator, is switched on or off during growth by mechanic shutters blocking the cell opening. An additional main shutter shields the sample from the material flow from all cells. The manipulator can be rotated to face the transfer tube through which sample holders are inserted into the chamber, to align the sample holder with the cells, or to bring the pressure gauge into flux measurement position. An in-depth description of the MBE chamber and its components can be found in [Scho 04].

3.2 Epitaxial Growth of (Ga,Mn)As

A number of factors play a critical role in the epitaxial growth of (Ga,Mn)As. In this section, we will examine the influence of several crucial growth conditions in detail and finish with a brief sketch of a typical (Ga,Mn)As growth procedure.

3.2.1 The Mn Cell Temperature

The most obvious influence on the incorporation of Mn into the GaAs lattice is the temperature T_{Mn} of the Mn effusion cell. The vapor pressure p of a material, based
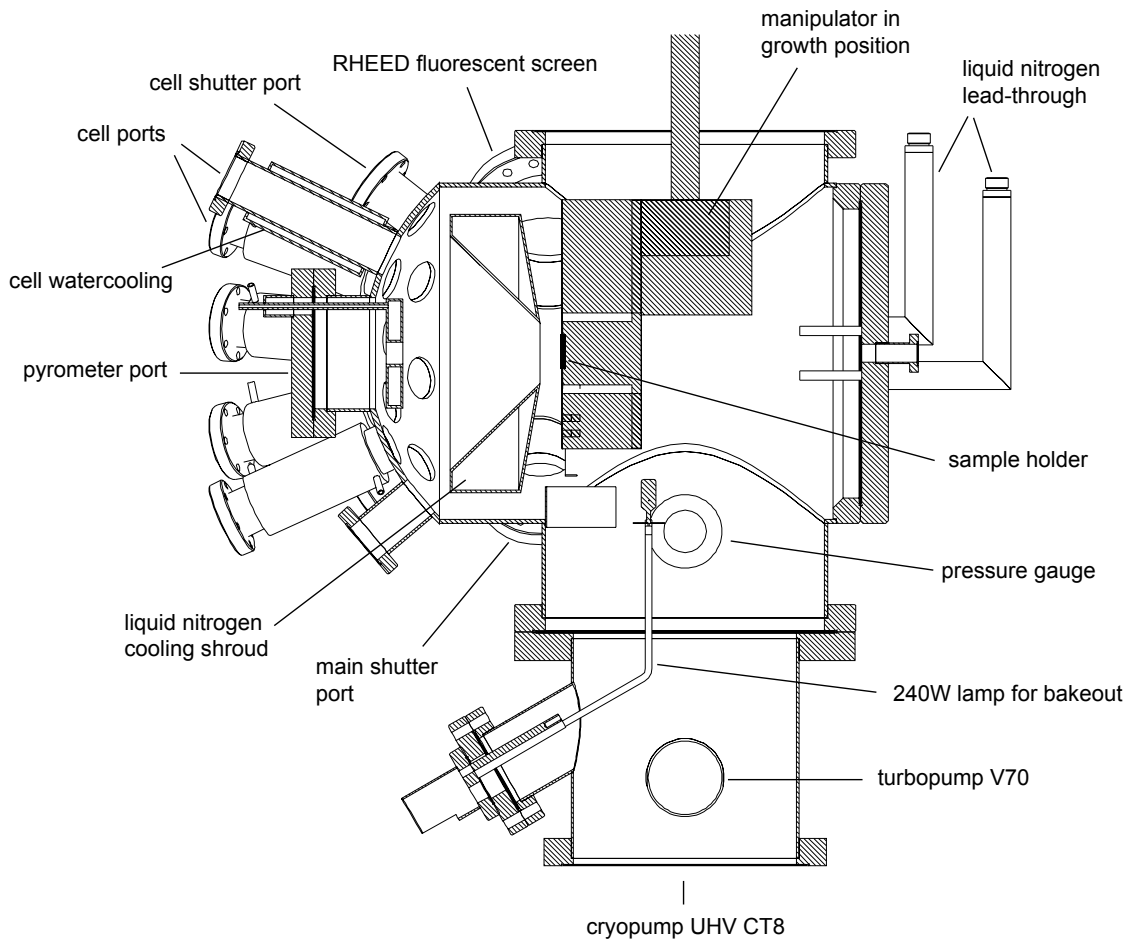
Figure 3.1: Schematic cross section of the UHV MBE chamber. The cells are mounted on the left side, aligned towards the sample holder sitting on the manipulator (shaded area) occupying the central cavity.

on thermal activation at a temperature T, is given by

$$p = b \, e^{-E/kT}. \tag{3.1}$$

E is the activation energy, k the Boltzmann factor and b a temperature dependent material parameter. For the small range of temperatures employed during growth in an effusion cell, the dependence is approximately exponential. Therefore, assuming favorable growth conditions, the amount of incorporated Mn (determined by HRXRD, see Section 3.5.1) also increases exponentially with rising cell temperature, as shown in Fig. 3.2 for a number of layers grown over a range of suitable Mn cell temperatures. As indicated by the trendline, an increase of T_{Mn} by 20°C leads to a doubling of the Mn content.

3.2.2   The Growth Temperature

The solubility of Mn in GaAs at thermal equilibrium is very low. (Ga,Mn)As is a metastable compound which can only be grown under conditions far from the equilib-
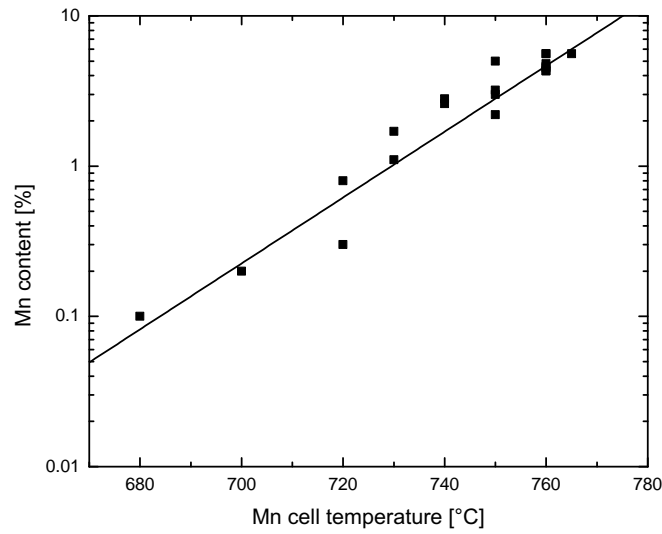
Figure 3.2: Mn content in % for (Ga,Mn)As layers grown over a large range of Mn cell temperatures. The trendline illustrates the approximately exponential correlation. The growth rate is typically 1 Å/s.
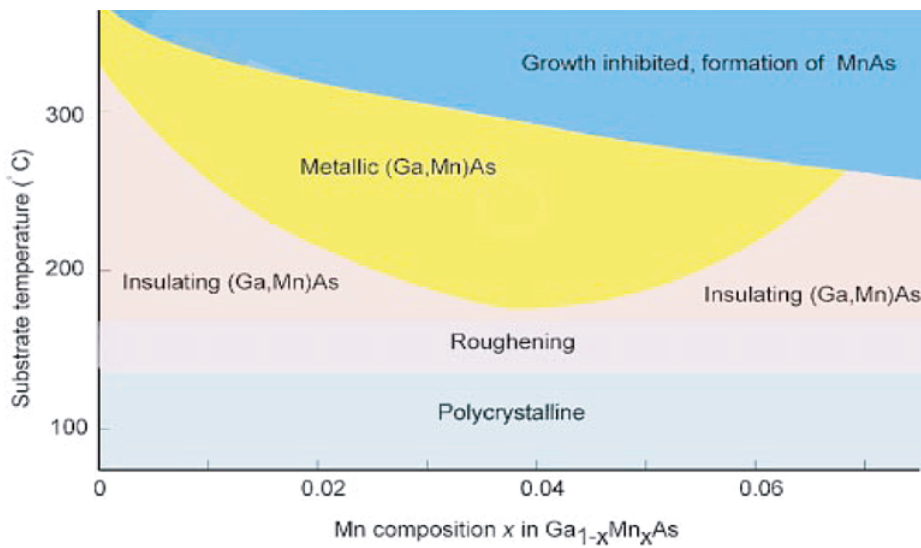

Figure 3.3: Schematic phase diagram illustrating the connection between the growth parameters substrate temperature and Mn content and the properties of the grown Ga,Mn)As layer [Ohno 98].

rium regime. Due to the low temperatures necessary to fabricate this material (below 300 °C), the growth is often referred to as low-temperature (LT) MBE growth. For this reason, the growth (or substrate) temperature T_{sub} plays a critical role in the epitaxial fabrication of (Ga,Mn)As layers for a given Mn content. First studies of the influence of this parameter have been carried out by H. Ohno [Ohno 98]. Fig. 3.3 is taken from this publication and shows a schematic phase diagram of epitaxially grown (Ga,Mn)As.

Below a certain substrate temperature, no growth of monocrystalline material takes

place. The onset of monocrystalline growth is characterized by a rough surface which
smoothes out at around 180 °C. Above this temperature, two phases of insulating
and metallic (Ga,Mn)As coexist, depending on the Mn content of the layer. As the
temperature approaches 300 °C, the formation of MnAs clusters becomes prevalent.

Care has to be taken when applying the temperature values of Fig. 3.3 to the
growth procedure of a layer, as the uncertainty in temperature measurement and
the influence of other growth parameters such as growth speed or As/Ga ratio also
significantly influence the properties of the material.

Another important consideration is that T_{sub} not only affects the solubility of Mn
in GaAs but also the quality of the LT growth in general. A lower growth tempera-
ture results in an increase in point defect density compared to a layer grown at high
temperature [Liu 95, Scho 03]. The main influence on the crystal lattice of LT-GaAs
originates from As antisites, Ga vacancies, and to a lesser degree, As interstitials. It
is therefore crucial to strike a balance between Mn incorporation, which increases for
lower temperatures, and retaining high crystal quality, which deteriorates for lower
T_{sub}. In our experience, for samples in the 1–5 % Mn content range, $T_{sub} = 270$ °C is
a favorable growth temperature.

3.2.3   V/III Flux Ratio

The ratio of the beam equivalent pressures (BEP) of the main group V (As) and III
(Ga) material fluxes is another critical MBE parameter. Epitaxial high temperature
growth (HT) of GaAs takes place under As overpressure (high As/Ga ratio) to as-
sure smooth surface formation. The evaporation process in the As cell supplies As_4
molecules. Depending on the type of effusion cell, these molecules are either directly
fed to the sample, or, in the case of a cracker cell, broken down to As_2 in a sepa-
rately heated region before coming in contact with the sample. Studies have shown,
that the use of a cracker cell can improve the structural qualities of a (Ga,Mn)As
layer [Camp 03]. This effect is attributed to a lower concentration of As antisite
(As_{Ga}) defects due to different incorporation kinetics of As_4 and As_2.

For our samples, we use uncracked As_4 molecules. For the HT GaAs growth, the
ratio of As/Ga = 40. For the LT (Ga,Mn)As growth this value is lowered to As/Ga
= 25 for most layers. At low temperatures, a high As/Ga ratio leads to an increased
concentration of As antisite defects which degrades the structural quality and increases
the lattice constant. This can lead to errors in the determination of the Mn content,
which is identified by the lattice constant of the (Ga,Mn)As layer (see Section 3.5.1).
As_{Ga} also acts as a double donor that compensates Mn acceptors, therefore lowering
the overall carrier concentration [Myer 06]. Ideally, the lattice constant of the LT
GaAs should not differ measurably from its HT counterpart. In samples where very
high Mn concentrations are intended, a lower As/Ga ratio is necessary to avoid MnAs
cluster formation.

3.2.4   Growth Rate

The amount of supplied material determines the rate at which new crystal layers are
formed. In the case of GaAs growth, the amount of Ga is the determining factor,
since the growth takes place under As overpressure. While very fast growth rates can

lead to a decrease in crystal quality, it is important to consider that a low growth rate for (Ga,Mn)As leads to self annealing during growth, which can significantly alter the magnetic anisotropy of the layer. The effect of annealing on (Ga,Mn)As is discussed in detail in Section 2.4.

3.2.5   Typical Growth Procedure

The substrate, a 2" epi-ready GaAs(001) wafer (or pieces thereof), is glued to a Molybdenum sample holder with liquid Indium to ensure best possible thermal contact. Dust is removed from the surface with a Nitrogen jet. After insertion into the UHV system, the sample holder is placed in a heating station and brought up to 300 °C for 15 min to remove residual water. The sample is then transferred into the growth chamber and slowly heated to a substrate temperature of 610 °C, which is sustained for 5 min, to remove the surface oxide layer. In RHEED (see Section 3.4, this transition is visible as the disappearance of the diffuse background, which is replaced by a reflection corresponding to the GaAs surface reconstruction. During this step, the sample is kept under a constant As pressure, starting at $T_{sub} = 400$ °C.

   After the oxide desorption, the temperature is lowered to 580 °C. At this temperature, a high quality 200 nm GaAs buffer layer is grown on the substrate to achieve a smooth surface and bury possible surface contaminations and defects on the wafer. In the following growth interruption, the substrate temperature is lowered to the (Ga,Mn)As growth temperature. The As flux is turned off at $T_{sub} = 570$ °C to preserve the GaAs (2×4) reconstruction.

   The majority of the (Ga,Mn)As layers in this work are grown at a substrate temperature of 270 °C. Upon reaching this value, the temperature is stable after approx. 15 min. Prior to the growth of (Ga,Mn)As, a thin (1 nm) layer of GaAs is deposited for an optimal growth start. With completion of the (Ga,Mn)As growth, all fluxes are shut off simultaneously. The sample is finally removed from the chamber after T_{sub} falls below 200 °C.

3.3   Crystal Defects

Besides the aforementioned atomic point defects (As_{Ga}, Mn_{I}, etc.), a common phenomenon in epitaxial growth is the occurrence of large-scale crystal defects. A convenient way to investigate crystal defects that are visible on the surface of the sample is Nomarski interference microscopy, which can achieve very high (few nm) vertical resolution. The most prominent defect structure is the "cross-hatch" pattern shown in Fig. 3.4 (a), which is usually observed on all MBE-grown samples. This defect type is visible as a dense net of intersecting ridge-like step edges aligned along the [110] and [1$\bar{1}$0] crystal directions, covering the entire sample surface. The origin of this defect type is threading dislocations caused by small precipitates in the substrate which intersect the substrate surface along $\langle 110 \rangle$ lines [Cunn 86]. Due to the low height and large spacing of the steps, we do not consider this type of defect to be detrimental to processing or measurement of layers and structures.

   Another large scale growth disruption is caused by Gallium spitting from the Ga effusion cell or its shutter, which leads to circular areas where normal crystal growth is replaced by a rough, grainy surface, often with a distinct central region. As can
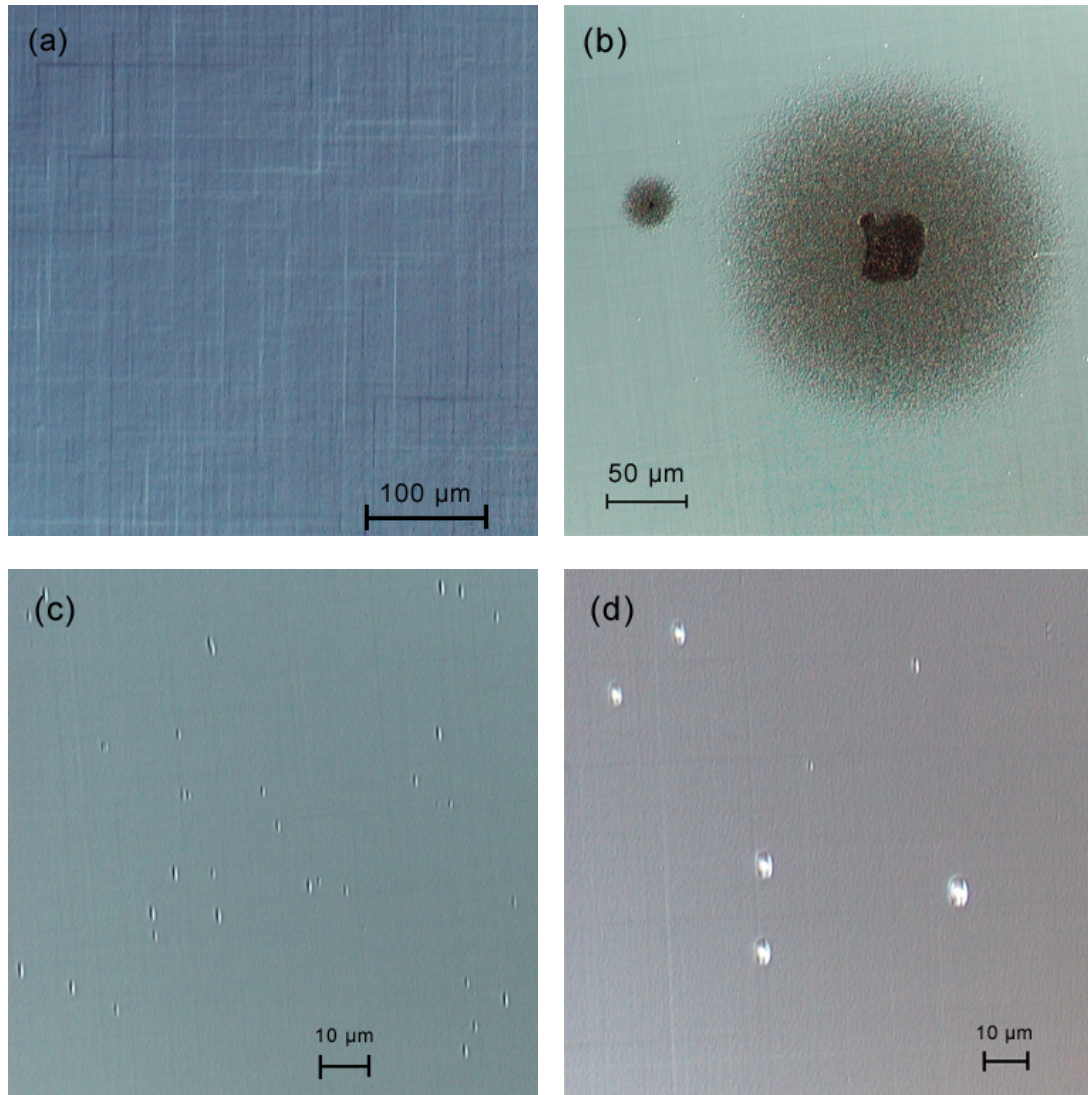
Figure 3.4: Nomarski interference microscope images of common crystal defects visible on a (Ga,Mn)As surface. (a) cross-hatches, (b) disrupted crystal growth due to Ga spitting, and two kinds of oval defects. Type α (c) contains no macroscopic core particulate, in contrast to type β (d).

be seen in Fig. 3.4 (b), these areas can extend over several hundreds of micrometers. Especially large areas are visible by the naked eye as milky, circular spots. While this defect has no influence beyond the affected area, care has to be taken to avoid such sample pieces for processing or measurement.

A class of much smaller defects are the oval defects, named for their appearance as oval surface pits, with their long axis aligned along either [110] or [1$\bar{1}$0]. As first classified by K. Fujiwara et. al. [Fuji 87], there are two major types of oval defects. The α type lacks a macroscopic core particulate, while the β type contains a visible core particulate. Fig. 3.4 (c) and (d) show α and β type oval defects observed on our (Ga,Mn)As samples. The size of both types increases with total grown layer thickness, which leads to the conclusion that the origin of this defect lies at the substrate/layer interface, most likely in the form of carbon contaminations. The density of oval defects
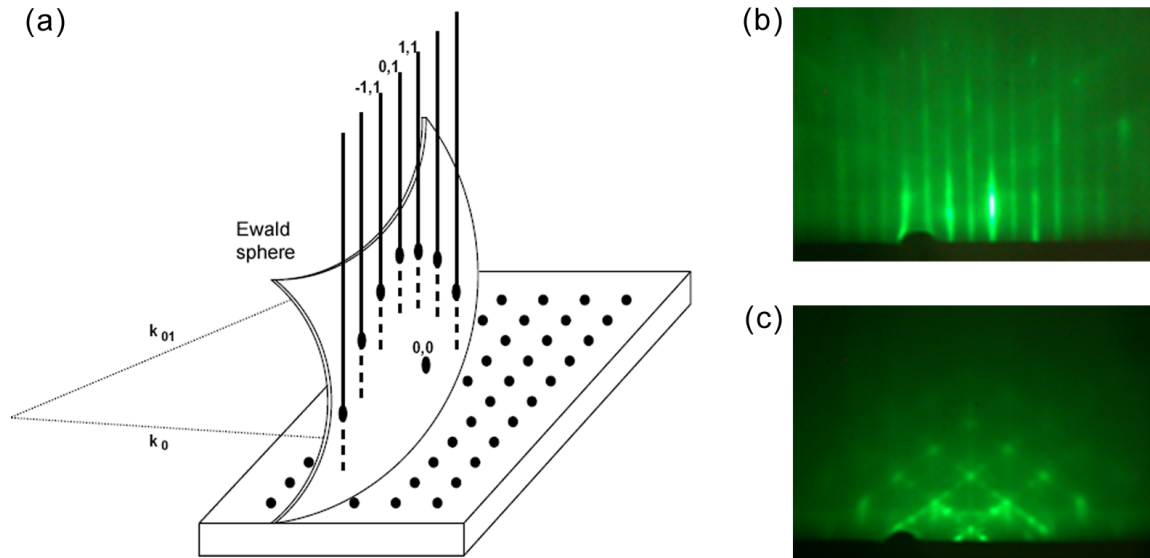
Figure 3.5: (a) Ewald sphere construction for the diffraction of fast electrons in k-space. The reciprocal lattice of the crystal surface are vertical rods which intersect the Ewald sphere where the diffraction conditions are fulfilled. The other pictures show the RHEED pattern for (b) a high quality GaAs layer and (c) the hexagonal lattice of MnAs clusters in a (Ga,Mn)As layer.

can vary greatly over different areas of the wafer. Type α defects are often found in larger concentrations in the central region of the wafer, while β defects are either randomly scattered over the whole wafer or found in dense clusters covering up to a few hundred micrometers. At low densities, both types of defects are not detrimental to the properties of the layer, as the affected volume is very small. Possible complications may arise during nanopatterning, where any kind of crystal deformation needs to be avoided.

3.4 RHEED

An important in-situ characterization method is reflection high energy electron diffraction (RHEED). An electron beam with an energy between 10–30 keV is directed on the sample surface under a glancing incidence angle (1–3°). The electrons penetrate only the first monolayers where they are diffracted (scattered) by the surface atoms. According to the crystal structure, the spacing of the atoms at the sample surface and the de Broglie wavelength of the incident electrons, the diffracted electrons interfere constructively at specific angles. The diffraction pattern is observed at a Phosphor fluorescence screen mounted on the chamber side opposite to the electron gun.

Fig. 3.5 (a) shows the Ewald sphere construction in the reciprocal space for determination of the constructive interference condition. Since the electron beam interacts only with the first few layers of the material, the reflection is massively broadened perpendicular to the sample surface such that it appears as a vertical line. The reciprocal lattice of a crystal surface is therefore a series of infinite rods extending perpendicular to the sample surface. Diffraction conditions are met, when the rods of the reciprocal
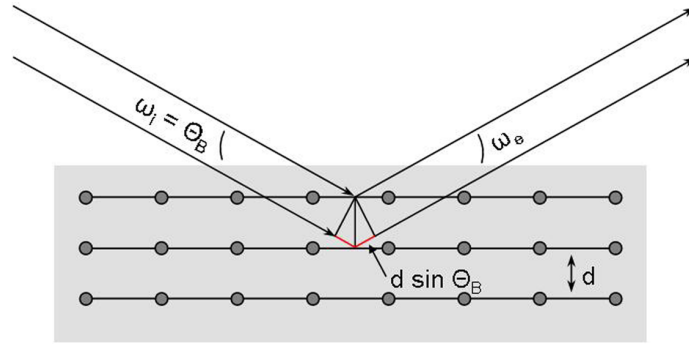
Figure 3.6: Diffraction geometry and Bragg condition for a symmetric reflection on parallel lattice planes. The path difference $2d \sin \Theta_B$ is marked in red.

lattice intersect the Ewald sphere. Due to the very short wavelength of the high-energy electrons, the radius of the Ewald sphere is much larger than the spacing between reciprocal lattice rods, which therefore intersect the sphere as an approximate plane. Additionally, both the rods and the Ewald sphere are broadened, the former due to defects and thermal vibrations, the latter due to the energy distribution of the electrons and divergence of the beam. This leads to the typical array of lines perpendicular to the sample surface, extending to both sides of the specular (0th order) spot.

In the context of MBE growth, RHEED serves two major functions. Firstly, it is a method to qualitatively evaluate the crystal growth in-situ without interfering with the process. High quality, two-dimensional growth is indicated by a "streaky" diffraction pattern with pronounced lines, as shown in Fig. 3.5 (b) for a GaAs layer. Roughening of the growth surface leads to breaking of the lines into a "spotty" diffraction pattern. During the growth of (Ga,Mn)As, the formation of MnAs clusters is visible as the appearance of a hexagonal pattern overlaying the usual vertical lines, see Fig. 3.5 (c). It is sometimes also desirable to determine the surface reconstructions [Bieg 90] of the material as they can influence the interface properties between layers. The HT GaAs buffer displays a (2×4) reconstruction which changes to (1×2) during (Ga,Mn)As growth.

Secondly, RHEED offers an in-situ way to determine the growth rate of the material [Shen 97]. A completely formed monolayer causes maximal reflection of the incident electrons, while the formation of the following monolayer is characterized by a drop in intensity due to roughening during its nucleation. Measuring the intensity of the specular spot over time shows an oscillating curve where adjacent maxima mark the completion of a monolayer, yielding a growth rate in ML/s.

3.5   X-Ray Diffraction

Among the most important ex-situ characterization methods for our work is high resolution x-ray diffraction (HRXRD) which yields detailed information about layer thickness, material composition, strain situation, and crystal quality. Standard characterization was performed using a Philips X'Pert system with a 4-crystal Ge(220) Bartels monochromator and a 2-crystal analyzer.

The diffraction geometry is sketched in Fig. 3.6. The parallel x-rays enter the
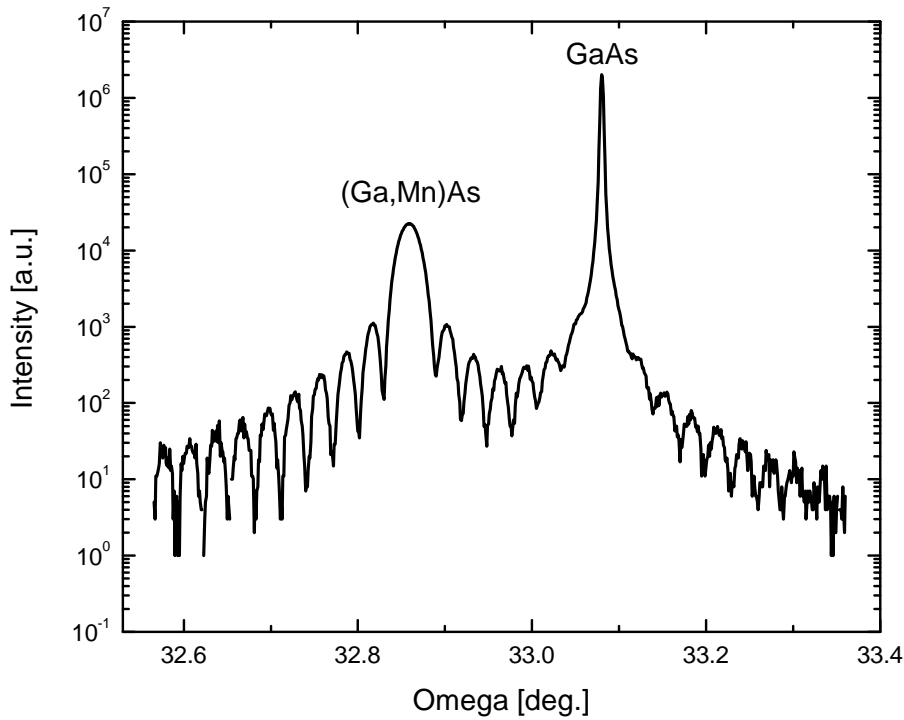
Figure 3.7: ω-2Θ scan of the (004) reflection of a 175 nm (Ga,Mn)As (6.3% Mn) layer on GaAs.

sample with an incidence angle ω_i relative to the lattice plains of spacing d in the sample. According to the law of reflection, the exit angle ω_e is equal to ω_i. The total angle between the incident beam and the detector is twice the incidence angle, and is commonly referred to as 2Θ. If the incidence angle equals the Bragg angle Θ_B, the path difference for parallel x-rays diffracted in the sample is an integer multiple n of the wavelength λ (1.5405929 Å for Cu K$_\alpha$). For this case, constructive interference between x-rays diffracted at different lattice planes is observed. This condition for constructive interference is called the Bragg condition:

$$2d\sin\Theta_B = n\lambda. \tag{3.2}$$

3.5.1 ω-2Θ Scans

In a sample with multiple layers, an ω-2Θ scan (varying both the incident, as well as the detector angle) over a range encompassing the Bragg angle for every layer, yields a high intensity peak according to each lattice constant. Fig. 3.7 shows an ω-2Θ scan of the (004) reflection of a (Ga,Mn)As layer on GaAs.

The (004) lattice planes are aligned parallel to the sample surface. The spacing of the lattice planes d_{004} is equal to 1/4 of the lattice constant, according to:

$$d_{hkl} = \frac{d_{001}}{\sqrt{h^2 + k^2 + l^2}} \tag{3.3}$$

A reflection is called symmetric, when the diffracting lattice plains are parallel to the sample surface. Symmetric reflections contain only information about the vertical
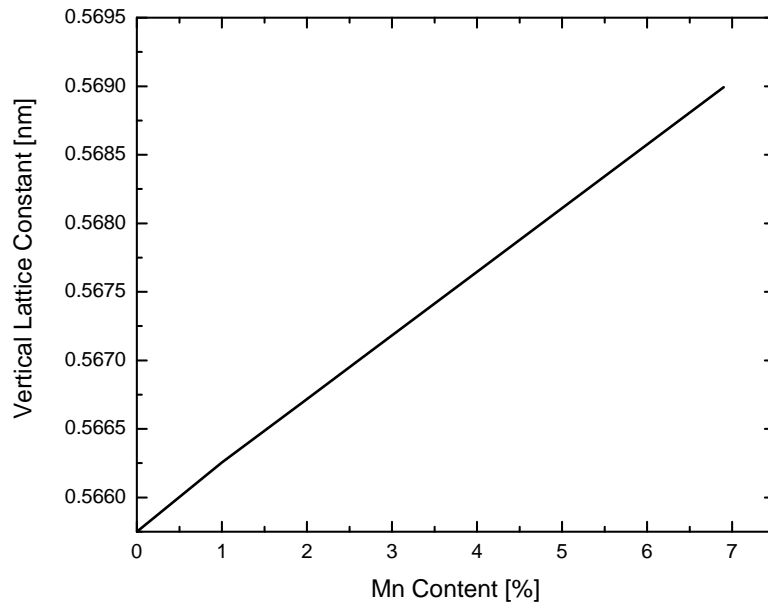
Figure 3.8: Calibration curve relating the vertical lattice constant $a_\perp$ of a (Ga,Mn)As layer with its Mn content.

lattice constant of the sample, which is easily visibly from the fact that only the l reciprocal direction enters the calculation. The remaining two, h and k, are zero. Reflections on lattice planes under an angle to the sample surface are called asymmetric reflections and contain information about two or all three spatial directions, depending on the specific reflection.

From an ω-2Θ scan as shown in Fig. 3.7, we obtain the Θ_B angle of the GaAs substrate as well as (Ga,Mn)As layer. Using the Bragg condition (Eqn. (3.2)), we define the angular difference $\Delta\Theta$ as

$$\Delta\Theta = \Theta_{GaAs} - \Theta_{(Ga,Mn)As} = \arcsin\left[\frac{\lambda}{2d_{GaAs,(004)}}\right] - \arcsin\left[\frac{\lambda}{2d_{(Ga,Mn)As,(004)}}\right]. \quad (3.4)$$

Solving this equation for the spacing of the (Ga,Mn)As lattice planes yields

$$d_{(Ga,Mn)As,(004)} = \frac{\lambda}{2\sin\left[\arcsin\left(\frac{\lambda}{2d_{GaAs,(004)}}\right)\right]}. \quad (3.5)$$

The lattice constant is finally given by Eqn. (3.3):

$$d_{(Ga,Mn)As} = 4 \cdot d_{(Ga,Mn)As,(004)}. \quad (3.6)$$

For an unstrained layer, this value is the bulk lattice constant. However, for a strained layer, it represents only the vertical lattice constant. The relaxed lattice constant has to be calculated from the elastic properties of the material, using Eqn. (4.17), which is derived in the following chapter.

The large number of additional small peaks in Fig. 3.7 are thickness oscillation peaks, also called fringe peaks. The period of these peaks is determined by the thickness of the (Ga,Mn)As layer. Their origin lies in multiple refraction of the x-ray beam

between the top and bottom interface of the layer. Each peak represents one order n in the Bragg condition (3.2), in which case d is the layer thickness. Analysis of these peaks is a way of accurately determining the thickness of an epitaxial layer and also indirectly the growth rate, when the growth time of the layer is known. The appearance of fringe peaks is also an indication of high interface and layer quality.

With regards to (Ga,Mn)As, one of the most important applications of HRXRD is the determination of the Manganese content in a layer. As Schott et. al. have shown, the lattice constant of (Ga,Mn)As is linearly dependent on the Mn concentration [Scho 01]. For our analysis, we use a calibration curve (shown in Fig. 3.8) based on this publication. From this curve, we derive an empirical formula with which we can determine the Mn content (in %) of a (Ga,Mn)As layer from the measurement of its vertical lattice constant $a_{\perp}$ (in nm):

$$[\text{Mn}] = \frac{a_{\perp,(Ga,Mn)As} - 0.5658}{4.6667 \cdot 10^{-4}}. \tag{3.7}$$

This method is only accurate to about 1%, because defects caused by the low temperature growth also influence the lattice constant of the material.

3.5.2 Reciprocal Space Maps

As shown in the previous section, ω-2Θ scans of the (004) reflection can only probe the vertical lattice constant of a sample. However, it is often important to make use of a reciprocal space map (RSM) around an asymmetric reflection to investigate the in-plane lattice constants as well. One application is the determination of the degree of relaxation of strained layers [Reß 98].

Fig. 3.9 illustrates the positions of peaks in the reciprocal space for different strain conditions. The crystal lattice of the substrate (or any unstrained cubic crystal) forms an image in reciprocal space which again has a cubic symmetry. If the lattice constant is a_{sub}, the reciprocal lattice constant is given by $1/a_{sub}$. By epitaxially growing a layer with a larger lattice constant onto this substrate, the layer is forced to match the lateral lattice constant of the substrate. Due to the Poisson effect, this leads to an extension of the lattice in growth direction. The reciprocal lattice of such a layer will therefore have the same lateral lattice constant a_{par}, and a smaller vertical lattice constant a_{vert}, since it translates to $1/a_{vert}$ in reciprocal space. When at some point the layer is fully relaxed (and has reached its bulk lattice constant), the reciprocal lattice points will have a smaller spacing in both directions than the substrate.

Combining the three lattices in the upper half of Fig. 3.9 shows how the peak positions are located relative to each other for different reflections. The zoomed section corresponds to the (044) reflection. The three peaks form a triangle in which the line connecting the pseudomorphic and the relaxed peak position is the line of relaxation. Since the transition between the pseudomorphic case and the fully relaxed case is not abrupt, the peak of a partially relaxed layer can be found at any point on the line of relaxation between the two cases, depending on the degree of relaxation. Mapping the reciprocal space containing the relaxation triangle is therefore a powerful tool to investigate strained layers [Hein 95, Schu 04]. By finding the layer peak on the line of relaxation, one can calculate the degree of relaxation for biaxially relaxed layers. It is also possible to determine the lattice constant (and therefore the strain) in one specific
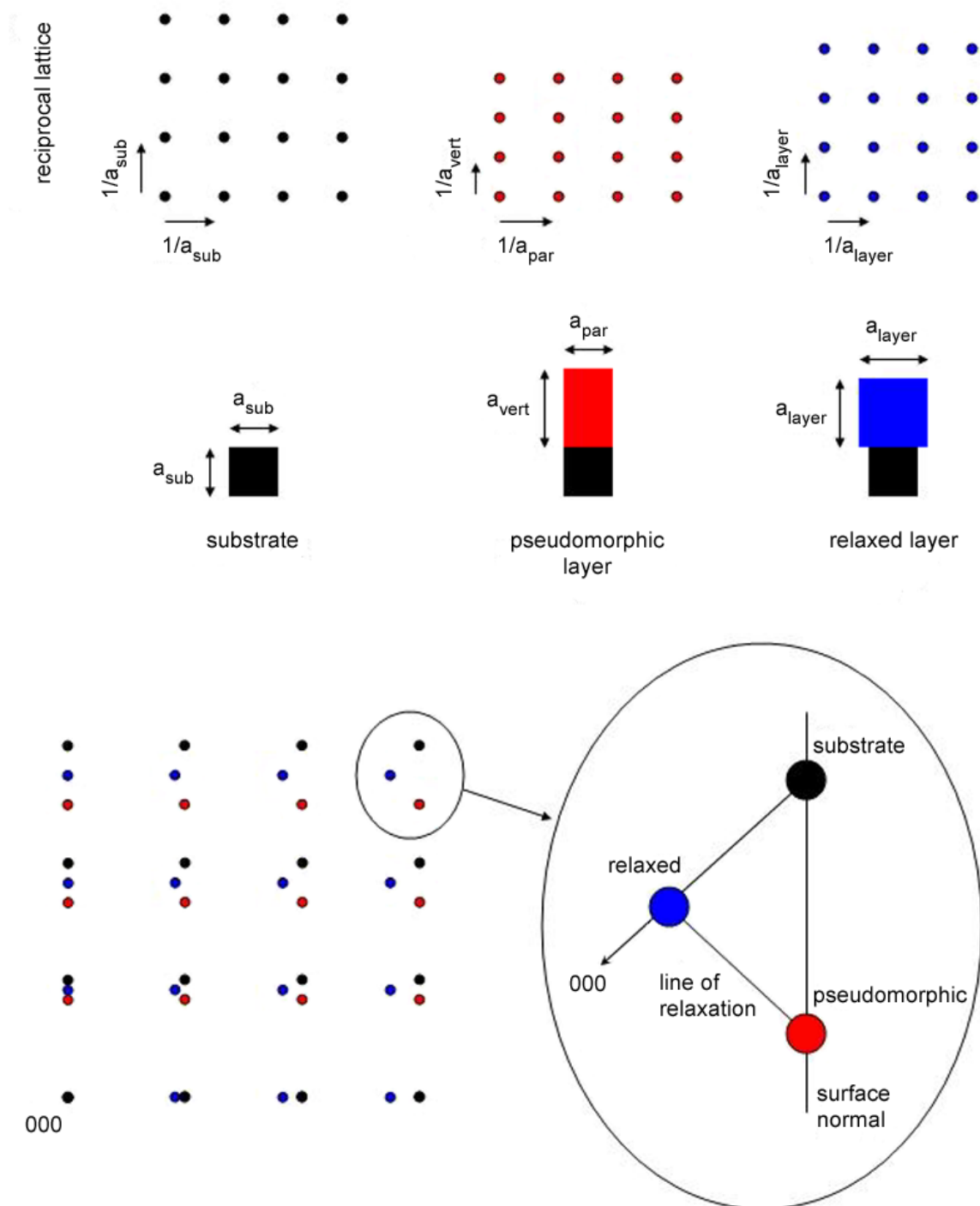
Figure 3.9: Reciprocal lattice for a cubic substrate (black), a pseudomorphic layer (red) and a fully relaxed cubic layer (blue). The lower half shows a combination of the above three cases, the zoomed section corresponds to the (044) reflection with the triangle of relaxation.

lattice direction by measuring a reflection that is sensitive to only one in-plane lattice direction, such as for example (206).

A map of the reciprocal space is assembled by a number of line scans along a scan axis. Each such scan is offset by a small step in a second axis, called the area axis. Possible choices for these axes are ω, 2Θ, and ω-2Θ. The best choice of axes depends on the specific reflection and the area which needs to be measured. Usually it is a pair of axes which most efficiently spans a reciprocal space area containing the whole region of interest.

Reciprocal Lattice Units

A RSM is usually depicted as a 2D cut plane in reciprocal space. The coordinates in a RSM have a component perpendicular to the sample surface $q_\perp$ and a component parallel to the surface $q_\parallel$. For the scaling of RSMs, we use reciprocal lattice units (r.l.u.), a dimensionless representation of rational Miller indices (hkl) with respect to the Miller indices of the substrate. For a layer where both in-plane directions h and k are equal, the conversion between the reciprocal lattice constant q and the real space lattice constant a is given by:

$$\begin{pmatrix} q_\parallel \\ q_\parallel \\ q_\perp \end{pmatrix} = \begin{pmatrix} h \\ k \\ l \end{pmatrix} \cdot \begin{pmatrix} \frac{a_{sub}}{a_\parallel} \\ \frac{a_{sub}}{a_\parallel} \\ \frac{a_{sub}}{a_\perp} \end{pmatrix} \tag{3.8}$$

With this equation it is immediately possible to relate a reciprocal space peak position measured in r.l.u. with a real space in-plane and perpendicular-to-plane lattice constant for a given reflection. With this relation and the information from Fig. 3.9, it is also easy to calculate the corners of the relaxation triangle, see table 3.1.

Table 3.1: Reciprocal space coordinates for the corner points of a relaxation triangle of an epitaxial layer. For a GaAs substrate, $a_{sub} = 5.6533$ Å.

position	real space	reciprocal space $(q_\parallel, q_\perp)$
substrate	$a_\parallel = a_\perp = a_{sub}$	(h, l)
pseudomorphic	$a_\parallel = a_{sub}$, $a_\perp = a_{vert}$	$(h, l \cdot \frac{a_{sub}}{a_{vert}})$
relaxed	$a_\parallel = a_\perp = a_{layer}$	$(h \cdot \frac{a_{sub}}{a_{layer}}, l \cdot \frac{a_{sub}}{a_{layer}})$

Example of RSM

To illustrate the application of a RSM, we present the measurement on a GaAs/ (In,Ga)As/(Ga,Mn)As structure. The goal of this sample was to achieve an out of plane easy axis of the magnetization, as described in Chapter 1, by growing (Ga,Mn)As under tensile strain. To achieve this strain situation, the (In,Ga)As layer was grown to a thickness of 1 μm, to allow plastic relaxation of the layer, and thereby forming a substrate for the (Ga,Mn)As layer with a larger lattice constant than the relaxed lattice constant of (Ga,Mn)As.
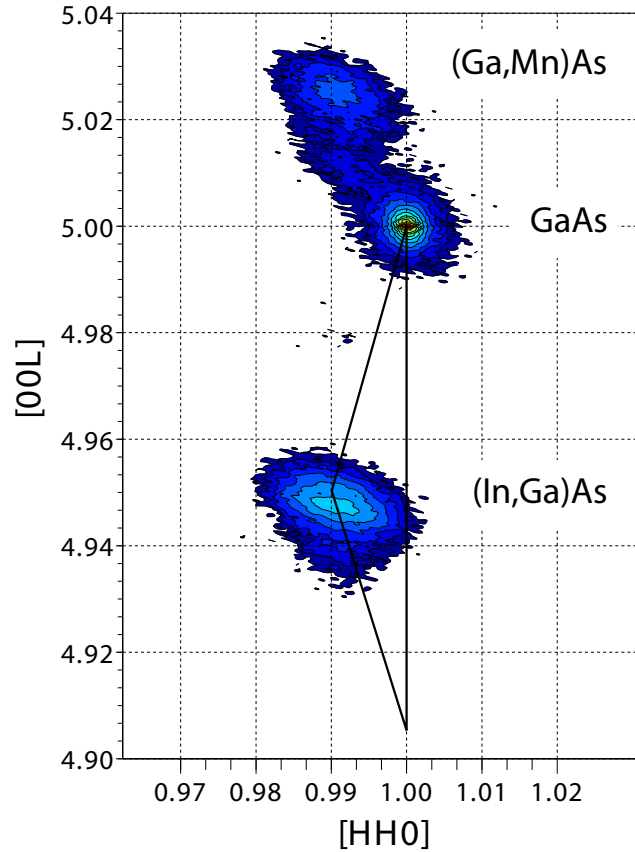
Figure 3.10: RSM of the (115) reflection of a GaAs/(In,Ga)As/(Ga,Mn)As structure. The scan axis is 2Θ (331 data points each scan) and area axis is ω (153 scans), with an integration time per step of 1 s. The relaxation triangle for the (In,Ga)As peak is marked in black.

Since the (In,Ga)As layer is not pseudomorphic to the substrate, ω-2Θ scans are no longer sufficient to investigate the whole strain situation. Fig. 3.10 shows a RSM of the (115) reflection of the sample. The map is centered of on the GaAs peak with $h = 1$, $k = 1$, $l = 5$. In all maps with $h = k$, we scale the x-axis by a factor of $1/\sqrt{2}$ because we actually measure the lattice constant along a $\langle 110 \rangle$ direction.

Due to its larger lattice constant, the peak of the (In,Ga)As layer is situated below the GaAs peak. For the fully pseudomorphic case, the peak would be located at the bottom tip of the relaxation triangle. The fact that the peak is almost at the fully relaxed corner of the relaxation line indicates the large degree of relaxation of the layer. We can calculate the degree of relaxation and the lattice constant for this layer as follows. From calibration samples, we know that the In contend in the (In,Ga)As layer is 14%, which corresponds to a bulk lattice constant (Vegard´s law) of 5.71 Å [IOFFE]. The position of the (In,Ga)As peak is located at $(q_\parallel, q_\perp) = (0.9907, 4.9475)$. According to Eqn. (3.8), this translates into the lattice constants $a_\parallel = 5.7063$ Å and $a_\perp = 5.7132$ Å, where $a_\parallel$ refers to the two in-plane directions [100] and [010].

We define the degree of relaxation γ as the quotient of the difference between the in-plane lattice constant $a_\parallel$ and the relaxed lattice constant a_{rel}, both relative to the

substrate lattice constant a_{sub}:

$$\gamma = \frac{\frac{a_\parallel - a_{sub}}{a_{sub}}}{\frac{a_{rel} - a_{sub}}{a_{sub}}} = \frac{a_\parallel - a_{sub}}{a_{rel} - a_{sub}}. \tag{3.9}$$

With this equation, we calculate a degree of relaxation for the (In,Ga)As layer of $\gamma = 0.93$, which is very close to full relaxation ($\gamma = 1$).

The (Ga,Mn)As layer is expected to grow pseudomorphically on the relaxed (In,Ga)As buffer, which is verified by the peak position of the (Ga,Mn)As layer in Fig. 3.10. The peak is located at the same h value as the underlying buffer and therefore shares its lateral lattice constant. Its vertical position of $q_\perp = 5.0251$ corresponds to $a_\perp = 5.6250$ Å, which is smaller than the lattice constant of GaAs. Again, the Poisson effect explains this behavior, as the in-plane tensile strain leads to a shrinkage of the (Ga,Mn)As lattice in the vertical direction.

Magnetic characterization of this sample reveals no clear out of plane easy axis. Rather, only a component of the magnetization was found in [001] direction, which leads to the conclusion that the magnetization is oriented at some oblique angle to the sample surface plane. Additionally, we have observed an anisotropic tilting of the lattice planes as reported by Grundmann et. al. [Grun 89], which has to be taken into account when interpreting XRD measurements on such samples.

Chapter 4

Finite Element Simulations of Strain Relaxation

To study the complex interaction between crystalline and magnetic properties of (Ga,Mn)As, a fundamental understanding of the mechanisms governing the strain relaxation behavior in this material is essential. In the following, we present finite element calculations which constitute a powerful tool in the investigation of the structures involved in this work.

Due to the considerable processing time of samples containing large stripe arrays, it is necessary to develop a method which allows reliable predictions about the relaxation in the patterned structures. With such a method, it is possible to optimize critical parameters before growth and patterning of the actual sample. The principal focus lies on predicting the extend and shape of strain relaxation, achieving homogeneity of strain throughout the structure, and high reproducibility of samples due to limited dependence of experimental results on small fluctuations in sample growth or processing.

The simulations are based on the stress/strain equations of elastic continuum mechanics, which will be discussed in the following section. For the actual calculations, we use the finite element simulation software FlexPDE (version 5.0.7). In this program a three-dimensional grid is defined, with individual material parameters for selected regions. For the numerical calculation, the grid is filled with a tetrahedral finite element mesh of points at which the equations are solved. The result is finally presented as diagrams. Simulated values on arbitrary cut planes through the 3D volume can be exported in tabular form.

4.1 Derivation of the Equation System

4.1.1 The Strain Coefficients

Consider the elastic properties of a crystal as a homogeneous continuous medium rather than as a periodic array of atoms [Kitt 05]. Further, we consider only small strains such that Hooke's Law stating that strain is directly proportional to the stress is valid. Let three orthogonal vectors $\hat{\mathbf{x}}$, $\hat{\mathbf{y}}$, $\hat{\mathbf{z}}$ of unit length be the basis of our coordinate system. After a small deformation of the solid, the axes are distorted in orientation

and length. The new axes $\mathbf{x}'$, $\mathbf{y}'$, $\mathbf{z}'$ may be written in terms of the old axes:

$$
\begin{aligned}
\mathbf{x}' &= (1 + \boldsymbol{\epsilon}_{xx})\hat{\mathbf{x}} + \boldsymbol{\epsilon}_{xy}\hat{\mathbf{y}} + \boldsymbol{\epsilon}_{xz}\hat{\mathbf{z}} \\
\mathbf{y}' &= \boldsymbol{\epsilon}_{yx}\hat{\mathbf{x}} + (1 + \boldsymbol{\epsilon}_{yy})\hat{\mathbf{y}} + \boldsymbol{\epsilon}_{yz}\hat{\mathbf{z}} \\
\mathbf{z}' &= \boldsymbol{\epsilon}_{zx}\hat{\mathbf{x}} + \boldsymbol{\epsilon}_{zy}\hat{\mathbf{y}} + (1 + \boldsymbol{\epsilon}_{zz})\hat{\mathbf{z}}
\end{aligned}
\tag{4.1}
$$

The coefficients $\boldsymbol{\epsilon}_{\alpha\beta}$ define the deformation; they are dimensionless and have values $\ll 1$ for small strains. The effect of the deformation (4.1) on an atom with the original position described by $\mathbf{r} = x\hat{\mathbf{x}} + y\hat{\mathbf{y}} + z\hat{\mathbf{z}}$ is such that its position after the deformation will be $\mathbf{r}' = x\mathbf{x}' + y\mathbf{y}' + z\mathbf{z}'$. The displacement $\mathbf{R}$ of the deformation is therefore defined by

$$
\mathbf{R} \equiv \mathbf{r}' - \mathbf{r} = x(\mathbf{x}' - \hat{\mathbf{x}}) + y(\mathbf{y}' - \hat{\mathbf{y}}) + z(\mathbf{z}' - \hat{\mathbf{z}}).
\tag{4.2}
$$

Or, using (4.1),

$$
\begin{aligned}
\mathbf{R}(\mathbf{r}) \equiv (x\boldsymbol{\epsilon}_{xx} + y\boldsymbol{\epsilon}_{yx} + z\boldsymbol{\epsilon}_{zx})\hat{\mathbf{x}} &+ (x\boldsymbol{\epsilon}_{xy} + y\boldsymbol{\epsilon}_{yy} + z\boldsymbol{\epsilon}_{zy})\hat{\mathbf{y}} \\
&+ (x\boldsymbol{\epsilon}_{xx} + y\boldsymbol{\epsilon}_{yz} + z\boldsymbol{\epsilon}_{zz})\hat{\mathbf{z}}.
\end{aligned}
\tag{4.3}
$$

This definition may be written in a more general form by introducing the displacements u, v, w along the (original) coordinate axes such that the displacement is given by

$$
\mathbf{R}(\mathbf{r}) = u(\mathbf{r})\hat{\mathbf{x}} + v(\mathbf{r})\hat{\mathbf{y}} + w(\mathbf{r})\hat{\mathbf{z}}.
\tag{4.4}
$$

The u, v, w are related to the local strains by taking the origin of $\mathbf{r}$ close to the region of interest and comparing (4.3) with (4.4), using Taylor series expansion of $\mathbf{R}$, with $\mathbf{R}(0) = 0$, and neglecting terms of order ϵ^2. This leads to

$$
x\boldsymbol{\epsilon}_{xx} = x\frac{\partial u}{\partial x}; \qquad y\boldsymbol{\epsilon}_{yx} = y\frac{\partial u}{\partial y}; \qquad \text{etc.}
\tag{4.5}
$$

In the following, we will work with the nonvectorial coefficients $e_{\alpha\beta}$ rather than $\boldsymbol{\epsilon}_{\alpha\beta}$, and define the first three strain components by the relations

$$
e_{xx} \equiv \boldsymbol{\epsilon}_{xx} = \frac{\partial u}{\partial x}; \qquad e_{yy} \equiv \boldsymbol{\epsilon}_{yy} = \frac{\partial v}{\partial y}; \qquad e_{zz} \equiv \boldsymbol{\epsilon}_{zz} = \frac{\partial w}{\partial z}.
\tag{4.6}
$$

The remaining strain components e_{xy}, e_{yz}, e_{zx} are defined in terms of the changes in angle between the axes. Using (4.1) we define

$$
\begin{aligned}
e_{xy} &\equiv \frac{1}{2}(\mathbf{x}' \cdot \mathbf{y}') \cong \frac{1}{2}(\boldsymbol{\epsilon}_{yx} + \boldsymbol{\epsilon}_{xy}) = \frac{1}{2}\left(\frac{\partial u}{\partial y} + \frac{\partial v}{\partial x}\right); \\
e_{yz} &\equiv \frac{1}{2}(\mathbf{y}' \cdot \mathbf{z}') \cong \frac{1}{2}(\boldsymbol{\epsilon}_{zy} + \boldsymbol{\epsilon}_{yz}) = \frac{1}{2}\left(\frac{\partial v}{\partial z} + \frac{\partial w}{\partial y}\right); \\
e_{zx} &\equiv \frac{1}{2}(\mathbf{z}' \cdot \mathbf{x}') \cong \frac{1}{2}(\boldsymbol{\epsilon}_{zx} + \boldsymbol{\epsilon}_{xz}) = \frac{1}{2}\left(\frac{\partial u}{\partial z} + \frac{\partial w}{\partial x}\right).
\end{aligned}
\tag{4.7}
$$

The six dimensionless coefficients $e_{\alpha\beta}(= e_{\beta\alpha})$ completely define the strain.

4.1.2 Hooke's Law and Equilibrium Equations

In the previous section we have established the strain coefficients which completely describe the strain in a system. By using Hooke's law, we can calculate the stresses acting on the material for a given set of strain coefficients. Hooke's law is valid for elastic deformations caused by small strains. In its most general form it reads

$$\sigma_{ij} = C_{ijkl}\left(e_{kl}\right). \tag{4.8}$$

There are six independent stress coefficients $\sigma_{\alpha\beta}(=\sigma_{\beta\alpha})$ which represent forces acting on a unit area of the solid. Three coefficients $(\sigma_{xx}, \sigma_{yy}, \sigma_{zz})$ represent a force applied in one of the cubic directions to a unit area of a plane whose normal lies in the same direction. The remaining three coefficients $(\sigma_{xy}, \sigma_{yz}, \sigma_{xz})$, which we will refer to as τ instead of σ in the following, are called shear stresses and represent forces acting parallel to a surface area. The quantities C_{ijkl} appearing in (4.8) are the elastic stiffness constants or moduli of elasticity. The C's have the dimensions of [force]/[area] and form a 4th order tensor. It can be shown [Kitt 05] that for a cubic crystal, the number of independent elastic stiffness constants is reduced to three:

$$\begin{pmatrix} C_{11} & C_{12} & C_{12} & 0 & 0 & 0 \\ C_{12} & C_{11} & C_{12} & 0 & 0 & 0 \\ C_{12} & C_{12} & C_{11} & 0 & 0 & 0 \\ 0 & 0 & 0 & C_{44} & 0 & 0 \\ 0 & 0 & 0 & 0 & C_{44} & 0 \\ 0 & 0 & 0 & 0 & 0 & C_{44} \end{pmatrix} \tag{4.9}$$

The full set of stresses, as calculated from (4.8) and (4.9) is therefore:

$$\begin{aligned} \sigma_{xx} &= C_{11}e_{xx} + C_{12}e_{yy} + C_{12}e_{zz} \\ \sigma_{yy} &= C_{12}e_{xx} + C_{11}e_{yy} + C_{12}e_{zz} \\ \sigma_{zz} &= C_{12}e_{xx} + C_{12}e_{yy} + C_{11}e_{zz} \end{aligned} \tag{4.10}$$

The shear stresses are:

$$\begin{aligned} \tau_{xy} &= 2C_{44}e_{xy} \\ \tau_{yz} &= 2C_{44}e_{yz} \\ \tau_{xz} &= 2C_{44}e_{xz} \end{aligned} \tag{4.11}$$

With the stresses we can formulate the equilibrium equations of 3D elasticity using the principle of conservation of linear momentum i.e., Newtons's second law. We will neglect external body forces for now and write:

$$\begin{aligned} \frac{\partial \sigma_x}{\partial x} + \frac{\partial \tau_{xy}}{\partial y} + \frac{\partial \tau_{xz}}{\partial z} &= 0 \\ \frac{\partial \tau_{xy}}{\partial x} + \frac{\partial \sigma_y}{\partial y} + \frac{\partial \tau_{yz}}{\partial z} &= 0 \\ \frac{\partial \tau_{xz}}{\partial x} + \frac{\partial \tau_{yz}}{\partial y} + \frac{\partial \sigma_z}{\partial z} &= 0 \end{aligned} \tag{4.12}$$

The solution of the equilibrium equations fully defines the six independent stress components throughout a structure. These equations are the basis for the finite element

simulation. However, in general, these equations cannot be solved without introducing additional equations. In the next section we will modify the stress equations (4.10) to model strain introduced into epitaxial layers by lattice-mismatched growth, which will also lead to a set of equations which can be solved numerically.

4.1.3 Lattice Mismatch Strain as Isotropic Internal Pressure

Remember, that the structures we want to simulate consist of pseudomorphically strained layers which are patterned into various shapes that allow unique strain relaxation. An epitaxially grown layer, which has a larger intrinsic lattice constant than the substrate it is grown on, is subject to compressive strain in the layer plane. This results in an internal force, working to expand the lattice towards its equilibrium state. This force is equivalent to an internal isotropic pressure or to a higher temperature which increases the lattice constant via thermal expansion. We will make use of this analogy to model the lattice-mismatch induced strain as a dimensionless "temperature" T which will be a unique parameter for each individual layer. Since all layers are grown on GaAs substrates, we choose its lattice constant as the reference point and assign it a temperature of $T = 0$.

Let us assume now, that we have a material with a larger lattice constant than GaAs. The temperature we assign to this material expands a unit GaAs (the reference) volume to fit the larger intrinsic lattice constant of the new material. This means that the temperature acts as an additional isotropic stress bT on the unit volume. Using (4.10), we can write:

$$\sigma_{xx} + bT = C_{11}e_{xx} + C_{12}e_{yy} + C_{12}e_{zz} \qquad (4.13)$$

Since the pressure is isotropic, we only consider one stress direction, as all three are equivalent ($\sigma_{xx} = \sigma_{yy} = \sigma_{zz} = \sigma$). The same holds true for the strain parameters ($e_{xx} = e_{yy} = e_{zz} = e$). Note that this internal pressure does not cause shear strain. If the material is allowed to relax freely, the stress has to vanish in the resulting equilibrium state when the material reaches its intrinsic lattice constant. For this case we can rewrite (4.13) as:

$$
\begin{aligned}
0 &= C_{11}e_{xx} + C_{12}e_{yy} + C_{12}e_{zz} - bT = \sigma_{xx} \\
\Leftrightarrow \quad 0 &= e(C_{11} + 2C_{12}) - bT \\
\Leftrightarrow \quad e &= \frac{b}{C_{11} + 2C_{12}} \, T \qquad (4.14)
\end{aligned}
$$

From this equation, we can immediately see that the "temperature" T acts as a force on the material which translates into a strain e as determined by the material parameters C_{11} and C_{12} and the free parameter b. We choose b such that a $\Delta T = 1$ causes a $\Delta e = 1.0 \cdot 10^{-4}$:

$$1.0 \cdot 10^{-4} = \frac{b}{C_{11} + 2C_{12}} \, 1 \qquad (4.15)$$

For the elastic moduli of GaAs, this equation leads to $b = 2.26 \cdot 10^8 \, \frac{dyn}{cm^2}$. Instead of e we can write the lattice mismatch f, and are now able to set any lattice mismatch between a layer material and GaAs in steps of $1.0 \cdot 10^{-4}$ by increasing T by 1.

4.2 The FlexPDE Software

4.2.1 The Simulation File

This section will give a very brief overview of the composition of a FlexPDE simulation descriptor file. For detailed information about the capability and command syntax of this software the reader should refer to the user manual. A complete input file for a 3D GaAs/(Ga,Mn)As stripe can be found in Appendix B as a working example. The problem description is given in the form of a readable text file, which consists of a number of sections identified by headers. The relevant sections for the sample in Appendix B are as follows.

Title This sections sets a label for the graphic output plots.

Select Contains a list of user specifications of the global behavior of FlexPDE such as calculation accuracy control or general plot options.

Coordinates Sets the coordinate system, in our case 3-dimensional cartesian coordinates.

Variables Names the dependent variables used in the partial differential equations.

Definitions Defines ancillary parameters, functions and relations. As can be seen in Appendix B, this includes the physical dimensions of the sample, material parameters such as elastic moduli and finally definition of the strain coefficients (4.6) and (4.7), the stresses (4.10), and shear stresses (4.11).

Equations Defines the partial differential equation system in which each equation is associated with a dependent variable. In our case, the displacements u, v, w are linked with the equilibrium equations (4.12).

Extrusion Extends 2D domains into tree dimensions.

Boundaries The geometry of a number of 2D regions is defined by walking the perimeter of a domain, stringing together line or arc segments to bound the figure. Individual parameters can be set to characterize the material of a region. This section also allows for the incorporation of boundary conditions i.e., locked values for parameters at surfaces or edges.

Plots Contains a list of requested graphic outputs and data exports in the form of ASCII tables.

The geometry of a sample is defined in the sections **Extrusion** and **Boundaries**. Fig. 4.1 shows the outline grid of a GaAs/(Ga,Mn)As stripe. First, we need to define the relevant surfaces of the structure along the z-axis, starting with the bottom of the substrate at $z = 0$. The first height step would be $z = h_{sub}$, the surface which contains
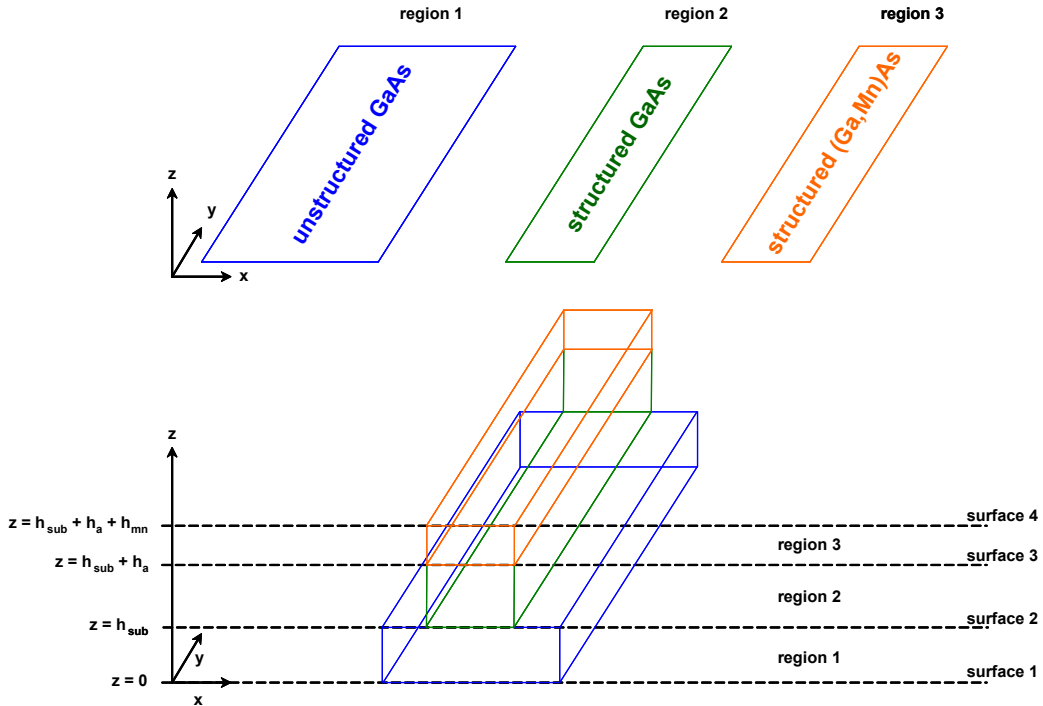
Figure 4.1: Schematic FlexPDE grid of a GaAs/(Ga,Mn)As stripe. Three regions in the x-y-plane (top) defined in the Boundaries section are extended into the z-direction in the Extrusion section (bottom).

the bottom of the etch trenches between the stripes. This step equals the total height of the unstructured material. Its thickness is chosen such, that it is larger than the extend of strain fields into the substrate to avoid edge effects. The following region of etched GaAs extends up to the (Ga,Mn)As layer, which begins at $z = h_{sub} + h_a$. The last step is the (Ga,Mn)As layer itself, terminating at the top of the sample at $z = h_{sub} + h_a + h_{mn}$. Each of these surfaces is associated with a region which is defined by its outline in the x-y-plane in the **Boundaries** section. The space between two subsequent surfaces is filled with the region pertaining to the lower surface.

4.2.2 Simulation Parameters

This section compiles a list of all relevant parameters which are used in the simulations throughout this thesis. Unless otherwise noted, all presented simulation data can be considered to be on the basis of the following values. The elastic moduli C_{ij} for GaAs are used for all sample materials, since the deviation due to Mn or In admixture to a GaAs layer is negligible. The parameter b discussed in Section 4.1.3 is fully determined by the C_{ij}. Table 4.1 lists the values for the C_{ij} as taken from [IOFFE].

Further required parameters are more sample specific. The parameters w and l set the width and length of a stripe in the x-y-plane. The height steps are h_{sub} (height of the unstructured GaAs), h_a (height of the structured GaAs), and h_{mn} (height of the (Ga,Mn)As layer).

As mentioned earlier, we assume that all layers have the same elastic properties. Consequently, different layers are only differentiated by their bulk lattice constants.

Table 4.1: Some material parameters.

parameter	value $\left[\frac{dyn}{cm^2}\right]$
C_{11}	$11.90 \cdot 10^{11}$
C_{12}	$5.34 \cdot 10^{11}$
C_{44}	$5.96 \cdot 10^{11}$
b	$2.26 \cdot 10^{8}$

Therefore we assign each layer a "temperature" value T_p as described in Section 4.1.3. Since GaAs is our reference point for the lattice constant, its temperature is $T_p = T_{Ga} = 0$. In the example in Appendix B, we simulate a (Ga,Mn)As layer with a Mn-content of 2.5 %, which is equal to a lattice mismatch of $f = 1.5 \cdot 10^{-3}$ to the underlying GaAs layer. This lattice mismatch is represented by $T_p = T_{Mn} = 15$.

4.2.3   Graphical Output

Three forms of graphical output of the simulation data were used in this study, see Fig. 4.2 for examples. For a qualitative impression of the relaxation and resulting lattice distortion, the grid command produces a picture of the whole structure, either in 3D or of a 2D cut plane through the structure (Fig. 4.2 (a) and (b)). Usually it is necessary to amplify the lattice distortion (here by a factor 100) because of the small size of the distortion relative to the physical dimensions of the structure. Similar to this depiction is the vector plot of the displacement vectors (Fig. 4.2 (c)).

Graphical presentation of the strain parameter is achieved via color-coded contour plots (Fig. 4.2 (d)–(f)). For this kind of plot it is required to define an arbitrary cut plane through the structure on which the data is plotted. The cut plane can be restricted to regions as defined in the Boundaries step. In the simulation, the strain parameter for any layer has its reference point at the bulk lattice constant of GaAs. However, it is customary to specify the strain parameter of a layer relative to the bulk lattice constant of the material the layer is composed of. To achieve this, the calculated strain has to be corrected by an offset equal to the lattice mismatch.

4.3   Simulation Results – Physical Dimensions

To study the influence of lattice strain on the magnetic properties of (Ga,Mn)As, it is essential to first acquire a detailed understanding of how lithographic patterning induces lattice relaxation in nanostructures. By structuring a layer into a stripe pattern, we locally remove constricting material to allow uniaxial lattice relaxation perpendicular to the stripes, see Fig. 4.2 (a) and (b). The current section is dedicated to simulations in which effects of changes of the physical dimensions of stripe structures on the lattice relaxation are investigated. Our coordinate system (see Fig. 4.3) is chosen such, that the x-axis coincides with the [010] crystal direction and the y-axis with the [100] direction. The growth direction (z-axis) is [001].
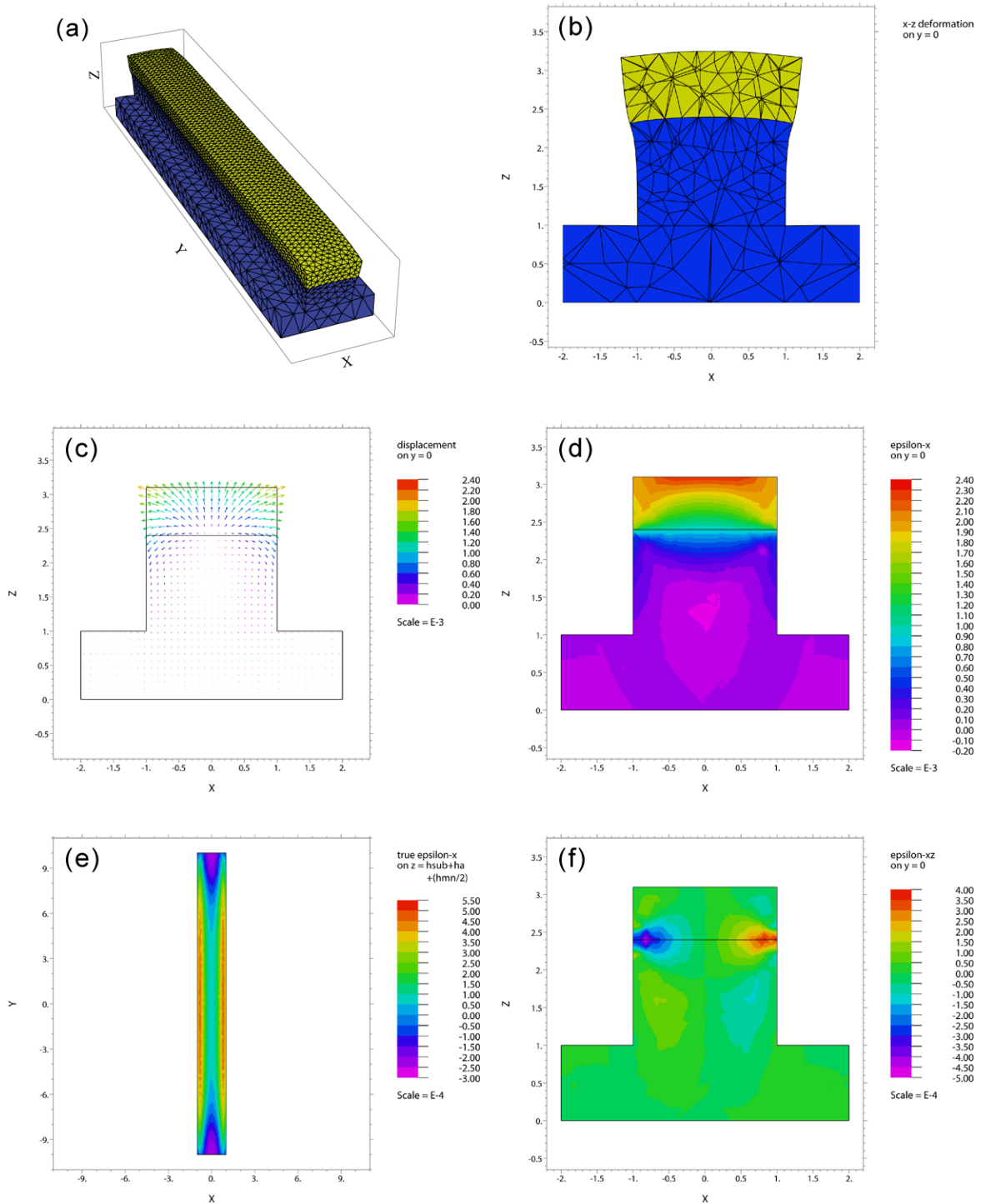
Figure 4.2: Examples of simulation data plots for a GaAs/(Ga,Mn)As stripe. Representation of (a) the relaxed structure in 3D and (b) on a x-z-plane through $y = 0$ (both the displacements are $100\times$ exaggerated). (c) displacement vector plot; (d) strain e_x in x-direction (relative to a_{GaAs}); (f) top view of the strain e_x relative to $a_{(Ga,Mn)As}$ on a horizontal cut plane through the middle of the (Ga,Mn)As layer; (f) shear strain e_{xz}.
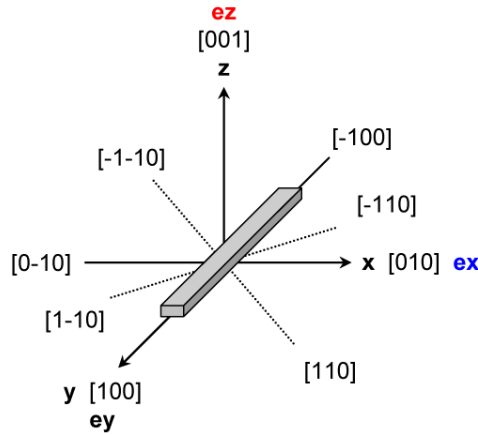
Figure 4.3: Crystal directions for a stripe along [100] with the corresponding cartesian coordinates of the simulation coordinate system. The strain e_y is fixed at the pseudomorphic limit. The relaxation axes are x (e_x), and z (e_z).

In the following we will consider stripes of (Ga,Mn)As on GaAs or GaAs/(In,Ga)As aligned along the [100] crystal direction. In the actual processed samples, their length is 100 μm with a width of 200 nm. However, such a large volume is impractical for numerical simulations. Therefore we limit ourselves to a length to width ratio of 5 for most cases, which is sufficient to ensure that no effects due to finite stripe length influence the simulation in the center region of the stripe. Furthermore, we simulate only a relatively thin (100 nm) region of the unstructured bottom layer, as it does not significantly influence the strain relaxation in the stripes.

It is important to note that the whole equation system governing the lattice relaxation is completely scale invariant. Any structure with given physical dimensions will produce an identical strain distribution to a structure in which the physical dimensions have been multiplied by an arbitrary scaling factor. As a consequence, we will often use the relative width of a simulated layer instead of concrete values when discussing variations in physical parameters. We define the relative width rw of a layer as the width w of a stripe divided by the thickness (height) h of the material we are interested in:

$$rw = \frac{w}{h} \tag{4.16}$$

Thus, a value of $rw = 5$ describes the strain in a layer of $w = 100$ nm and $h = 20$ nm, as well as in any other layer where w and h are multiplied by an arbitrary scaling factor.

The values shown in the following plots are calculated by taking the average value (or its standard deviation) of a simulation parameter over a cut plane through the region of interest of a sample. At the commonly used simulation accuracy, such a cut plane contains 2601 data points.

4.3.1 Relative Width

At first, we will examine how the relative width rw of a (Ga,Mn)As stripe impacts on the strain distribution within the layer. By varying the parameter rw over a series of
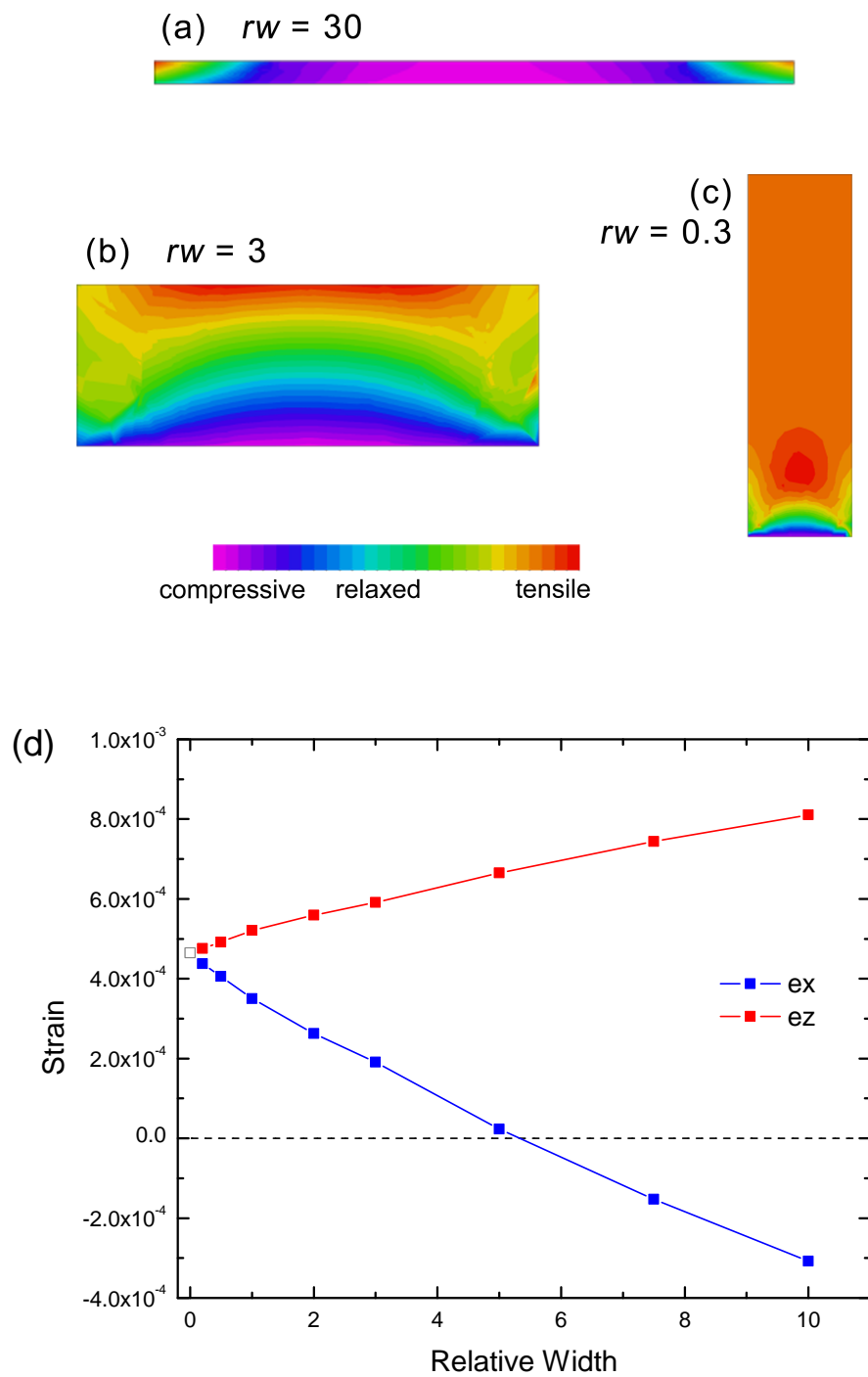
Figure 4.4: (a)–(c) Strain e_x in the cross-section of a (Ga,Mn)As (2.5% Mn, $h_a = 200$ nm) stripe for three selected values of rw. (d) dependence of average strain on the relative width in a GaAs/(Ga,Mn)As stripe. The open gray square at $rw = 0$ represents the extrapolated strain towards the border case of $rw \to 0$.

simulations and evaluating the average strain e_x and e_z in a cross-section of the layer, we obtain the plot in Fig. 4.4 (d). To illustrate how the strain distribution evolves with rw, the figure also shows color coded cross-section strain maps of stripes with three selected values of rw. To understand how the relative width influences the strain, it is helpful to first consider the two extreme cases:

1. A large value of rw describes a very thin but very wide stripe, which approaches the case of an epitaxial layer without any structuring.

2. A small value of rw, which corresponds to a very narrow and high stripe.

For the first case, Fig. 4.4 (a) shows that the center region of the layer retains a high degree of compressive strain. In fact, no strain relaxation can take place there at all for large enough widths, as the substrate material prevents horizontal strain relaxation. The largest strain relaxation is visible in the side wall regions, which constitute only a small fraction of the total volume of the layer. The strain distribution is therefore dominated by the substrate layer. The average values for all three strains approach the value of a fully pseudomorphic layer. For the (Ga,Mn)As layer in Fig. 4.4 (d), these values are $e_x = e_y = -1.5 \cdot 10^{-3}$. By applying Hooke's law (Eqn. (4.8)), we find that the strain in z-direction is given by:

$$e_z = -\frac{2\nu}{1 - \nu}\frac{\Delta l}{l} \tag{4.17}$$

Here, $\Delta l / l$ is the relative difference between the relaxed lattice constant of (Ga,Mn)As and the lattice constant of GaAs as defined in Eqn. (2.2); ν is the Poisson ratio. With this equation we calculate a value of $e_z = 1.35 \cdot 10^{-3}$.

In the second case, the substrate layer influence declines as the interface region becomes small compared to the total volume of the stripe material. The interface region at the bottom of the layer is forced to match the lattice constant of the substrate, while the majority of the volume is free to relax in x- and z-direction. Apart from the interface region, the lattice constant will therefore be characterized by the uniaxial compression of the material along the y-direction. The transverse strain e_t, acting in x- and z-direction, is linked to the uniaxial compression by the Poisson ratio:

$$e_t = -\nu e_y \tag{4.18}$$

Fig. 4.4 (c) shows such a stripe where the upper two thirds of the structure are completely unaffected by the underlying GaAs. The strain in the upper region is, according to Eqn. (4.18), given by $e_x = e_z = 4.65 \cdot 10^{-4}$. For the border case of $rw \to 0$, both strains in Fig. 4.4 (d) converge to this value.

Concerning the three shear strains, the simulation results for e_{xy} and e_{yz} are of the order of 10^{-5} and are therefore assumed to be zero for any further calculations. The shear strain e_{xz} (see Fig. 4.2 (f)) reflects a bending of the lattice planes and reaches its maximum value of a magnitude of 10^{-4} around the side-walls of the GaAs/(Ga,Mn)As interface region. Due to the symmetry of the stripe, this shear strain has an opposite sign, depending if $x < 0$ or $x > 0$. The average value of e_{xz} in a cross-section of the stripe is therefore zero.

From this simulation series, we learn that the relative width of a (Ga,Mn)As stripe has the tendency to increase the total strain relaxation (compared to the unstructured case) perpendicular to the stripes for lower values. A transition from compressive to tensile in-plane strain takes place at $rw \approx 5$.
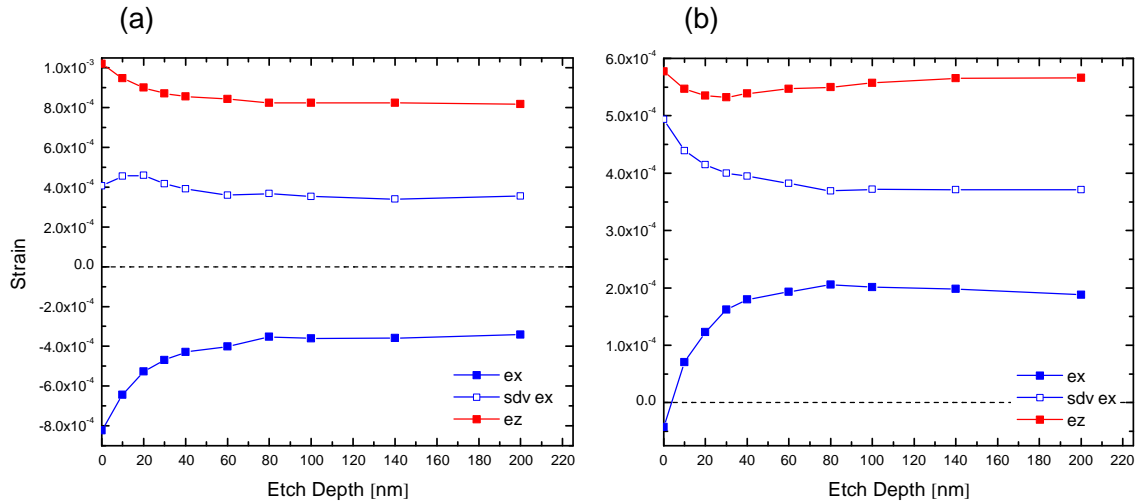
Figure 4.5: Strain dependence on etch depth h_a (into the substrate) in a 200 nm wide (Ga,Mn)As stripe ($f = 1.5 \cdot 10^{-3}$) of (a) 20 nm ($rw = 10$) and (b) 70 nm thickness ($rw = 2.9$) on GaAs. The standard deviation of e_x (sdv ex) is a measure for the homogeneity of the strain in the region.

4.3.2 Etch Depth

Another structural parameter which can be controlled during the fabrication process is the total height $h_a + h_{mn}$ of the stripes. We assume that the (Ga,Mn)As layer is always completely etched and will only vary the parameter h_a, which describes the etch depth into the substrate below the (Ga,Mn)As layer. In varying the etch depth h_a, as shown for two different layer thicknesses in Fig. 4.5, we see that a certain etch depth is necessary to achieve maximum relaxation.

For both layers, the strain in x- and z-direction becomes independent of the etch depth at around 80 nm. Further increase of h_a does not increase the strain relaxation. We conclude that for lower etch depths, the GaAs pillar on which the relaxing (Ga,Mn)As layer rests, is itself restricted by the underlying unstructured material and prevents maximal relaxation of the top layer. It is important to keep this fact in mind when simulating different structures, as the etch depth at which the strain relaxation attains its largest possible value for a given geometry may not be the same. It is also worth noting that, when reproducing a structure that is not yet in the maximum possible relaxation regime, small deviations in etch depth may result in a change in relaxation of the top layers.

We observe that the standard deviation of e_x is smaller for the 20 nm than for the 70 nm layer. The explanation lies in the fact that for a thicker layer, more relaxation is possible towards the upper surface, where the separation from the constricting bottom interface is largest. This leads to a strain gradient, which increases with layer thickness and therefore results in a larger standard deviation for such layers. For large etch depths, the standard deviation of both layers approaches a common value because the vertical strain gradient is replaced by a homogeneous relaxation of the majority of the stripe, with the remaining strain gradient confined to the side-edge regions of the stripe (see Fig.4.4 (a), (b) for the strain distribution in layers of different height).
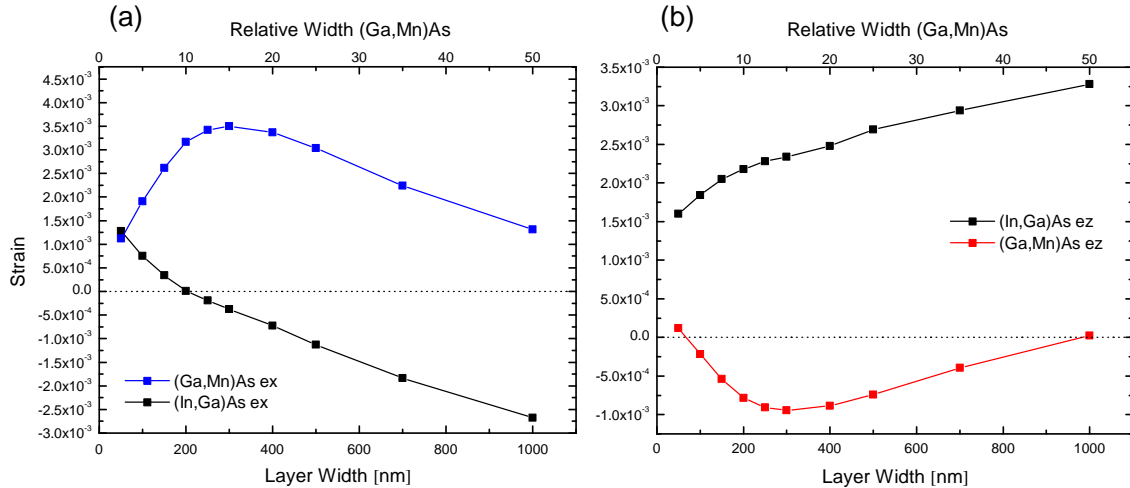
Figure 4.6: Strain dependance on stripe width in a patterned GaAs/(In,Ga)As/(Ga,Mn)As sample (7.4% In, $f_{In} = 5.3 \cdot 10^{-3}$; 2.5% Mn, $f_{Mn} = 1.5 \cdot 10^{-3}$). (a) strain e_x in x-direction, (b) strain e_z in z-direction.

4.4 Simulation Results – (In,Ga)As/(Ga,Mn)As

While the last section investigated the general impact of variations of the physical dimensions of the sample on the lattice strain, we will now use simulations to understand the strain distribution in a more complex sample design. The motivation for the following series of samples is to introduce an additional factor to the sample design, which can act to increase the strain. In the stripes simulated so far, the driving (and only) source of strain relaxation is the growth strain energy accumulated during MBE growth of the (Ga,Mn)As layer. By adding an additional, highly strained (In,Ga)As layer with much higher lattice mismatch than (Ga,Mn)As below the (Ga,Mn)As layer, we introduce an additional source of strain energy. We expect that by patterning-induced relaxation, the (In,Ga)As layer will assume a larger lattice constant than the bulk value for (Ga,Mn)As and therefore act as an additional stressor.

To estimate the effect of this stressor layer, we simulate the following sample design: A GaAs buffer layer is followed by a highly strained (In,Ga)As layer of 80 nm thickness and an In-content of 7.4% ($f_{In} = 5.3 \cdot 10^{-3}$). The top layer is composed of 20 nm (Ga,Mn)As with 2.5% Manganese ($f_{Mn} = 1.5 \cdot 10^{-3}$).

In this sample, the layer thickness of the (In,Ga)As layer is not a free parameter. It is chosen such that the layer is as close as possible to the onset of plastic strain relaxation before patterning for the given In-content. We will therefore use the stripe width instead of the relative width as the free simulation parameter, and keep the layer height fixed at $h_{In} = 80$ nm and $h_{Mn} = 20$ nm. The height of the (Ga,Mn)As layer is chosen to retain comparability with other (Ga,Mn)As layers.

As shown in Fig. 4.6, we simulate stripe widths between 50 nm and 1 μm. For the (In,Ga)As layer, we observe a result qualitatively very similar to the case of GaAs/(Ga,Mn)As stripes (Fig. 4.4). For large stripe widths, the strain approaches the case of an unstructured, pseudomorphic layer, with $e_x = e_y = -5.3 \cdot 10^{-3}$. The strain in z-direction is again given by Eqn. (4.17) and approaches a value of $e_z = 4.75 \cdot 10^{-3}$.

For very small w, y becomes the only pseudomorphic direction, with resulting lattice expansion in x- and z-direction. In neither border case is the average value of the strain of the (In,Ga)As layer altered by the (Ga,Mn)As layer.

For the (Ga,Mn)As layer, the strain dependence on layer width reveals a remarkable difference to the pure GaAs/(Ga,Mn)As case. First, we note that the behavior for large widths is not influenced by the stressor layer, which is easy to understand when we consider that the stressor layer itself is pseudomorphic for these conditions. Therefore the (Ga,Mn)As will see a substrate with the lateral lattice constant of GaAs, which it would also see if there was no stressor layer in the first place.

Coming from the high width limit, we observe significantly higher tensile strain in the (Ga,Mn)As layer with stressor. In a pure 20 nm (Ga,Mn)As layer, we would expect the transition from compressive to tensile strain to be around $w = 100$ nm ($rw = 5$, see Fig. 4.4). In the stressor layer stripe, a (Ga,Mn)As layer with $w = 1000$ nm already exhibits a large degree of tensile strain. The strain in z-direction is increased likewise.

The important feature is the maximum of the strain in the (Ga,Mn)As layer at around $w = 300$ nm. To understand this behavior, we examine the low w case. In this regime, the interface region between (In,Ga)As and (Ga,Mn)As contributes less influence to the total volume than for a wide, thin layer. The upper regions of the (Ga,Mn)As layer are consequently less subject to the tensile strain induced by the (In,Ga)As, resulting in a total decrease of e_x and the corresponding increase in e_z.

The etch depth is not as critical in this case as for a (Ga,Mn)As stripe without the stressor, as the (In,Ga)As layer negates the effects of the pillar height on the strain in the (Ga,Mn)As layer caused by small differences in the total etch depth. In conclusion, we can deduct, that for the given layer thicknesses and compositions, a stripe width of around 300 nm is most desirable, as it results in the largest possible strain in the (Ga,Mn)As layer on top of the (In,Ga)As layer.

4.5   Stripes Along $[1\bar{1}0]$

So far, we have only considered stripes which are aligned along the [100] direction, which corresponds to one of the intrinsic biaxial easy axes of magnetization in a (Ga,Mn)As epilayer. This configuration therefore allows us to study the influence of uniaxial strain relaxation on such an easy axis.

The next challenging question which arises is, how uniaxial strain relaxation impacts on the magnetic anisotropy, when it is applied under 45° to the easy axes, i.e. along a hard axis of magnetization. Simulations of a (Ga,Mn)As stripe along the $[1\bar{1}0]$ direction (see Fig. 4.7) reveals several notable differences to the previously studied geometry.

Along the long axis of the stripe, $[1\bar{1}0]$, the lattice constant is pseudomorphic to the substrate, analogous to the [100] stripe. The free relaxation directions are [001] and [110]. Contrary to the previous geometry, the strain components e_x and e_y are no longer aligned with the stripe axes. Due to the symmetry of the system, they are equal in sign and magnitude for this case, and both contribute equally to the relaxation perpendicular to the stripe. Important is the emergence of the shear strain component e_{xy}, which is not observed in the previous stripes.

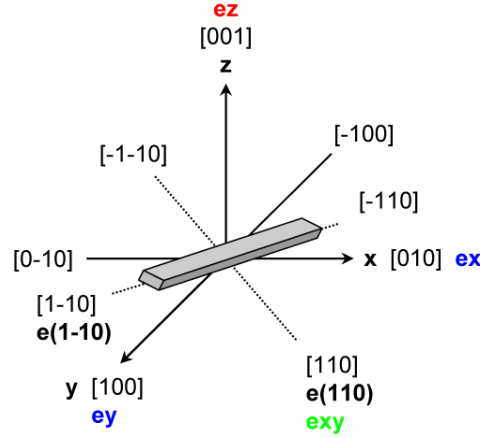For a volume conserving deformation of the crystal, the shear strain in a $[1\bar{1}0]$

Figure 4.7: Crystal directions and simulation coordinate system for a $\left[1\bar{1}0\right]$ stipe. Important strain components are indicated.

stripe would simply be equal to the strain along an in-plane cubic direction of a [100] stripe [Ibac 03]. However, for our case, we do not have a volume conserving deformation, since we keep the lattice fixed along the [1$\bar{1}$0] direction. Therefore, we have to compute the strain distribution in the relaxed stripes by one of the following two methods. The first is to transform the basis of the stress-strain equations (4.10) and (4.11) into the rotated coordinate system, so that x and y again match the directions perpendicular and parallel to the stripes. However, since we want to be able to directly compare the strains for both cases without transforming the axis directions, we make use of another method.

While retaining the previous coordinate system, we define the stripe area with an angle of 45° to the y-axis. The simulation calculations yield the strain components with respect to the coordinate axes, which we can write as the strain matrix E:

$$E = \begin{pmatrix} e_x & e_{xy} & 0 \\ e_{xy} & e_y & 0 \\ 0 & 0 & e_z \end{pmatrix} \qquad (4.19)$$

Here, $e_{xy} = e_{yx}$, with all other shear strain components being zero. To quantitatively compare the strain relaxation perpendicular to the stripe for both geometries, we rotate this matrix by -45° around the z-axis by applying the rotation matrix R, which leads to the new strain matrix E':

$$E' = R \ E \ R^T$$

$$E' = \begin{pmatrix} \frac{1}{\sqrt{2}} & \frac{1}{\sqrt{2}} & 0 \\ -\frac{1}{\sqrt{2}} & \frac{1}{\sqrt{2}} & 0 \\ 0 & 0 & 1 \end{pmatrix} \begin{pmatrix} e_x & e_{xy} & 0 \\ e_{xy} & e_y & 0 \\ 0 & 0 & e_z \end{pmatrix} \begin{pmatrix} \frac{1}{\sqrt{2}} & -\frac{1}{\sqrt{2}} & 0 \\ \frac{1}{\sqrt{2}} & \frac{1}{\sqrt{2}} & 0 \\ 0 & 0 & 1 \end{pmatrix}$$

$$E' = \begin{pmatrix} \frac{1}{2}(e_x + 2e_{xy} + e_y) & \frac{1}{2}(-e_x + e_y) & 0 \\ \frac{1}{2}(-e_x + e_y) & \frac{1}{2}(e_x - 2e_{xy} + e_y) & 0 \\ 0 & 0 & e_z \end{pmatrix} \qquad (4.20)$$
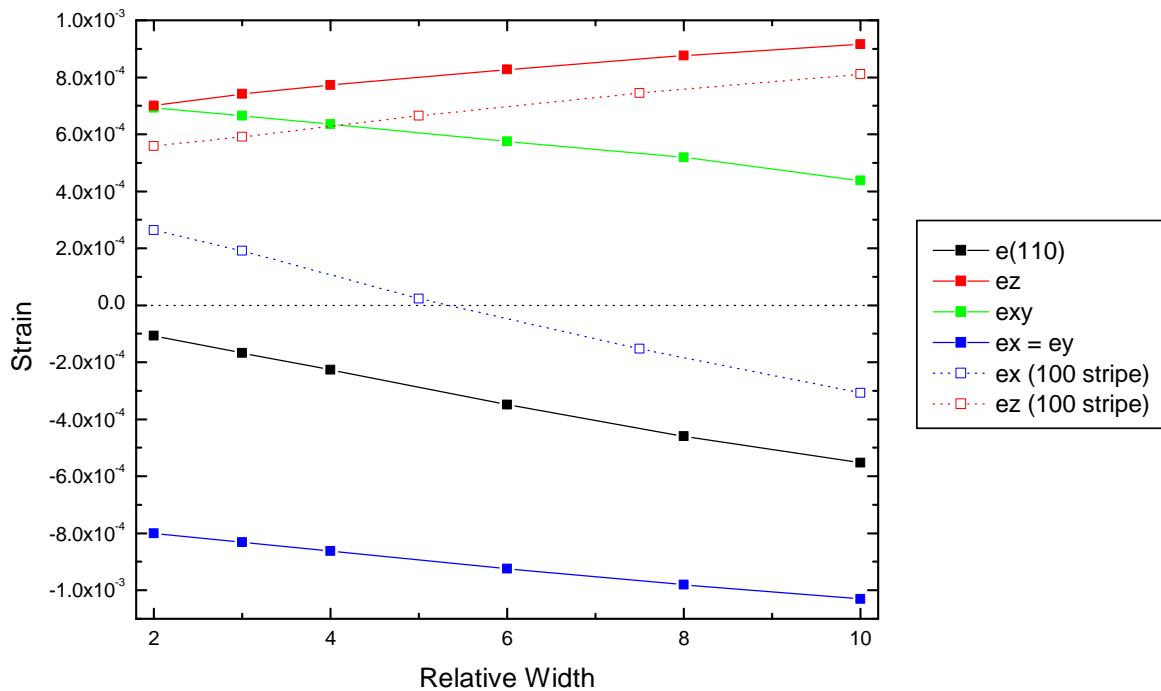
Figure 4.8: Simulation of the average strain in a (Ga,Mn)As stripe aligned along the $[1\bar{1}0]$ crystal direction. The solid lines represent the strain in the cubic directions (blue: $e_x = e_y$, red: e_z), the shear strain (green: e_{xy}), and the calculated relaxation perpendicular to the stripe axis (black: $e_{[110]}$). The dotted lines are the simulation results for an identical stripe aligned along [100], taken from Fig. 4.4.

By comparing Eqn. (4.19) and Eqn. (4.20), we can now identify:

$$e_{[1\bar{1}0]} = \frac{1}{2}(e_x - 2e_{xy} + e_y) \qquad (4.21)$$

$$e_{[110]} = \frac{1}{2}(e_x + 2e_{xy} + e_y) \qquad (4.22)$$

For the given material parameters of the stipe, the strain in $[1\bar{1}0]$ is equal to $-1.5 \cdot 10^{-3}$, as no strain relaxation takes place in this direction. The strain $e_{[110]}$ can be directly compared to e_x for a stripe along [100] to determine the difference in perpendicular relaxation for both geometries. We note that in the rotated matrix E', the shear strain vanishes, as we would expect for a stripe aligned with the coordinate axes.

The strain simulation shown in Fig. 4.8 was compiled by varying the relative width of a (Ga,Mn)As stripe with identical parameters as discussed in Section 4.3.1.

By comparing the relaxation perpendicular to the stripe, $e_{[110]}$, with the the corresponding e_x (dotted blue line) of the nonrotated stripe, we can immediately see, that we achieve a lesser degree of relaxation in this geometry for otherwise identical structures. This fact is also evident in the larger value of e_z in the rotated stripe. The

in-plane strain relaxation is split equally between e_x and e_y, and therefore significantly different from the [100] case, where e_x represents the full in-plane relaxation and e_y remains at the pseudomorphic value. The shear strain e_{xy} is a new factor whose influence on the magnetic anisotropy will be investigated in Chapter 5. For large values of rw, the [1$\bar{1}$0] stripes also approach the limit of an unpatterned pseudomorphic layer, with $e_{xy} \to 0$.

Chapter 5

Local Anisotropy Control by Strain Engineering

As discussed in the previous chapter, finite element simulations of the strain relaxation in stripe-shaped nanostructures predict a significant anisotropy in strain for the directions parallel and perpendicular to a long stripe axis. Theoretical band structure calculations and the Zener model indicate that lattice strain plays a significant role in determination of the magnetic anisotropy of (Ga,Mn)As. To investigate the interplay between lattice strain and magnetic anisotropy, we have produced a series of samples. Their main characterizing properties, aside from Mn content and layer thicknesses, are twofold: the inclusion of a stressor layer and the alignment direction of the stripe pattern. Therefore the series contains samples

- consisting solely of a (Ga,Mn)As layer on a GaAs substrate.

- containing an additional (In,Ga)As stressor layer between the substrate and the (Ga,Mn)As layer to increase lattice strain.

- with stripe structures aligned along the [100] crystal direction.

- with stripes aligned along the [1$\bar{1}$0] direction.

In the first section of this chapter, we will describe the fabrication process of the samples and provide detailed XRD studies which investigate the strain situation in the parent and structured layers. The second section focuses on the magnetic characterization by SQUID and transport measurements.

At this point it is important to emphasize the difference between the two mechanisms of relaxation which are important in the context of this work. One is the relieving of accumulated growth strain during fabrication of an epitaxial layer. This effect takes place after a critical layer thickness is reached during growth of a layer with a lattice mismatch to its substrate. Stress relief is achieved via plastic relaxation of the crystal, through formation of lattice defects, which leads to degradation of the layer quality. During this process, the lattice constant will increase in both in-plane directions, which is why we will refer to this phenomenon as biaxial relaxation.

The strain relaxation discussed in this chapter is induced by the removal of constricting material in parts of the layer. The initial condition of the layer, which is below its critical thickness, is still completely pseudomorphic, with a crystal devoid of lattice
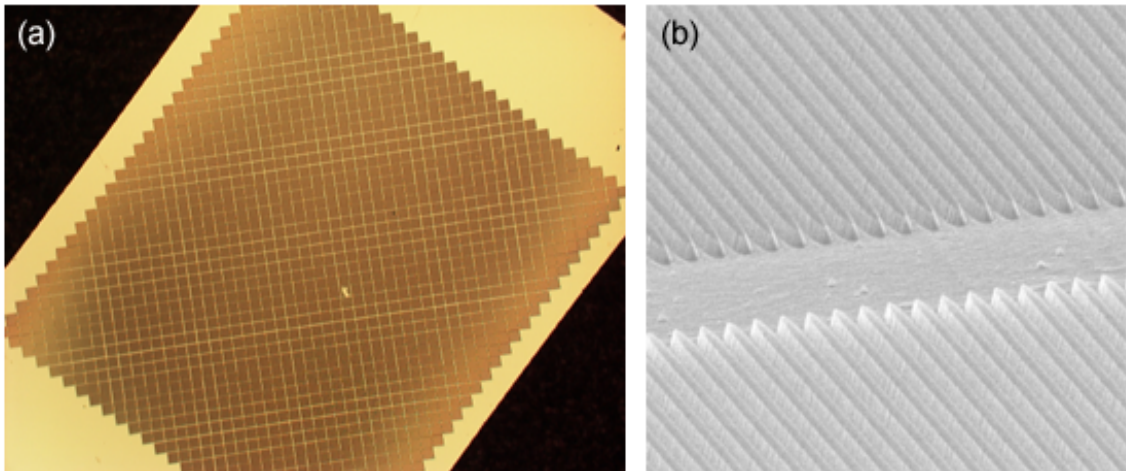
Figure 5.1: (a) microscope image of patterned 4 × 4 mm stripe array containing fields of 251 parallel stripes. (b) SEM image of border region between two stripe fields. The width of the stripes is 200 nm.

defects caused by plastic deformation. In pattering the layer into strips as introduced in the previous chapter, we allow the stripe material to relieve strain by expanding its lattice perpendicular to the stripe axis. This deformation is purely elastic and does not cause the formation of lattice defects. Since the lattice constant along the stripe direction is unaffected, we refer to this case as uniaxial relaxation.

5.1   Patterning and Structural Characterization

Table 5.1 provides a list of all samples which will be discussed in this chapter. All samples were grown following the general procedure described in Chapter 3. The (In,Ga)As stressor layer was grown at a temperature of 500 °C. For this layer, it is critical to avoid crossing the critical layer thickness and therefore the onset of plastic strain relaxation through lattice defect formation. The critical layer thickness can be estimated according to [Cohe 94]. Verification that indeed no relaxation takes place before pattering is achieved by HRXRD measurements.

After growth, electron beam lithography and chemically assisted ion beam etching are used to pattern the samples into the desired stripe structures. For most samples, a total area of 4 × 4 mm is covered by arrays of stripes, see Fig. 5.1. Each field in the array contains 251 parallel stripes, with each individual stripe measuring nominally 200 nm × 100 μm. The separating distance between the stripes is 200 nm. A total etch depth of about 200 nm was chosen to avoid influence from insufficient GaAs pillar height (see Section 4.3.2).

Table 5.1: List of (Ga,Mn)As stripe samples. Layer thickness and material content as determined by HRXRD measurements. All strains are simulation values in units of 10^{-3}, averaged over a cross section of the respective layer.

sample name	(Ga,Mn)As thickness	[Mn]	(In,Ga)As thickness	[In]	stripe alignment	(Ga,Mn)As strain e_x	e_y	e_z	e_{xy}	(In,Ga)As strain e_x	e_y	e_z	e_{xy}
A (S366)	70 nm	2.5%	–	–	[100]	0.21	-1.50	0.56	0.00	–	–	–	–
B (S336)	70 nm	2.5%	80 nm	7.4%	[100]	1.47	-1.50	-0.27	0.00	0.08	-5.30	1.58	0.00
C (S336)	70 nm	2.5%	80 nm	7.4%	[1$\bar{1}$0]	-0.42	-0.42	-0.06	1.09	-3.10	-3.10	3.55	2.16
D (S464)	19 nm	4.4%	11 nm	12.8%	[100]	1.87	-2.30	0.21	0.00	-5.31	-9.20	6.50	0.00
E (S464)	19 nm	4.4%	11 nm	12.8%	[1$\bar{1}$0]	-0.64	-0.64	0.60	1.65	-7.59	-7.59	6.83	1.59
F (S469)	19 nm	5.4%	14 nm	19.0%	[100]	3.60	-2.60	-0.44	0.00	-7.29	-13.60	9.36	0.00
G (S469)	19 nm	5.4%	14 nm	19.0%	[1$\bar{1}$0]	-0.15	-0.15	0.16	2.45	-11.10	-11.10	9.93	2.52
H (S470)	18 nm	4.4%	15 nm	22.6%	[100]	4.78	-2.30	-1.09	0.00	-8.81	-16.20	11.20	0.00
I (S470)	18 nm	4.4%	15 nm	22.6%	[1$\bar{1}$0]	0.47	0.47	-0.41	2.78	-13.20	-13.20	11.90	3.02

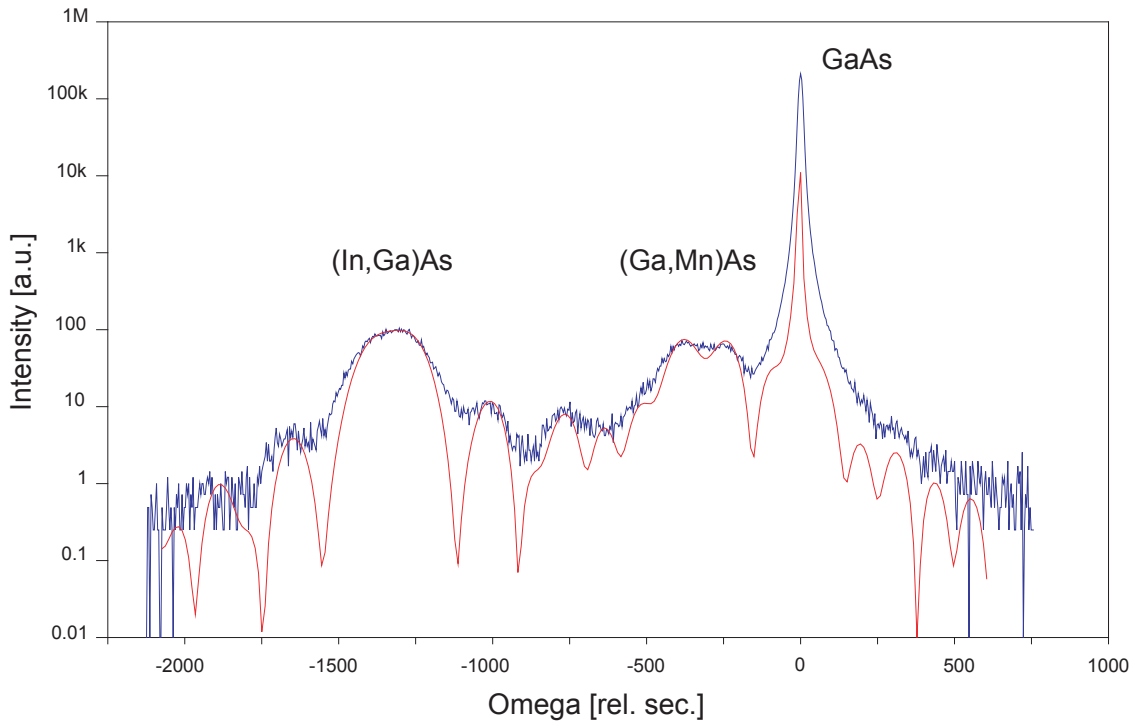**Figure 5.2:** HRXRD ω-2Θ-scan (blue line) of the (004) reflection of the unpatterned, as-grown wafer from which samples B and C were processed. The red line is a simulation of the scan with the sample parameters given in table 5.1. The substrate peak is located at $\omega = 32.086°$.

5.1.1   HRXRD Measurements

Parent Layer ω-2Θ-Scans

The parent layers were investigated with high resolution X-ray diffraction measurements of the (004) reflection to guarantee high layer quality and fully pseudomorphic layers. Fig. 5.2 shows an ω-2Θ-scan of an unpatterned piece of the parent layer for samples B and C. The good agreement between the scan and the simulation of a completely pseudomorphic structure with parameters as given for the samples in Table 5.1 proofs high layer quality and confirms that no significant relaxation has taken place during growth. Similar measurements have been performed for all samples discussed in this chapter.

HRXRD RSM, Relaxation Triangles

To quantify the strain relaxation after pattering the layer into the stripe structure, two different XRD techniques were used. We will first focus on the HRXRD RSM method as introduced in Section 3.5.2. The crucial difference to the situation discussed in Section 3.5.2, in which we showed measurements on a biaxially relaxed layer, is that stripe samples are subject to uniaxial and therefore anisotropic lattice relaxation in the plane of the sample.

To discuss how we model this uniaxial relaxation, i.e. how we construct the re-

laxation triangle for full relaxation, we have to distinguish between the two different stripe alignments. Stripes aligned along the [100] direction are easy to understand in the sense that we can imagine the relaxation as analogous to biaxial, with the suppression of relaxation in one in-plane direction, hence uniaxial. Due to this suppression, more growth strain is relieved by expanding the lattice in the remaining free directions. The in-plane lattice constant perpendicular to the stripes will therefore be larger (smaller $q_\parallel$ in the RSM) than we would observe for a biaxially relaxed layer. The same is true for the vertical lattice constant, which is also larger (smaller $q_\perp$) than for the case of biaxial relaxation.

We can calculate the strain limits for the free surfaces of the stripe by using Eqn. (4.18). Written in a form independent of crystal directions, it reads:

$$e_\perp = -\nu e_\parallel \tag{5.1}$$

This equation relates the compression of the lattice along the stripe ($e_\parallel$) with the resulting transverse strain ($e_\perp$) via the Poisson ratio ν. Using the definition of strains as the relative lattice constant difference between the strained and the relaxed condition (see Eqn. (2.2)), we can write:

$$e_\perp = \frac{a_{uniax} - a_{relaxed}}{a_{relaxed}}; \qquad e_\parallel = \frac{a_{substrate} - a_{relaxed}}{a_{relaxed}} \tag{5.2}$$

Here, we use a_{uniax} to designate the relaxed lattice constant for the case of uniaxial relaxation, while $a_{relaxed}$ refers to the relaxed lattice constant of bulk (Ga,Mn)As. Substituting these two relations into Eqn. (5.1), we can solve for a_{uniax}:

$$a_{uniax} = -\nu(a_{substrate} - a_{relaxed}) + a_{relaxed} \tag{5.3}$$

The crystal structure of the relaxed stripe has a tetragonal symmetry, with a_{uniax} in the perpendicular directions, and $a_{substrate}$ in the direction parallel to the stripe.

For the case of a stripe aligned along the [1$\bar{1}$0] direction, the situation is slightly more complicated. The Poisson ratio ν is usually defined for stresses and resulting strains in $\langle 100 \rangle$ directions, which is the case for biaxially relaxing layers and [100] stripes. In this case the value for ν is defined by the elastic compliances:

$$\nu = -\frac{s_{12}}{s_{11}} \tag{5.4}$$

While this definition has been correct for all situations described so far, we now encounter stress along [1$\bar{1}$0], with resulting strains in [110] and [001]. An expression for ν for arbitrary orientations of the cubic crystal has been described by [Bran 73] for a longitudinal stress along a direction **l** which causes a strain in an orthogonal direction **m**:

$$\nu = -\frac{s_{12} + (s_{11} - s_{12} - \frac{1}{2}s_{44})(l_1^2 m_1^2 + l_2^2 m_2^2 + l_3^2 m_3^2)}{s_{11} - 2(s_{11} - s_{12} - \frac{1}{2}s_{44})(l_1^2 l_2^2 + l_2^2 l_3^2 + l_1^2 l_3^2)} \tag{5.5}$$

The s_{ij} are the three independent elastic compliances. The l_i and m_i are the direction cosines of **l** and **m** with respect to the $\langle 100 \rangle$ cubic axes. With this equation, we calculate for

$$\mathbf{l} = [100], \quad \mathbf{m} = [010]: \qquad \nu = 0.312$$
$$\mathbf{l} = [100], \quad \mathbf{m} = [001]: \qquad \nu = 0.312$$

$$\mathbf{l} = [1\bar{1}0], \quad \mathbf{m} = [110]: \qquad \nu_1 = 0.021$$
$$\mathbf{l} = [1\bar{1}0], \quad \mathbf{m} = [001]: \qquad \nu_2 = 0.444$$

Comparing ν and ν_1, we can immediately see that the crystal is much less susceptible to deformations in [110] than in [010] direction, when they are caused by stress in an orthogonal direction. Contrary to that, the stress in the vertical direction is larger as compared to the [100] stripes. These results confirm the simulation data, which also predict reduced lattice relaxation perpendicular to the stripes but an increased value in the vertical direction, when comparing [1$\bar{1}$0] and [100] stripes. Using Eqn. (5.3), we obtain for the relaxed lattice constants:

$$a_{uniax,[110]} = -\nu_1\big(a_{substrate} - a_{relaxed}\big) + a_{relaxed}$$
$$a_{uniax,[001]} = -\nu_2\big(a_{substrate} - a_{relaxed}\big) + a_{relaxed}$$

During relaxation, the base of the unit cell is extended along the [110] diagonal, while remaining fixed along the other diagonal, thus forming a parallelogram. The resulting crystal symmetry is therefore monoclinic.

Neither the substrate position nor the pseudomorphic position is different for the uniaxial relaxation triangles. With these considerations, we are now able to calculate the entire relaxation triangle for both stripe alignments. The relaxed position coordinates are summarized in Tbl. 5.2. Fig. 5.3 shows the uniaxial and for reference the biaxial relaxation triangle for both stripe alignments.

Table 5.2: Reciprocal space coordinates for the relaxed position of the relaxation triangle for a biaxially relaxed layer and two different alignment of uniaxially relaxed stripes.

relaxed position for	$(q_\parallel, q_\perp)$
biaxially relaxed layer	$\left(h \cdot \frac{a_{sub}}{a_{relaxed}}, l \cdot \frac{a_{sub}}{a_{relaxed}}\right)$
[100] stripe	$\left(h \cdot \frac{a_{sub}}{a_{uniax}}, l \cdot \frac{a_{sub}}{a_{uniax}}\right)$
[1$\bar{1}$0] stripe	$\left(h \cdot \frac{a_{sub}}{a_{uniax,[110]}}, l \cdot \frac{a_{sub}}{a_{uniax,[001]}}\right)$

HRXRD RSM, [100] Stripes

To investigate the strain relaxation in [100] stripes, we measure two reciprocal space maps of sample B, one of the (026) reflection, with the incident x-ray beam along the [010] direction, and one map of the (206) reflection, with incident x-rays along the [100] direction. In the first case, only lattice planes with [010] and [001] components will contribute to the scattering process, or, in other words, the measured $q_\parallel$ corresponds to an $a_\parallel = a_{[010]}$. In the second case, the incident x-ray beam is rotated by 90° in the plane of the sample relative to the first case. The lattice constant $a_\parallel$ measured in this RSM therefore corresponds to $a_{[100]}$. The vertical component remains identical
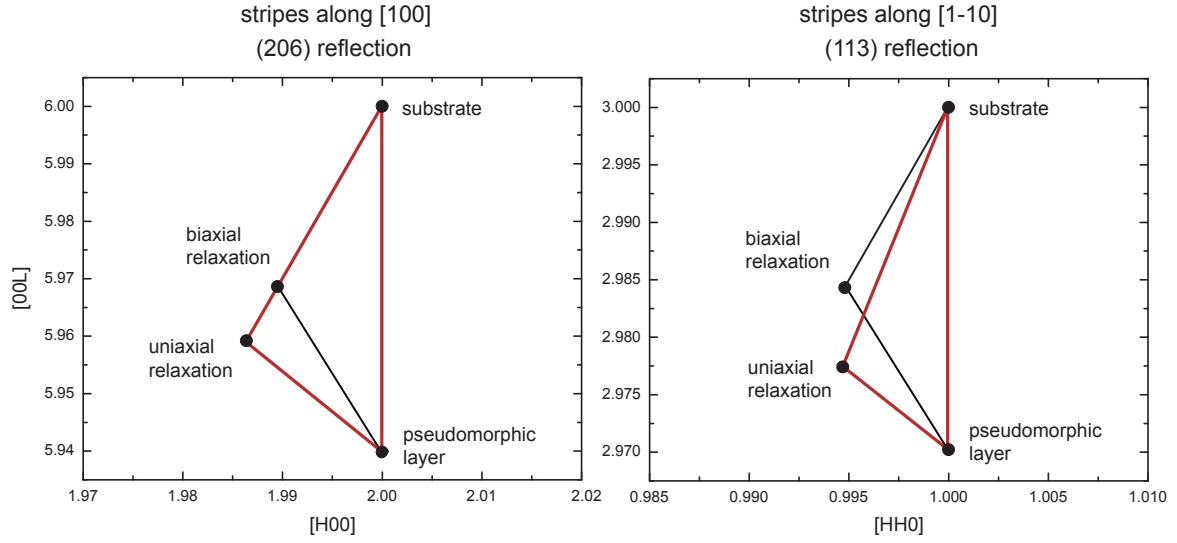
Figure 5.3: Red lines: relaxation triangles for the uniaxial relaxation of two differently aligned stripes. The according relaxation triangle for biaxial relaxation is marked in black. The coordinates for all corner points are given in Tbl. 3.1 and Tbl. 5.2. The displayed triangles are calculated for the (In,Ga)As layer of samples B and C.

for both maps and measures the vertical lattice constant $a_{[001]}$. By analyzing the two RSMs, shown in Fig. 5.4, we can independently determine the lattice constant and therefore the strain perpendicular and parallel to the patterned stripe axis.

In Fig. 5.4 (a), we observe a shift of the (In,Ga)As peak along the relaxation line, which is caused by the relaxation of the lattice in [010] direction, perpendicular to the stripes. The (In,Ga)As peak in Fig. 5.4 (b) on the other hand is shifted along the surface normal towards larger $q_\perp$. This indicates a smaller lattice constant in [001], which is explained by the fact that the lattice relaxes perpendicular to the stripe, thus lowering the lattice parameter in z-direction due to the Poisson effect. The fact that no shift in $q_\parallel$ is observed in this map proves, that no relaxation takes place along the stripe axis. To calculate the degree of relaxation for the (In,Ga)As stressor layer in Fig. 5.4 (a), with its peak position at (1.9898, 5.9552), we rewrite Eqn. (3.9) by replacing a_{rel} with a_{uniax}:

$$\gamma = \frac{a_\parallel - a_{sub}}{a_{uniax} - a_{sub}}. \tag{5.6}$$

With this equation we determine a value of $\gamma = 0.75$.

The peak of the (Ga,Mn)As layer is difficult to resolve in these maps. Even in the pseudomorphic sample (see ω-2Θ scan in Fig. 5.2), the separation between this layer peak and the substrate peak is small. We expect that the relaxation of the underlying (In,Ga)As stressor layer during pattering forces a corresponding lattice constant, and therefore $q_\parallel$ position, on the (Ga,Mn)As layer. The [010] (Ga,Mn)As lattice constant is thus increased, which leads to a reduction in the vertical lattice constant of the stripes. This shifts the peak accordingly to larger values of $q_\perp$ and causes it to be partially overlapped by the substrate peak. The measurement is further complicated by the relatively small volume of the stripe structure compared to a complete layer, which leads to a low intensity of the scattered x-rays. With regard to these effects,
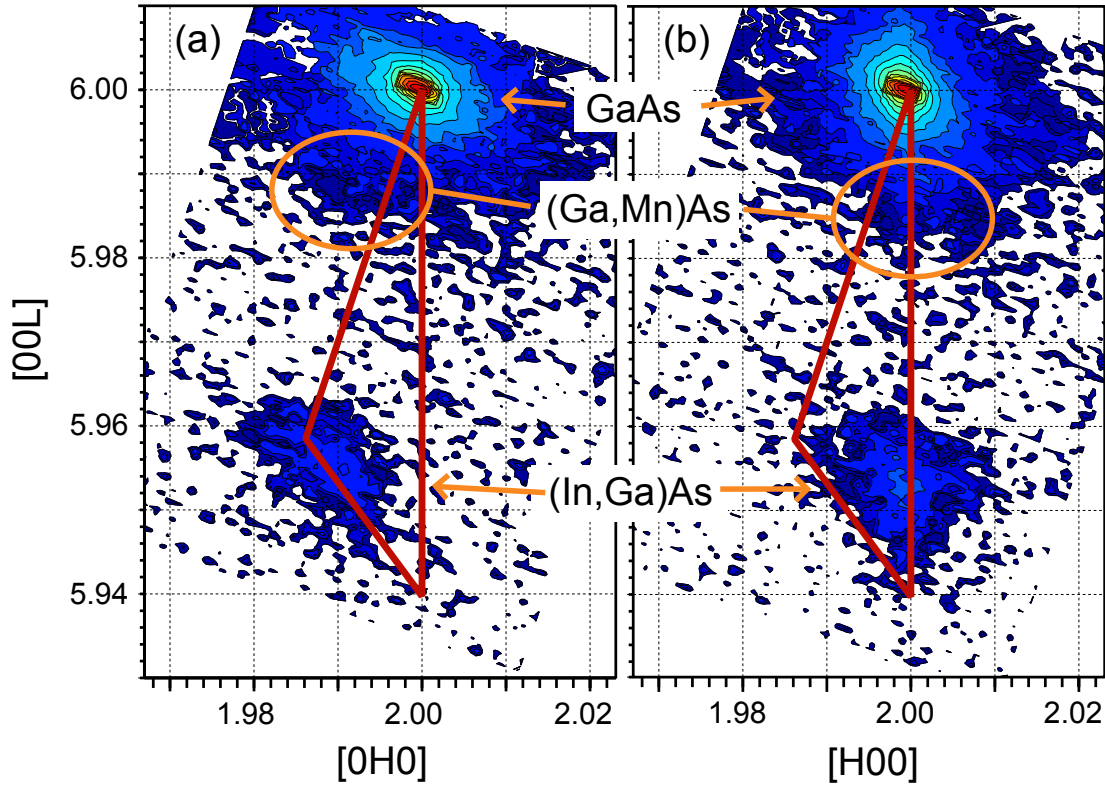
Figure 5.4: HRXRD measurement of sample B, showing a reciprocal space map of the (026) and (206) Bragg reflection with incident x-rays (a) perpendicular and (b) parallel to the stripe axis. The red line indicates the triangle of relaxation for (In,Ga)As for uniaxial relaxation.

we attribute the bulge marked with orange ovals below the substrate peak in Fig. 5.4 (a) and (b) to the (Ga,Mn)As layer. By estimating its peak position in the RSM in Fig. 5.4 (a) at (1.992, 5.988), we conclude, that tensile strain in the range of $e_{[010]} = (2.2 \pm 1.0) \times 10^{-3}$ has been induced in the (Ga,Mn)As layer by the underlying stressor. This value is in good agreement with the finite element simulations which predict a value $e_{[010]} = 1.47 \times 10^{-3}$ for this sample.

HRXRD RSM, $[1\bar{1}0]$ Stripes

For $[1\bar{1}0]$-aligned stripes, the situation is slightly different than in the previous measurement. Lattice planes of asymmetric reflexes with $h = k$ are now oriented along the direction parallel and perpendicular to the stripe axis. For this reason we chose the (113) Bragg reflection for the measurement of sample C shown in Fig. 5.5. Both maps are qualitatively very similar to the maps measured for [100] stripes. For incident x-rays perpendicular to the stripes (Fig. 5.5 (a)), we observe a shift of the stressor layer peak along the relaxation line, caused by lattice expansion in [110] direction. For x-rays parallel to the stripes, no change in $q_{\parallel}$ is visible, which proves that the lattice of both top layers remains pseudomorphic to the substrate in this direction, as it did in the corresponding case for the [100] stripes.

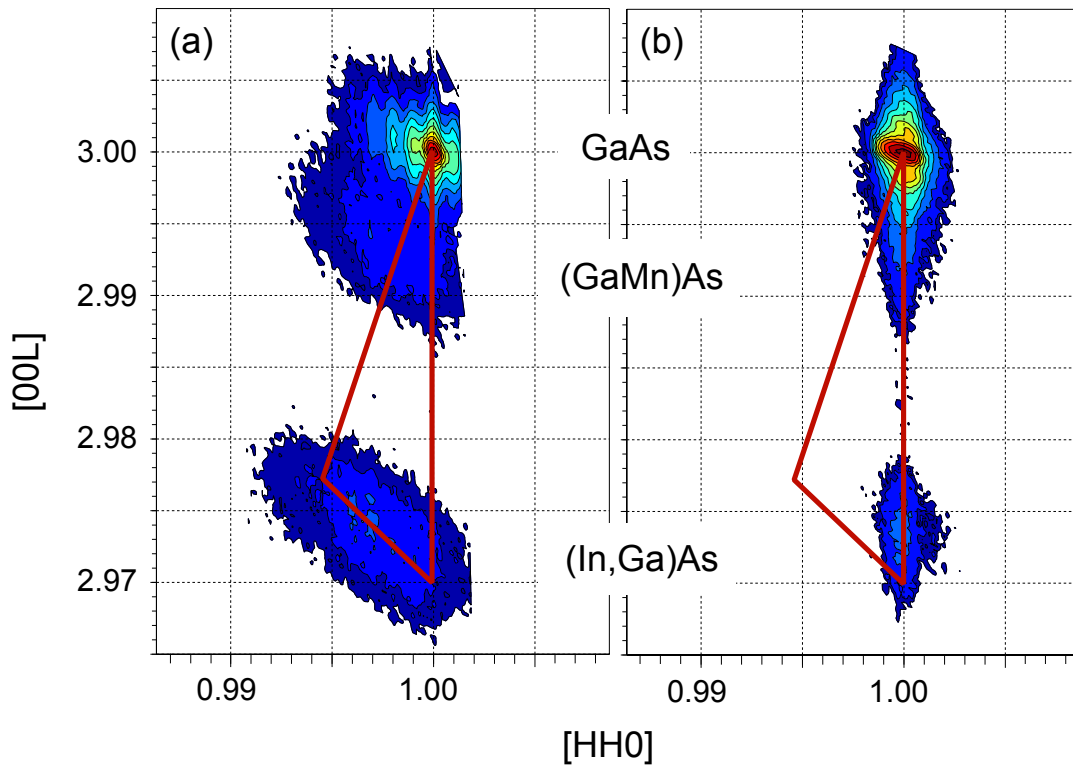As predicted by the finite element simulations, the overall strain relaxation is

Figure 5.5: HRXRD RSM around the (113) reflection of sample C. The incident x-rays are oriented (a) perpendicular and (b) parallel to the stripe direction along [1$\bar{1}$0]. The solid red line represents the relaxation triangle for the (In,Ga)As stressor layer.

smaller for [1$\bar{1}$0] stripes than for [100] stripes. By analyzing the layer peak positions, we find, that the induced strain in the (Ga,Mn)As layer is $e_{[100]} = e_{[010]} = 0.3 \pm 1.0 \times 10^{-3}$ (Simulation: $e_{[100]} = e_{[010]} = -0.42 \times 10^{-3}$). From the location of the (In,Ga)As peak at $(0.9973, 2.9734)$, we calculate the degree of relaxation for the stressor layer as $\gamma = 0.48$.

An interesting feature is the modulation of the intensity of the substrate and, to a lesser degree, the layer peaks in Fig. 5.5 (a). The period of this modulation is approximately $q_{\parallel} = 0.0014$ r.l.u. In real space units, this corresponds to a period of ≈ 400 nm, which identifies the modulation as superlattice reflections of the stripe array.

5.1.2 GIXRD RSM

Sample A has been selected for high-precision XRD measurements at beamline BW2 at the Hamburger Synchrotronstrahlungslabor (HASYLAB) to study the relaxation in a sample without stressor layer. For this type of sample, the XRD equipment available at Würzburg is insufficient to achieve quantitative data. With the high intensity of the synchrotron radiation provided at HASYLAB, it is possible to achieve a very high resolution. Measurements were performed in the grazing incidence (GI) geometry on the (333) reflection, with an incidence angle of $\alpha_i = 0.2°$ and a photon energy of 9.6 keV. The incidence angle is below the critical angle for total reflection in GaAs of

$\alpha_c = 0.256°$. This ensures, that scattering from the uppermost regions of the stripes is dominant and further increases the sensitivity in the region of interest.

Because of the small lattice mismatch between GaAs and (Ga,Mn)As in this sample of only $f = 1.5 \times 10^{-3}$, the Bragg reflections of both materials lie very close to each other. If the (Ga,Mn)As stripes were purely pseudomorphically strained, the difference between the two reflections would be only $\Delta l = 0.0044$ r.l.u., a value which can hardly be resolved with our experimental setup. However, since the height of the stripes is only about 70 nm, the (Ga,Mn)As (333) reflection is significantly broadened in l direction and fringes due to finite thickness are visible. Therefore, by mapping the reciprocal space on the maximum of one of the finite thickness fringes, which is far enough from the l position of the GaAs bulk peak, one is mainly sensitive to the (Ga,Mn)As stripes.

This measurement, a h-k map at $l = 2.98$, is shown in Fig. 5.6 (a), and a similar map through the GaAs (333) bulk peak in Fig. 5.6 (b). In the stripes sensitive measurement, one can clearly observe a shift of the peak towards smaller values in k. This shift indicates relaxation of the (Ga,Mn)As structure in [010] direction, whereas no relaxation takes place in [100] direction (no peak shift visible in h direction). The different widths of the peaks in h and k direction are due to the different lateral dimensions of the stripes.

In order to quantify the shift, we fit the measured peaks to Voigt profiles. Fig. 5.6 (c) shows the central k-line scan through the peaks of both reciprocal space maps (open circles in the figure). Each curve is fit with the sum of two Voigt profiles (thick solid lines), one fixed at $h = 3$ representing the bulk contribution, the other with a variable position. All four individual peaks are also shown as thin lines. By this procedure, we obtain a value for the strain perpendicular to the stripes of $e_{[010]} = -0.28 \times 10^{-3}$, which is very close to full relaxation ($e = 0$). Again, this result is in good agreement with simulation data, which predict a value of $e_{[010]} = 0.21 \times 10^{-3}$. For reference, the fully pseudomorphic condition before relaxation is $e_{[010]} = -1.50 \times 10^{-3}$.

Summary

The strain situation which we expect based on simulation results are confirmed by the various XRD measurements for all samples. Before patterning, all samples are completely pseudomorphic to the substrate and under in-plane biaxial compressive strain. Patterning the sample into the stripe arrays allows uniaxial lattice relaxation perpendicular to the long axis of the stripe. The direction along the stripe axis shows no sign of strain relaxation. The ability of the (In,Ga)As stressor layer to induce additional strain in the top (Ga,Mn)As layer could also be verified. For the presented measurements, the inclusion of a stressor layer increases the strain from $e_{[010]} = -0.28 \times 10^{-3}$ in sample A to $e_{[010]} = 2.20 \times 10^{-3}$ in sample B. Regarding the alignment of stripes, we found that relaxation is less for stripes oriented along the [1$\bar{1}$0] direction than for stripes along [100]. Finally, it has been shown that the finite element simulations are in good agreement with real structures.
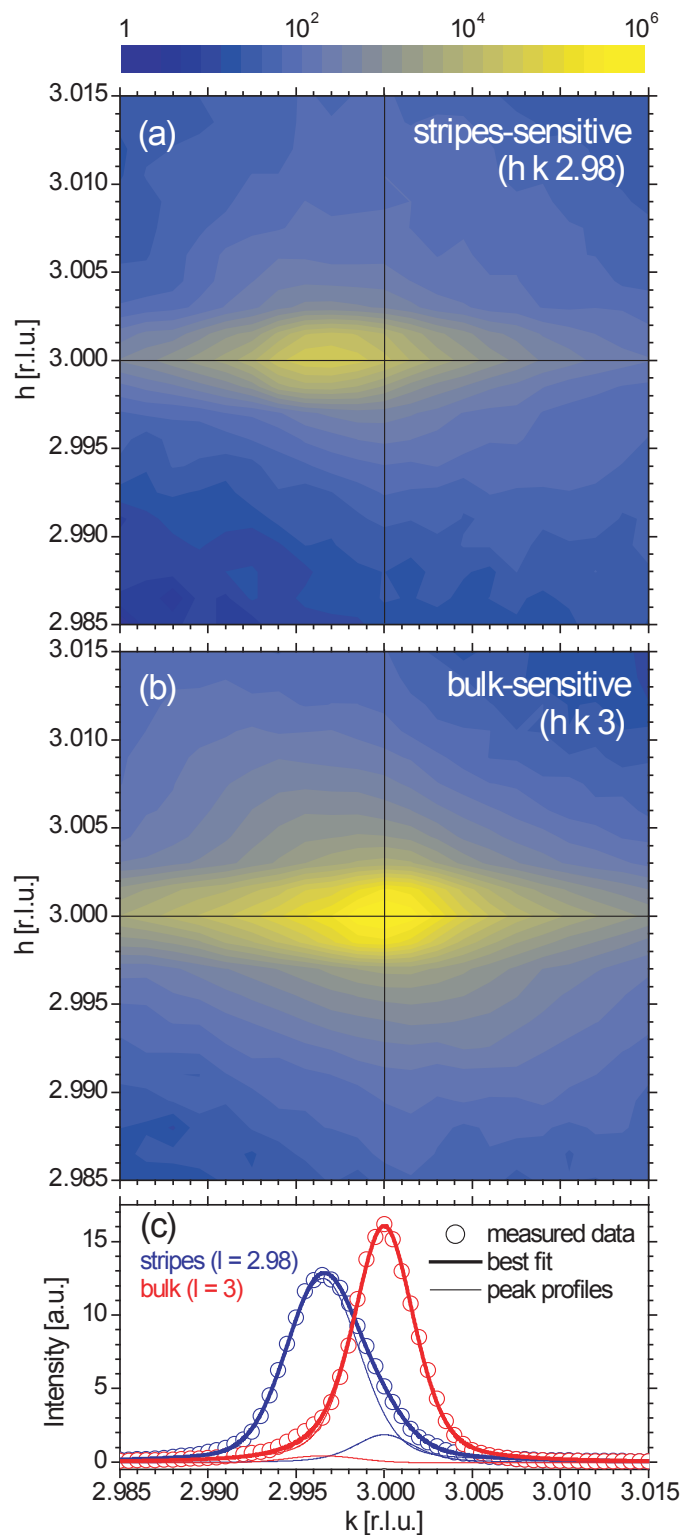
Figure 5.6: GIXRD reciprocal space *h-k* maps for sample A in the vicinity of the (333) Bragg reflection at (a) a stripes-sensitive and (b) a bulk-sensitive *l* position. In (c) the corresponding *k*-line scans (horizontal scans through the maximum of (a) and (b)) and best fitting Voigt profiles are shown.
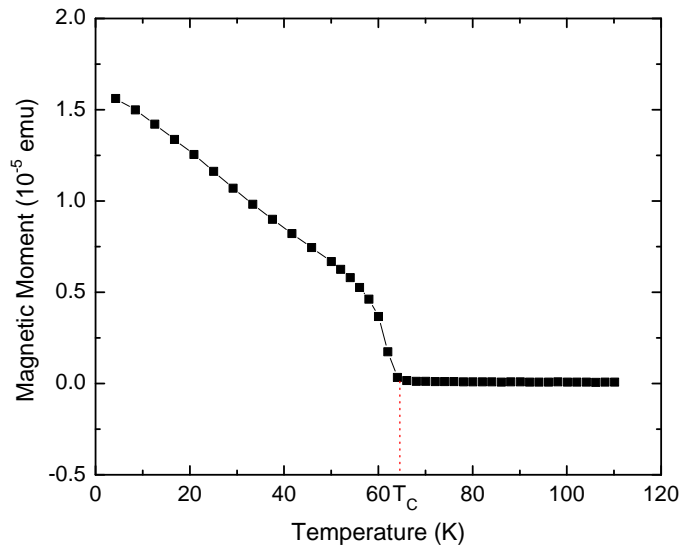
Figure 5.7: $M(T)$ SQUID curve of the parent layer of sample A. The red line indicates the ferromagnetism to paramagnetism phase transition at $T_C \approx 64$ K.

5.2 Magnetic Characterization

For investigation of the magnetic properties, especially the magnetic anisotropy, of the patterned samples and their parent layers, we use two characterization techniques. The first is a superconducting quantum interference device (SQUID), which allows us to measure hysteresis loops along selected crystal directions. The second are transport measurements in the presence of an external magnetic field, which make use of the anisotropic magnetoresistance (AMR) effect in (Ga,Mn)As, as described in Section 2.3.1. Both techniques and results will be discussed in detail in this section.

5.2.1 SQUID Measurements

The SQUID provides the possibility of a highly accurate measurement of the magnetic moment of the sample. It consists of a system of superconducting detection coils which are connected to the SQUID sensor with superconducting wires. A measurement is performed by moving a sample through the detection coils, which will cause an electrical induction current in the coils. Because the detection coils, the connecting wires and the SQUID input coil form a closed superconducting loop, any change in magnetic flux in the detection coil produces a proportional change in the persistent current in the detection circuit. Essentially, the SQUID functions as a highly linear current-to-voltage converter which transforms variations in the current in the detection coils to an output voltage which is proportional to the magnetic moment of the sample. In all data presented in this work, the background signals originating from the substrate and sample holder have been subtracted.

We use the SQUID for two types of measurements, namely $M(T)$ and $M(H)$, which are both very distinct for ferromagnetic materials. Fig. 5.7 shows a typical $M(T)$ curve of the parent layer of sample A. The magnetic moment decreases with increasing temperature up to the Curie temperature T_C, at which long range magnetic
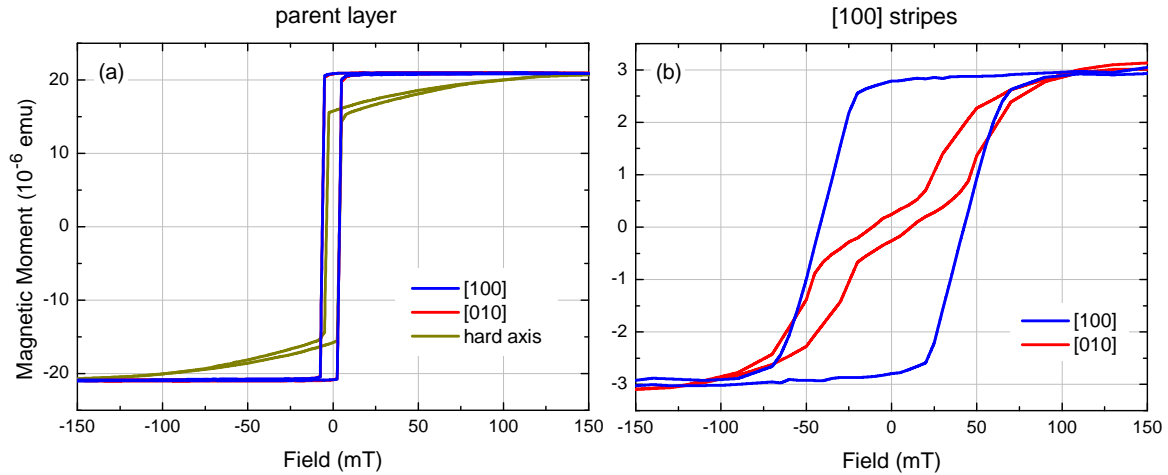
Figure 5.8: SQUID magnetization measurements for (a) the as-grown parent layer of sample A and (b) sample A with stripes along [100]. All measurements were performed at 4 K.

order is lost and the phase transition to Curie-Weiss paramagnetism takes place. The value of $T_C \approx 64$ K, which we obtain for this sample is typical for as-grown, unannealed (Ga,Mn)As layers.

Fig. 5.8 shows the magnetization M vs. H dependence of sample A as well as its parent layer. The external magnetic field of up to ± 150 mT is applied in all for major in-plane orientations. In the unpatterned layer (left panel), we observe the typical hysteresis loops for as-grown (Ga,Mn)As measured at a temperature of 4 K. The easy axes along [100] and [010] are located on top of each other and are difficult to distinguish on this scale. The hard axis magnetization value at zero field is roughly a factor of $\sqrt{2}$ smaller than the corresponding easy axis value. In this case we measure the projection of the magnetization (which is aligned along [100] or [010]) on the scan axis.

The behavior observed for the patterned sample, with stripes aligned along [100], shown in the right panel of Fig. 5.8, is heavily modified compared to the unpatterned case. The direction parallel to the stripe orientation is still a magnetic easy axis, similar to that of the host, albeit showing a much larger coercive field of 43 mT compared to the original 4 mT. In contrast to that, along the [010] direction, the easy axis is replaced by a pronounced hard axis behavior, marked by the drop of the remanent magnetization at zero field to $\sim 10\%$ of the parent layer value. We conclude from this measurement, that the biaxial easy axis in the parent layer has been replaced by a single uniaxial easy axis along the direction of the stripes after patterning.

The submicron dimensions of the lithographic patterning have also allowed us to reach the single domain limit in the (Ga,Mn)As stripes at low temperatures. We derive this conclusion from the observation, that the magnetization reversal along the remaining [100] easy axis takes place at circa the uniaxial anisotropy field $H_a = 45$ mT, which we obtain from transport measurements as detailed in the following section. This indicates a nearly fully coherent Stoner-Wohlfarth rotation behavior of the magnetization in the stripe as opposed to domain wall nucleation and propagation in the parent layer.

When comparing the saturation magnetization in Fig. 5.8 (a) and (b), we note a

reduction of a factor of 7 from the parent layer to the stripe sample. The main reason for this difference is that both measurements were done on different pieces of the same wafer which were not of exactly equal size. We estimate that the total (Ga,Mn)As volume in the patterned sample is approximately by a factor of 5 smaller than in the as-grown sample piece. This estimate takes into account the difference in sample size, area between the stripe fields and damage caused by etching. The remaining disparity in saturation moment can be explained considering the uncertainty in determining the volume and possible local fluctuations of Mn content (two different pieces of one wafer). Sidewall damage due to etching is also a possible, albeit probably small, contribution to this effect.

5.2.2   Transport Measurements

[100] Stripes

For the transport measurements, a field of 251 parallel stripes is contacted from both ends. The current direction $\mathbf{J}$ is therefore parallel to the stripes. At 4 K, a series of magnetic field sweeps from -300 mT to 300 mT is performed. Between each scan, the angle ϕ between the magnetic field $\mathbf{B}$ and the current $\mathbf{J}$ is increased by an increment until the whole range from $0°$ (parallel to the stripes) to $90°$ (perpendicular to the stripes) is covered. A selection of transport measurements is shown in Fig. 5.9 for the samples A, B and F from Tbl. 5.1.

In all measurements, the initial configuration is the $\mathbf{B} \parallel \mathbf{J}$ or $\phi = 0°$ setup. For a magnetic field sweep along this direction, we observe a low resistance state over the whole sweep range for all three samples in Fig. 5.9. According to Sec. 2.3.1, a low resistance is expected in (Ga,Mn)As, when the magnetization $\mathbf{M}$ is aligned parallel to $\mathbf{J}$. With progressively increasing ϕ, we note an increase in magnetoresistance at higher fields up to an angle dependent saturation value. This increase in resistance reaches a maximum for $\phi = 90°$, which corresponds to an orientation perpendicular to the stripe direction. Since a high magnetoresistance in (Ga,Mn)As is expected for $\mathbf{M} \perp \mathbf{J}$, we explain our observations as follows: In the absence of an external field $\mathbf{B}$, the magnetization $\mathbf{M}$ is oriented along the direction of the stripes. Sweeping the field in this direction does not change the orientation $\mathbf{M}$ (save for the $180°$ reversal marked by the change in the slope of the curve) and has therefore no influence on the magnetoresistance. Applying $\mathbf{B}$ under an angle to the stripe direction forces $\mathbf{M}$ away from this direction at higher fields. The resulting angle between $\mathbf{M}$ and $\mathbf{J}$ leads to an increase in the resistance. The maximum is reached when $\phi = 90°$, in which case the magnetization is forced to orient perpendicular to the current. The fact that all curves share a low resistance state at zero external field proves the existence of a uniaxial easy axis along the stripe direction.

The opening of the curves is a measure for the strength of the uniaxial anisotropy. If only a pure uniaxial anisotropy was present, the hard axis magnetoresistance scan would be parabolic and the magnetic field necessary to force the magnetization perpendicular to the easy axis would be a direct measure for the strength of the anisotropy. The presence of a small biaxial anisotropy contribution is evident in a slight shift of the parabola to positive fields. An estimate of the uniaxial anisotropy field H_a (see Sec. 2.3) is achieved by the following procedure [Huem 07]. We fit a parabola to the low field part of the $\phi = 90°$ curve [West 60]. The intersection of this parabola with
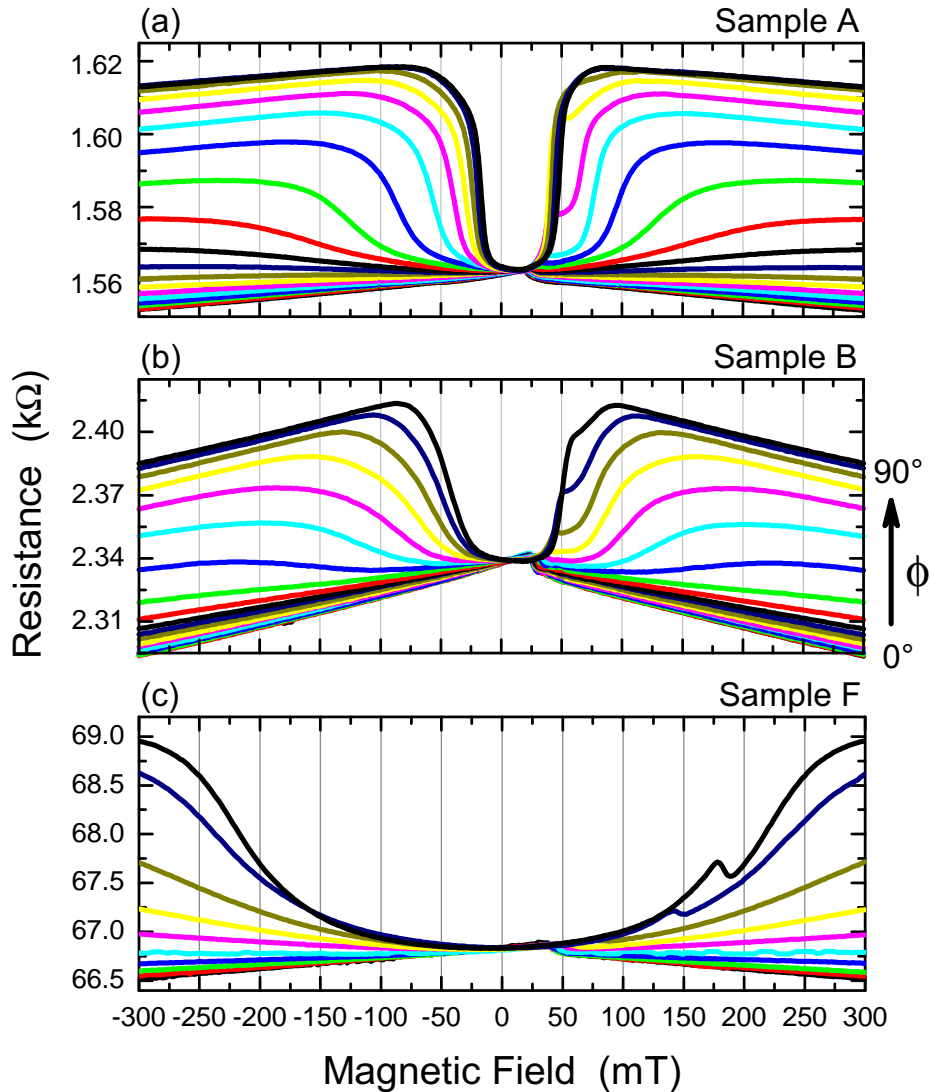
Figure 5.9: Magnetoresistance scans on stripe samples A, B and F at 4 K. The lowest curve in each plot corresponds to $\phi = 0°$, the highest curve to $\phi = 90°$, as indicated in (b). All curves are hysteretically symmetrical.

the linear extrapolation of the saturation value at high fields gives the value for H_a.

Using this method, we find a value of $H_a = 45$ mT for sample A and $H_a = 80$ mT for sample B. For the higher strained samples (D, F, H) we cannot apply this method due to technical limitations of the measurement setup. It is only possible to apply magnetic fields up to ±300 mT, which is insufficient to achieve full saturation in these samples (see Fig. 5.9 (c)). We will therefore use the width of the parabolic opening at half height as a figure of merit when comparing the strength between differently strained samples. For geometrical reasons, the width at half height is roughly $\sqrt{2}/2$ of H_a.

In Fig. 5.10, we compile the results on all transport measurements of [100]-aligned stripes. We observe an increase of the width of the openings, and therefore the
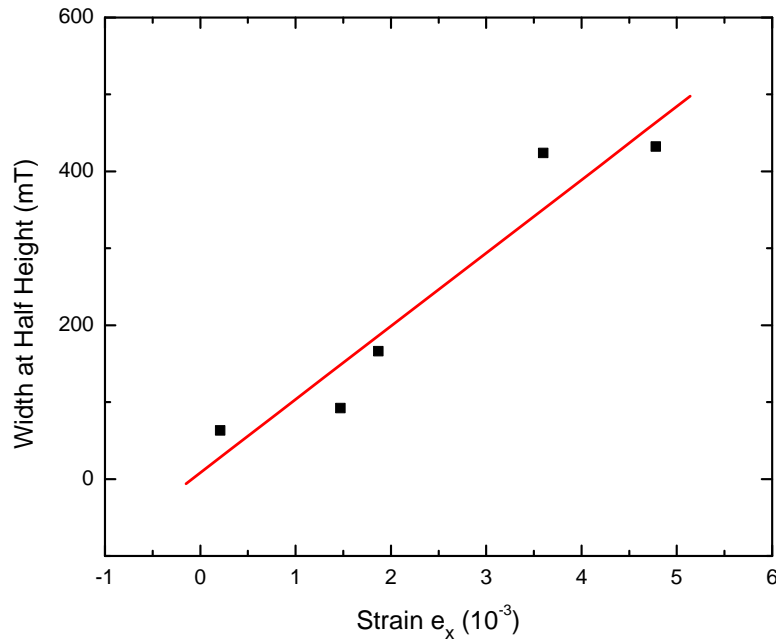
Figure 5.10: Width of the opening at half height of the parabolic low field part of the magnetoresistance scans over average strain in x-direction. All samples of Tbl. 5.1 with [100]-aligned stripes are shown. The red line is a linear interpolation.

anisotropy field, with increasing average strain. There are several factors which explain the scattering of the data points around the red linear interpolation line. As mentioned in the previous chapter, all simulations from which the strain value is calculated consider ideal stripes. This means that inhomogeneous etching, which may cause rough or slanted sidewalls and therefore regions of inhomogeneous strain are not taken into account. Also, the physical dimensions (stripe width, etch depth) are expected to differ slightly between simulation and processed stripes, causing another uncertainty in the strain value. Furthermore we will show in annealing experiments detailed in the following section, that the carrier density has an impact on the strength of the anisotropy. Since the Mn content of the stripe samples in Fig. 5.10 varies between 2.5–5.4%, differences in carrier concentration are also accountable for the scattering of the data points. But, even taking all aforementioned uncertainties into account, we still observe a very clear dependence of the anisotropy field on the lattice strain, which identifies it as the driving force in determining the configuration of the magnetic anisotropy in (Ga,Mn)As nanostructures.

[1$\bar{1}$0] Stripes

The situation for [1$\bar{1}$0] oriented stripes is notably different from what we observe for the [100] stripes. Fig. 5.11 (a) shows magnetotransport measurements on sample I. As with the [100] stripes, the external field sweeps are performed in the interval from **B** $\parallel$ **J** ($\phi = 0°$) to **B** $\perp$ **J** ($\phi = 90°$). In contrast to the [100] stripe measurements in Fig. 5.9, the lowest curve at $\phi = 0°$ is not the flattest curve of the ensemble. The curvature of a magnetotransport measurement is caused by the rotation of the magnetization to the
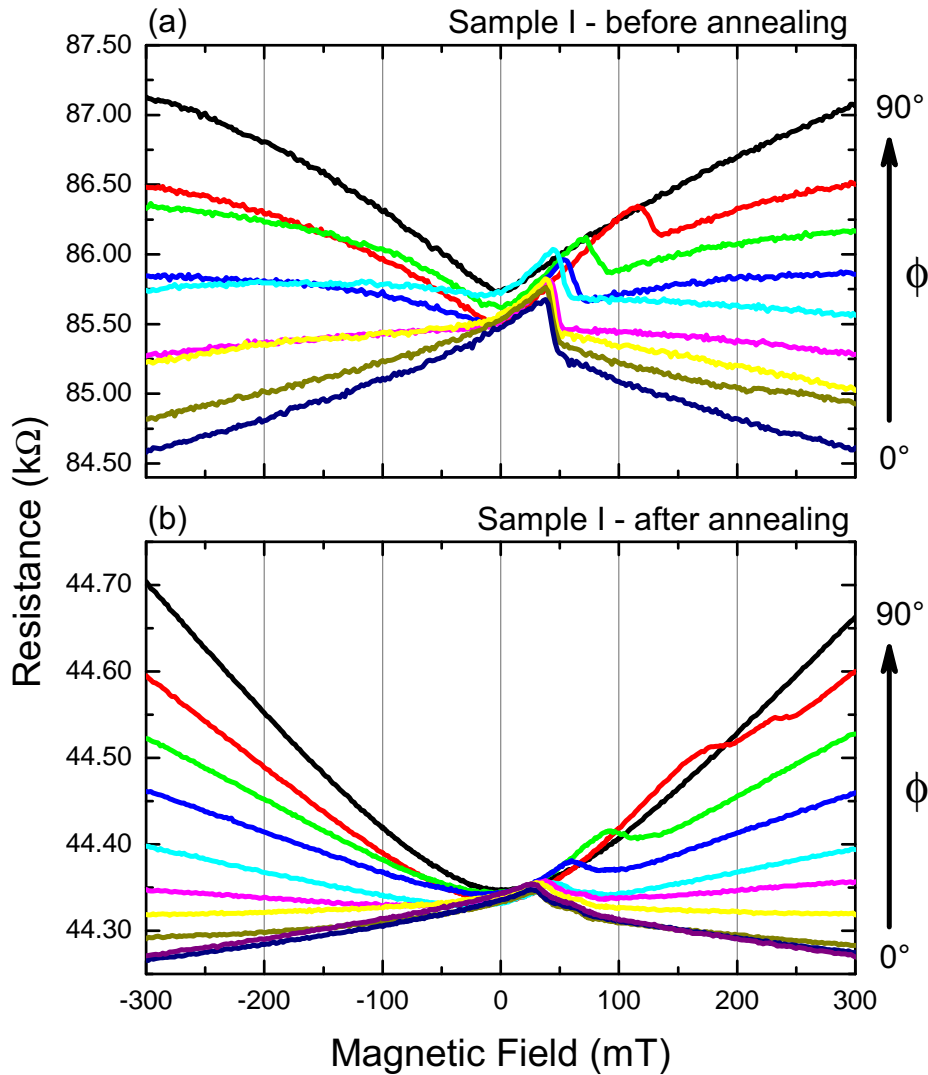
Figure 5.11: Magnetoresistance scans on stripe sample I (a) before and (b) after annealing for 50 hours. Although the applied magnetic field is insufficient to achieve saturation for high ϕ, a reorientation of the easy axis between the two plots is observable.

nearest easy axis. Therefore, we do not observe purely uniaxial behavior parallel to the stripe direction as in the [100] stripes. The curvature of the lowest curves indicates that the magnetization rotates away from the stripe direction in the absence of an external field. The easy axis of sample I is therefore located at some angle between the original easy axis (45° to the stripe axis) and the stripe direction.

To quantify this reorientation, we have to determine the exact angle ϑ_x of the easy axis after patterning of the $[1\bar{1}0]$ stripes, which can be evaluated directly from the magnetotransport measurements [Deng 08a]. To do so, we have to subtract the isotropic component of the magnetoresistance from the 0° and 90° curve. The isotropic component is determined by fitting the linear region of the measurement curve with the smallest slope, as shown in Fig. 5.12. This fit line is matched to the linear region of the 0° and 90° curve by parallel translation. The intersection of these three lines with $H = 0$ mT defines two resistance values, which we call Δ_1 and Δ_2.
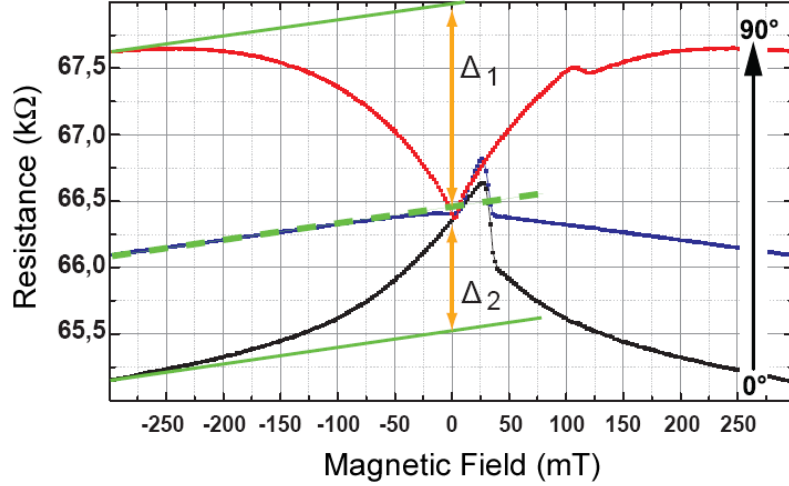
Figure 5.12: Determination of the isotropic component by linear fit of the curve with smallest slope (blue). Parallel translation to 0° (black) and 90° (red) curve defines Δ_1 and Δ_2 by intersection with $H = 0$ mT.

Using these values, we can rewrite the formula for the longitudinal resistivity of the AMR effect, Eqn. (2.13), as

$$\rho_{xx} = \rho_\perp - \Delta\rho \; \cos^2(\vartheta), \tag{5.7}$$

with

$$\Delta\rho = (\rho_\perp - \rho_\parallel) = (\Delta_1 + \Delta_2). \tag{5.8}$$

At $H = 0$ mT, we can write the resistance change Δ_2 caused by the angle ϑ_x between **M** and **J** as

$$\Delta_2 = \rho_{xx}(\vartheta_x) - \rho_{xx}(\vartheta = 0°). \tag{5.9}$$

Combining (5.7) and (5.9) leads to an expression for the angle ϑ_x:

$$\begin{aligned}
\Delta_2 &= \Delta\rho \left(-\cos^2(\vartheta_x) + 1 \right) \\
\Delta_2 &= \Delta\rho \; \sin^2(\vartheta_x) \\
\sin^2(\vartheta_x) &= \frac{\Delta_2}{\Delta_1 + \Delta_2} \\
\vartheta_x &= \arcsin\left(\sqrt{\frac{\Delta_2}{\Delta_1 + \Delta_2}} \right)
\end{aligned} \tag{5.10}$$

For the presented data, this procedure suffers from the same limitations as the determination of H_a for the [100] stripes. It is necessary to a apply a magnetic field of sufficient intensity to saturate the magnetization for all field alignments in order to perform the linear translation of the fit of the flattest curve. For the data in Fig. 5.11, this is obviously not possible, since the linear regime of the highest and lowest curve is not reached. However, this procedure to calculate ϑ_x still serves well to evaluate magnetoresistance curves, even if an exact determination of ϑ_x is not possible.

For sample I, as shown in Fig. 5.11 (a), the flattest curve is the dark yellow one, corresponding to an angle of $\phi = 15°$. Δ_2 can be determined fairly accurately as

~ 0.2 kΩ. We estimate Δ_1 to be in the range of 3.1–3.8 kΩ, which results in an angle ϑ_x between 13–14°. While this is not a uniaxial anisotropy as observed for the [100] stipes, this result clearly documents a large influence of anisotropic strain on the easy axis orientation for [1$\bar{1}$0] oriented stripes.

In order to further affect the easy axis orientation, we anneal sample I for 50 hours at 185 °C and repeat the magnetoresistance measurements. We expect thermal treatment to affect the easy axis orientation because it is known to increase the carrier density, which mediates the ferromagnetic coupling according to the Zener model. The result of the procedure is shown in Fig. 5.11 (b). In contrast to the measurement before annealing, the flattest curve (purple, $\phi = 15°$) is now very close to the lowest curve (dark blue, $\phi = 0°$), leading to $\Delta_2 \sim 0.1$ kΩ. It is obvious that Δ_1 is now much larger relative to Δ_2 than before annealing, which is equivalent to a reduction of the easy axis orientation angle ϑ_x. This suggests, that the creation of a uniaxial easy axis is also possible for [1$\bar{1}$0] stripes by further increasing the strain in the stripe, possibly assisted by thermal treatment of the sample.

When annealing the sample to increase the uniaxial character of the stripe it is important to bear in mind that Sawicki et. al. have reported the appearance of a uniaxial easy axis along an in-plane $\langle 110 \rangle$ direction after annealing in unpatterned (Ga,Mn)As layers [Sawi 04]. To ascertain that the uniaxial easy axis in our stripes is indeed caused by patterning-induced stain modification and not purely by annealing, we conduct all magnetotransport measurements on [1$\bar{1}$0], as well as [110] stipes. So far, no perfectly uniaxial character could be demonstrated for [1$\bar{1}$0] stripes. Ongoing measurements on sample G are very promising though and are expected to yield the first purely uniaxial [1$\bar{1}$0] stripes in the very near future.

5.3 Shape Anisotropy

In early publications on micro-scale structured (Ga,Mn)As, the observed modification of the magnetic configuration of the structures has been attributed to shape anisotropy [Hama 04]. Shape anisotropy describes the phenomenon that a long, ferromagnetic bar is preferentially magnetized along its long axis. The external fields necessary to reverse the magnetization increases for narrower shapes. For metallic ferromagnets, such as cobalt or iron, this effect has been widely used [OHan 00]. However it is important to note that, although this effect is certainly present in nanostructured (Ga,Mn)As, the strength of this shape anisotropy depends on the magnetization, which is much smaller for (Ga,Mn)As then for ferromagnetic metals.

When described in terms of the magnetostatic energy equation (2.10), the effect of shape anisotropy is an additional uniaxial energy term $K_{uni} \sin^2(\vartheta - \vartheta_{uni})$, where ϑ_{uni} denotes the direction parallel to the long dimension of the ferromagnetic shape. Based purely on magnetostatics considerations, this $K_{uni} = K_{shape}$ is proportional to the square of the saturation magnetization M_s [OHan 00]:

$$K_{shape} = \Delta N \frac{\mu_0 M_s^2}{2}. \tag{5.11}$$

Even at 4K, the factor $\mu_0 M_s$ is much lower in (Ga,Mn)As (~ 0.05 T) than in typical ferromagnets such as Ni (~ 0.6 T) or Fe (~ 2.2 T) [Sawi 04]. ΔN is the difference in demagnetizing factors, which describes the geometry of the ferromagnet. To

determine ΔN, we follow the approach of [Ahar 98] for the geometry of a rectangular ferromagnetic prism. For sample A, with a stripe thickness of 70 nm, width of 200 nm, and a length of 100 μm, we calculate $\Delta N = 0.28$. According to Eqn. (5.11), this yields $K_{shape} \sim 280$ J/m^3. Divided by the volume magnetization (see Sec. 5.2.1) of 14 emu/cm^3, we get $K_{shape}/M \sim 20$ mT.

We have already established earlier, that the biaxial crystalline anisotropy is of the order of $K_{cryst}/M \sim 100$ mT. Comparing this to the calculated shape anisotropy field in sample A of $K_{shape}/M \sim 20$ mT, we note that shape anisotropy alone cannot be sufficient to overcome the intrinsic biaxial anisotropy. Indeed, magnetotransport measurements (see Fig. 5.10) reveal anisotropy fields in a range from $H_a = 45$ mT for sample A up to $H_a \sim 300$ mT for samples F and H, which is 2–15 times larger than the expected shape anisotropy.

Further proof that shape anisotropy is insufficient to explain the observed uniaxial anisotropy after patterning comes from a comparison of the magnetotransport measurements of sample A and B (Fig. 5.9 (a) and (b)). Both (Ga,Mn)As layers share identical dimensions as well as containing the same Mn content, which is equivalent to an identical ΔN and M_s. Both are therefore subject to the same contribution from shape anisotropy. However, the measured anisotropy field of sample B is significantly larger that that of sample A (80 mT compared to 45 mT). The only characteristic differentiating both samples is the lattice strain, which is larger for sample B. Based on these considerations, we can rule out shape anisotropy as the driving force in the observed occurrence of uniaxial magnetic anisotropy in our patterned samples.

5.4 A Model for Anisotropy Orientation

As shown in this chapter, the magnetic characterization of a multitude of processed (Ga,Mn)As stripe samples with different orientations reveals a manifold dependence of the orientation of the magnetic anisotropy on lattice strain. To understand these observations on a deeper level, we will discuss a phenomenological model on the basis of $\mathbf{k \cdot p}$ calculations (Sec. 2.2) and the magnetostatic domain energy landscape (Sec. 2.3).

The results of $\mathbf{k \cdot p}$ calculations by M. Schmidt, as outlined in Sec. 2.2, are presented in Fig. 5.13. The mean energy per valence band hole for a (Ga,Mn)As layer identical to the one used in samples A–C has been calculated and plotted for directions of $\mathbf{M}$ over a range of 180°. Starting with the pseudomorphic case, the layer is allowed to relax in x- and z-direction, while the lattice constant is kept fixed in y-direction. This corresponds exactly to the strain situation found in a stripe aligned along the [100] direction (x-axis).

We note, that for the pseudomorphic case (black curve in Fig. 5.13), the calculation qualitatively reproduces the biaxial anisotropy of the magnetostatic energy landscape in Fig. 2.4, if only the crystalline anisotropy term from Eqn. (2.10) is taken into account. With beginning strain relaxation, the energy minimum in [010] becomes less favorable for the magnetization and disappears entirely around $e_x = -0.6 \cdot 10^{-3}$. Above this value only a single energy minimum remains along the stripe direction in [100], which is characteristic of uniaxial behavior. All discussed stripe structures in Tbl. 5.1 surpass this strain value by a large margin, which matches with the observation of a strong uniaxial character in all patterned [100] stripes.
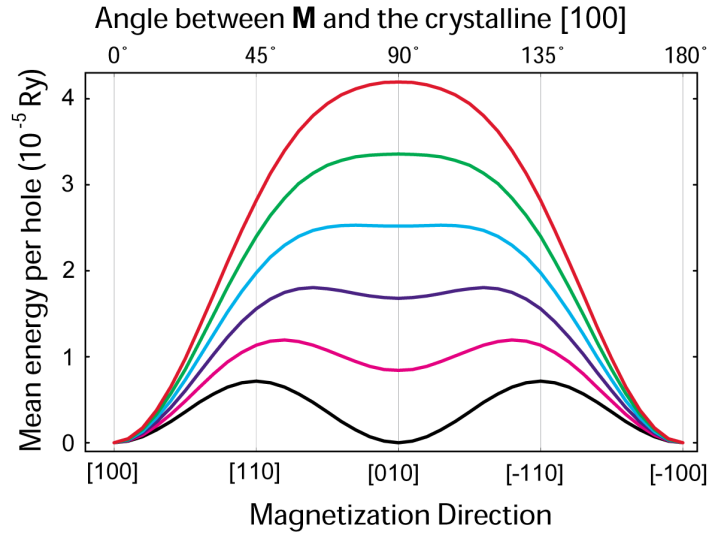
Figure 5.13: Theoretical $\mathbf{k} \cdot \mathbf{p}$ calculations of the mean energy per valence band hole of a (Ga,Mn)As layer with 2.5% Mn. The levels of the strain e_x range, in equal steps, from the pseudomorphic case ($e_x = -1.5 \cdot 10^{-3}$, black curve) to the fully relaxed case ($e_x = 0$, red curve). The strain e_y remains fixed at $-1.5 \cdot 10^{-3}$. The carrier density is assumed to be $4 \cdot 10^{20}$ cm^{-3}.
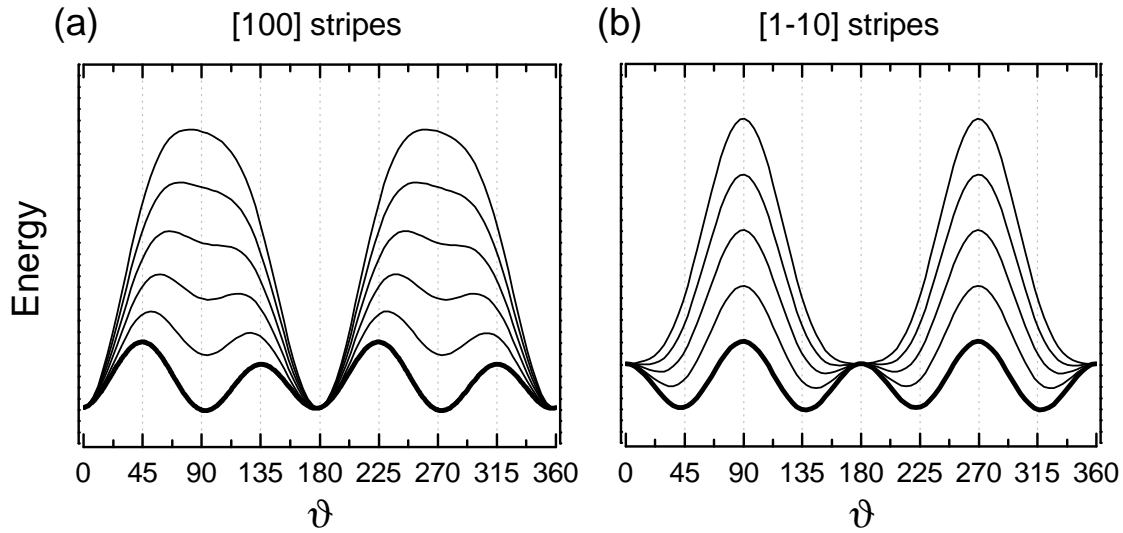

Figure 5.14: Magnetostatic energy landscape as calculated from Eqn. (2.10) (thick black line). The influence of stain is represented by an additional uniaxial term $K_{strain} \sin^2(\vartheta)$. The magnitude of this term is increased in steps of $0.25 K_{cryst}$ for (a) [100] stripes and (b) [1$\bar{1}$0] stripes. For both plots, $\vartheta = 0°$ is parallel to the stripe direction.

In the energy landscape picture (which we have shown to be consistent with $\mathbf{k} \cdot \mathbf{p}$ calculations), a uniaxial anisotropy takes the form of a term with a $\sin^2(\vartheta)$ symmetry. In unpatterned layers, such contributions are already present in the $K_{uni[\bar{1}10]}$ and $K_{uni[010]}$ terms. We introduce an additional term K_{strain} to represent the influence of strain on the energy landscape.

First, we will investigate the influence of strain on [100] stipes. Fig. 5.14 (a) shows the energy landscape of an unpatterned layer (thick black line), which is dominated by the biaxial crystalline anisotropy given by K_{cryst}. The influence of strain is taken into account by the term $K_{strain} \sin^2(\vartheta)$, which is zero for the unpatterned layer. We expect this term to increase with strain, as induced by patterning of the stripes. In the plot, this is represented by increasing its magnitude in increments of $0.25 K_{cryst}$. We observe, that the energy minimum at 90° diminishes as the uniaxial strain term becomes more dominant. By the time when K_{strain} reaches a value of 75% K_{cryst}, the energy minimum has completely disappeared and only a single global easy axis along the stripe axis remains.

According to this picture, a rather large uniaxial term close to the order of the biaxial crystalline anisotropy would be needed to cause the appearance of a global uniaxial easy axis. In practice, this is not the case, as can be seen from the measurements on sample A in Fig. 5.9 (a). Here, we find an anisotropy field of only 45 mT compared to $K_{cryst}/M \sim 100$ mT. Two reasons for this discrepancy are explained in the following.

Firstly, the interplay between the anisotropic strain relaxation and the crystalline anisotropy is not a simple superposition of energy terms as implied in the above discussion. Both anisotropy terms are coupled to the crystal lattice of the sample. As such, we have to assume that the biaxial crystalline anisotropy term is also affected by the induced relaxation. Since the symmetry of the crystal is lowered, we expect the influence of the biaxial term to be smaller than in the unpatterned case, which would allow the K_{strain} term to dominate the energy landscape even though it is smaller than the original value of K_{cryst}.

Secondly, the [$\bar{1}10$] uniaxial anisotropy, which is always present in (Ga,Mn)As layers, works in favor of the strain-induced uniaxial character. Without this contribution, the energy maxima separating the easy axes would be of equal height. The [$\bar{1}10$] anisotropy increases the height of one of these hard axes (see Fig. 2.4). A value of $K_{uni[\bar{1}10]} = 10\%$ K_{cryst}, which is assumed in Fig. 5.14 (a), is sufficient to eliminate the remaining shallow local energy minimum at 90° for $K_{strain} = 75\%$ K_{cryst}. An even earlier onset of uniaxial behavior can be expected for some samples, as values of $K_{uni[\bar{1}10]}/K_{cryst}$ exceeding 20% have been reported in (Ga,Mn)As layers [Goul 08].

In the case of [$1\bar{1}0$] stripes, the situation is different. Now, the stripes are aligned along one of the natural hard axes of the material. Stain relaxation and increasing tensile strain via a stressor layer again strengthens the K_{strain} term. However, contrary to the [100] stripes, it does not directly act on one of the easy axes. Instead it increases the height of the existing hard axis perpendicular to the stripe alignment, as shown in Fig. 5.14 (b). Due to the corresponding increase in with of the hard axis, the original easy axes at 45° to the stripe direction are 'pushed away' from the hard axis perpendicular to the stripes. In Fig. 5.14 (b), we observe this effect as a rotation of the easy axis towards the [$1\bar{1}0$] direction parallel to the stripes. We expect the two minima to merge at the position of the former [$1\bar{1}0$] hard axis at a value of $K_{strain} \sim$

100% K_{cryst}, thus defining a single global easy axis parallel to the stripe direction.

We have observed evidence of this phenomenon in the magnetotransport measurements after patterning, see Fig. 5.11. For the case of sample I, the patterning induced strain shifts the easy axis from 45° to an angle of 13–14° to the stripe direction.

Chapter 6

Device Application

As stated in the beginning, the ultimate goal of this work was to establish a well-understood foundation for the design of a class of novel devices which make use of multiple connected regions with individually engineered anisotropy properties. In this chapter, we present investigations on the first such device as published by K. Pappert et. al. [Papp 07d].
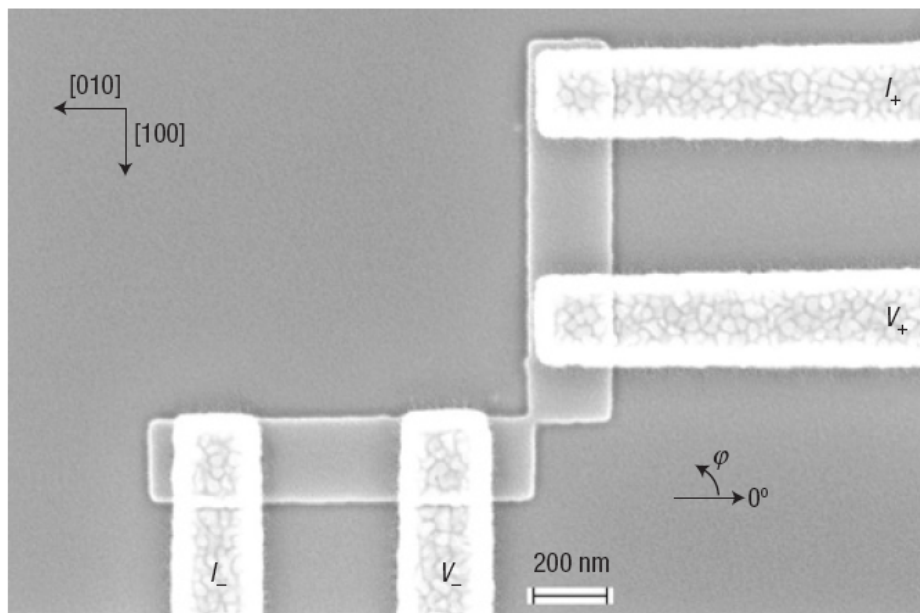

Figure 6.1: SEM image of the L-shaped structure consisting of two connected (Ga,Mn)As nanobars. The bright stripes leading to the image edges are Ti/Au current and voltage leads. The definition for the writing angle φ as well as current and voltage are indicated.

The device is shown in Fig. 6.1 and consists of two (Ga,Mn)As nanobars which are oriented perpendicular to each other and connected at one of the edges via a constriction. The resistance of an electrical current driven through this constriction depends on the relative magnetization states of the nanobars and is determined by the AMR effect.

6.1   Device Operation

The 20 nm thick (Ga,Mn)As layer used for the fabrication of the device contains 2.5% Mn and is grown by the standard procedure as detailed in Sec. 3.2.5. The two orthogonal nanobars of which the device consists have a length of 1 μm and a width of 200 nm. Despite the shorter length compared to the stripes discussed in earlier chapters, we expect a similar relaxation behavior. Detailed simulation results will be presented in the following section. Several constrictions in the range of some tens of nm have been investigated. In this chapter, the characteristics of two structures representing two different types of behavior depending on constriction width (measured as the length of the corner-to-corner diagonal) are discussed. In addition to the patterning procedure of the nanobars by electron beam lithography (EBL) and chemically assisted ion beam etching, Ti/Au contacts are defined in another EBL step through metal evaporation and lift-off. Transport measurements have been performed to confirm that both stripes are completely uniaxial.

To operate the device, transport measurements are carried out at 4 K in a magnetocryostat in which a vector field of up to ± 300 mT can be applied in any direction. An initial device state can be 'written' by an in-plane magnetic field of 300 mT along a writing angle φ (see Fig. 6.1). The writing field aligns the magnetic moments in the bars. When the field is reduced back to zero, the magnetization will relax to the closest easy axis. Due to the easy axis along the nanobar, four possible magnetization configurations can be achieved, depending in which direction the magnetic moments are aligned in each bar. We measure the four-terminal resistance of the constriction in the written remanent state by applying a voltage V_b to the current leads (I_+ and I_-) and recording the voltage drop between contacts V_+ and V_-, as defined in Fig. 6.1.

The polar plot of Fig. 6.2 shows the constriction resistance as a function of the writing angle φ. Two distinct resistance values are visible. The high resistance state is prepared by writing the device in the first quadrant ($-3° \leq \varphi < 98°$), while the low resistance state occupies the second quadrant ($98° < \varphi < 167°$). The whole plot is point symmetric with respect to the origin.

With these properties, the structure can be viewed as the basis of a non-volatile ferromagnetic semiconductor memory device. Information can be stored in a magnetic semiconductor by saving it in the relative magnetization orientation of two orthogonally oriented nanobars. No power is required to conserve the information due to the stability of the orientation of magnetic moments. The information read-out via resistance measurement over the constriction offers a large on/off resistance ratio. Values up to 280% have already been achieved by tuning the device geometry [Papp 07d].

6.2   The Role of the Constriction

The four possible magnetic states sketched in Fig. 6.2 fall into two groups. The nanobars in inset (i) and (iii) are magnetized 'in series', i.e. the magnetization vectors meet in a head-to-tail configuration. In contrast to this, in (ii) and (iv), both magnetization vectors point towards (head-to-head) or away from (tail-to-tail) the constriction. The head-to-tail configuration is somewhat preferred due to magnetostatic interactions between the bars. This effect is caused by a small repulsive field of the order of 2 mT, resulting from the wrong poles meeting at the connected tips of the bars. The magnetic
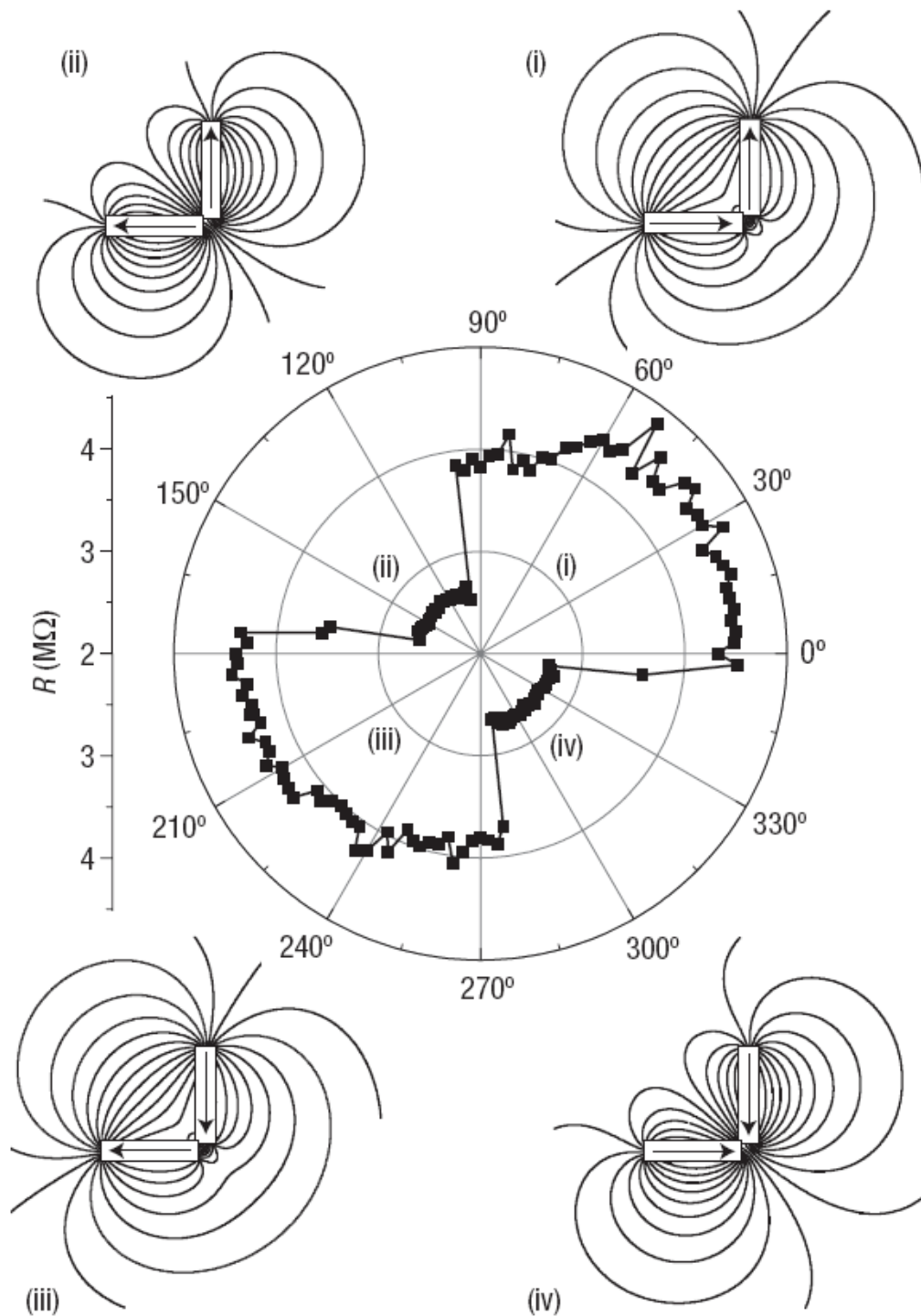
Figure 6.2: Polar plot of the constriction resistance as a function of the writing angle φ. Two resistance states (high/low) are observed and related to the four possible magnetic configurations of the nanobars, as sketched with corresponding field line patterns in insets (i)–(iv).

field line patterns in the sketches in Fig. 6.2 (i)–(iv) are calculated using a simple bar magnet model. The field lines are close to parallel to the current for the head-to-tail configuration. In the tail-to-tail and the head-to-head configuration, the field lines are approximately perpendicular to the current.

The resistance difference between the head-to-tail ($\mathbf{M} \parallel \mathbf{J}$) and head-to-head ($\mathbf{M} \perp \mathbf{J}$) configurations is caused by a special variation of the AMR effect. As discussed earlier (see transport measurements in Chapter 5), the AMR effect can only account for a few percent resistance difference between the two states. However, in Fig. 6.2, not only is the difference between the two states of the order of a few hundred percent, but the angular dependence is also inverted. We observe the low resistance state for $\mathbf{M} \perp \mathbf{J}$, which we would expect for $\mathbf{M} \parallel \mathbf{J}$ in the typical AMR picture.

For several wide constrictions, a typical AMR effect as described in the earlier chapters has been observed. For these constrictions we also measure a 100 times lower constriction resistance. K. Pappert et. al. ascribe the different behavior of the presented sample with a narrow constriction to the occurrence of depletion in the constriction which drives the transport in this region from metallic transport into the hopping regime. One possible reason for the depletion of the constriction region, namely large, geometry dependent strain fields, will be discussed in the following.

We investigate the strain distribution around the constriction area by a series of 3D finite element simulations as introduced in Chapter 4. The results for two constriction widths are shown in Fig. 6.3. The upper row ((a)–(c)) plots the strains e_x and e_z as well as the shear strain e_{xy} for a 10 nm wide constriction. As a comparison to this set, the lower row ((d)–(f)) contains identical plots for a 50 nm wide constriction. We will only discuss e_x and omit e_y, as they transform into each other when the whole geometry is rotated by 90°.

First of all, we note several general trends. The relaxation of the stripe as a whole is not appreciably influenced by the constriction. The average strain values in a cross section in the middle of the stripe oriented along y are:

$$e_x = -0.41 \cdot 10^{-3}; \qquad e_y = -1.49 \cdot 10^{-3}; \qquad e_z = 0.81 \cdot 10^{-3}.$$

If we compare these values to sample A in Tbl. 5.1, we note slightly different values for all three strains, which is mainly caused by the reduced length of the stripes (1 μm versus 100 μm). This results in a slight relaxation of the strain in y-direction, i. e. parallel to the stripes, which lessens the pressure in the two perpendicular directions x and z. Although the strain values are lower than those of all investigated stripe structures in the previous chapter, they are still well within the region, where the $\mathbf{k} \cdot \mathbf{p}$ calculations predict uniaxial behavior (see Sec. 5.4), which we indeed observe by magnetotransport measurements in one arm of the device.

The edges of the constriction show small, highly compressively strained regions, where e_x reaches values as high as $-5.10 \cdot 10^{-3}$ (deep blue regions in Fig. 6.3 (a) and (d)). In this area, the opposing strain fields of both stripes (e_x for one bar and e_y for the other) overlap, thus exerting pressure on the material from two directions and preventing relaxation in either. The situation for e_z is similar. The opposing and overlapping in-plane strain fields prevent relaxation in x and y-direction and consequently force the material to further expand in z-direction. This effect causes the yellow to red regions in (b) and (e), where e_z is increased up to $2.00 \cdot 10^{-3}$. Finally, we also note the appearance of shear strain in the constriction region, which is usually negligibly
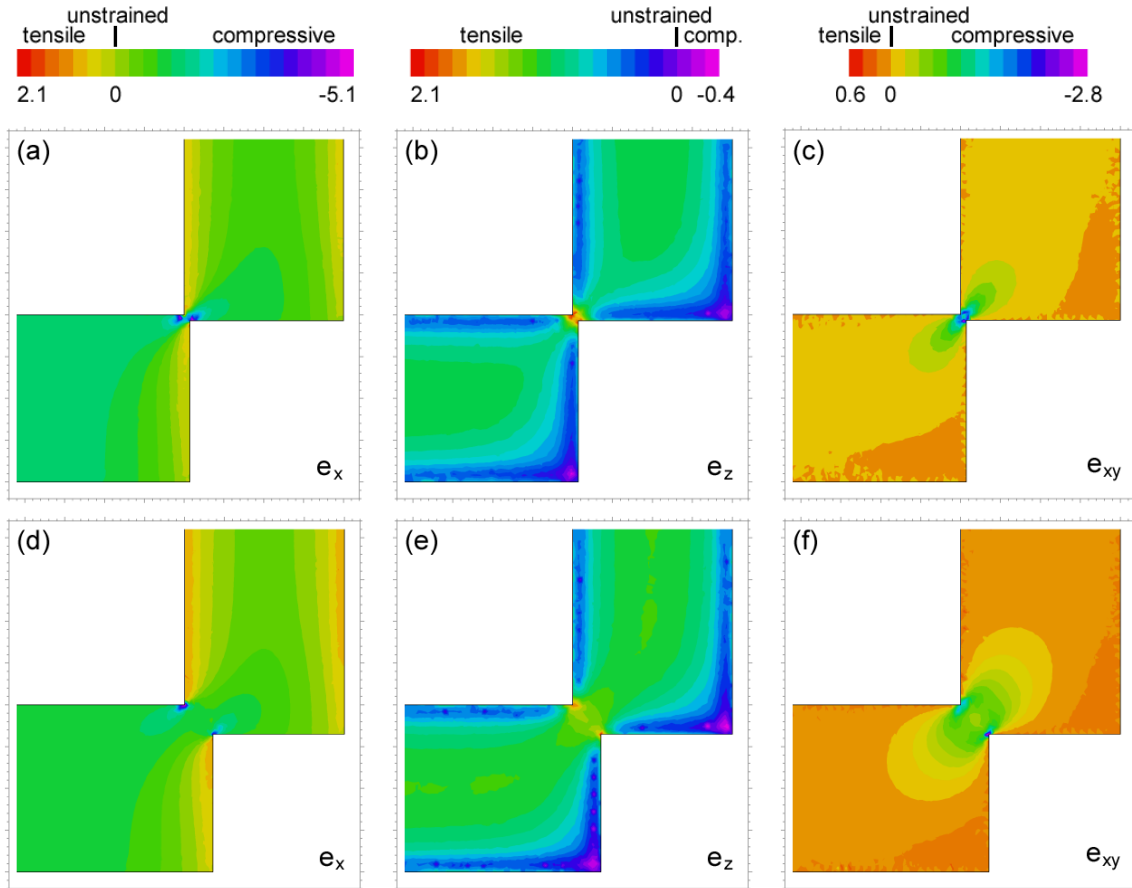
Figure 6.3: Simulation of the strain distribution around the region where two nanobars are connected by a constriction. The displayed region is a cross section (top view) through the x-y-plane at half height of the (Ga,Mn)As layer. The stripes are 200 nm wide and 1 μm long; the plots are zoomed on the constriction region. The constriction width is 10 nm for plots (a)–(c) and 50 nm for (d)–(f). The values in the scale are given in units of 10^{-3}.

small in [100]-oriented bars. However, due to the suppressed in-plane relaxation in the constriction region, the shear strain e_{xy} can reach values up to $-2.60 \cdot 10^{-3}$ in the green to dark blue regions in (c) and (f).

When comparing the strains around the constriction area for the 10 nm and 50 nm wide constriction, we note that the peak values for all three strains is actually not much different. The main effect of the narrower constriction is that the regions of maximum strain move closer together. As a consequence to this, the strain in the region between the peaks also increases in magnitude. The 'channel' of comparatively low strain connecting the two bars in the 50 nm constriction is mostly gone in the 10 nm constriction.

To quantify this effect, we calculate the average strains in a vertical cross section through the constriction. The results for a series of varying widths are displayed in Fig. 6.4. The average strain value is relatively unaffected by constriction widths down to 30–20 nm. Beyond this value, we observe a noticeable increase for all strains. However, it is important to keep in mind that these values do not contain the regions
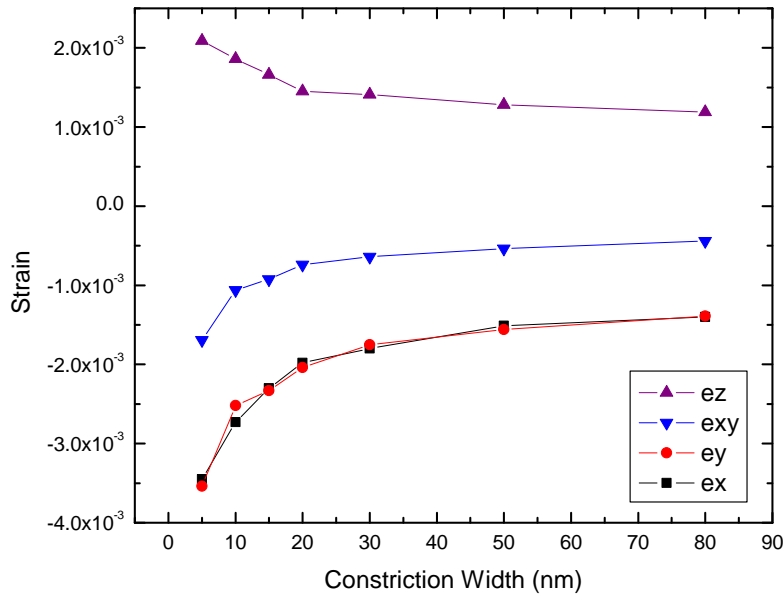
Figure 6.4: Average simulated strain values in a vertical cross section through a constriction with varying width. Only the strain in the (Ga,Mn)As layer is shown.

of highest strain for e_x and e_{xy}. For the former, the highest value is found to the left and right of the constriction. Additionally, an according highly compressive region of e_y exists above and below the constriction. The shear strain forms a structure similar to a ring around the center of the constriction, with two clubs extending deeper into the bulk of the stripes.

With the simulation results displayed in Fig. 6.4, we calculate the band structure of (Ga,Mn)As (see Sec. 2.2) in a 10 nm constriction and compare these values with the band structure in the center of the stripe, and a pseudomorphically strained layer without any strain relaxation. Table 6.1 summarizes the energies of the four valence bands for the three different cases. We note that the energy E_1 of the topmost band is lower in the constriction than in the relaxed stripes, thus slightly increasing the bandgap energy. However, the shift is only 3 meV, which is certainly too low to deplete the constriction. The effect of strain on the other bands is also not notably larger. Performing the same calculations for the regions of highest strains around the constriction also yields shifts of a magnitude of only a few meV. It therefore seems unlikely that strain is the main driving mechanism which causes depletion of the whole constriction region. In reality, side wall damage caused by etching will also play an important role in degradation of the interface region, as it may penetrate deep enough (several nm) into the material to affect the whole volume of a very thin constriction. We therefore expect a combination of several factors to play a role in the depletion of the constriction.

Of course, the kind of simulations presented in Fig. 6.3 is not limited to the geometry of this particular device. The results discussed in this chapter also remain true for other types of constrictions. For example, Rüster et. al. report a very similar very large magnetoresistance effect in a double constriction of a single (Ga,Mn)As wire [Rüst 03]. Strain simulations for this geometry also display the small charac-

Table 6.1: Calculation of the energy E of the four top valence bands in meV at Γ in a 10 nm (Ga,Mn)As constriction. The values are given with respect to the energy of the degenerate bands without spin-orbit coupling and strain (defined as zero, see Sec. 2.2). The magnetization in the constriction is assumed to point in [110] direction.

bands in	E_1	E_2	E_3	E_4
pseudomorphic layer	46.3	10.7	-20.1	-44.6
relaxed stripe	45.9	10.3	-19.7	-44.1
constriction	42.9	12.7	-20.7	-50.6

teristic regions around the corners of the constriction where the strain reaches a peak value. The strain distribution behavior with increasingly narrow constrictions as shown in Fig. 6.4 also reproduces qualitatively for this geometry.

Chapter 7

Conclusion and Outlook

The detailed understanding of the (Ga,Mn)As material system as a model system for the class of dilute magnetic semiconductors is one of the foundations for the progress of the field of spintronics in general. Understanding in this case encompasses a wide field of different subjects, some of which have been touched in this thesis. All experimental approaches have to begin with understanding the intricacies associated with mastering the trade of MBE and the wide range of possible characterization methods, outlined in the second and third chapter of this work. Although the epitaxial growth of (Ga,Mn)As can look back on several years of experience now, there is still room for improvement. It is not yet possible to produce (Ga,Mn)As layers, in which the Mn content notably exceeds the 10% border, which limits the carrier dependent Curie temperature. One goal for growth is to increase T_C beyond the current record of 180 K [Olej 08]. Other examples of notable topics related to the work at Würzburg are the fabrication of ultrathin layers (< 3 nm) or the use of (Ga,Mn)As layers as a source of spin-polarized carriers in a p-i-n diode structure.

More closely related to the subject of this thesis is the ongoing investigation of the connection between strain and magnetic anisotropy in (Ga,Mn)As. G. Dengel et. al. have demonstrated the combination of lithographically patterned (Ga,Mn)As stripes and a neighboring continuous layer in a single sample which yields a complex magnetic anisotropy response, with possible new device applications [Deng 08b]. Another example is the further development of the memory cell prototype introduced in Chapter 6. By expanding the concept of connected and locally controlled magnetized regions into larger and more complex structures, it will soon be possible to construct an all-electrical all-semiconductor non-volatile logic circuit.

An experimental avenue which has yet to be explored is the utilization of lithographic anisotropy control to produce samples with a perpendicular to plane oriented easy axis. So far, out of plane easy axes have been produced by inducing tensile strain in a (Ga,Mn)As layer via growth on a relaxed buffer with larger lattice constant such as (In,Ga)As [Liu 05, Xian 05]. The drawback of this method is the plastic relaxation of the buffer layer through the formation of lattice defects resulting in poor layer and surface quality. With the lithographic patterning technique, it is possible to write an array of nanopillars on a highly strained but pseudomorphic (Ga,Mn)As layer with underlying stressor, analogous to the stripe samples. The resulting elastic relaxation circumvents the problems of lattice defect formation while still providing the biaxial tensile strain needed to achieve the easy axis reorientation.

In addition to the apparent technological potential of lithographic anisotropy control, it also allows for novel sample designs to study more fundamental physics, such as the resistance connected to the geometrical confinement of a domain wall or possibly the spin transport between sources of orthogonal spin orientation.

Finally, the 3D finite element strain simulations have already proven to be an invaluable tool for understanding the strain relaxation in a wide variety of (Ga,Mn)As structures. Being able to accurately predict the strain in complex geometries greatly facilitates the design of novel samples with respect to the desired functionality. The most recent generation of simulations is able to take into account effects such as slanted side walls or rounded structures in addition to the features discussed in Chapter 4. A possible future simulation application could be the calculation the strain in layers with a material composition gradient and inhomogeneities for an even more realistic representation of experimental conditions.

Appendix A

Band Structure Hamiltonians

A.1 Kohn-Luttinger Hamiltonian H_{KL}

The six-band model Kohn-Luttinger Hamiltonian H_{KL} is given by:

$$
\mathrm{H}_{KL} = \left(
\begin{array}{cccc|cc}
\mathcal{H}_{hh} & -c & -b & 0 & \dfrac{b}{\sqrt{2}} & c\sqrt{2} \\[2mm]
-c^* & \mathcal{H}_{lh} & 0 & b & -\dfrac{b^*\sqrt{3}}{\sqrt{2}} & -d \\[2mm]
-b^* & 0 & \mathcal{H}_{lh} & -c & d & -\dfrac{b\sqrt{3}}{\sqrt{2}} \\[2mm]
0 & b^* & -c^* & \mathcal{H}_{hh} & -c^*\sqrt{2} & \dfrac{b^*}{\sqrt{2}} \\[2mm]
\hline
\dfrac{b^*}{\sqrt{2}} & -\dfrac{b\sqrt{3}}{\sqrt{2}} & d^* & -c\sqrt{2} & \mathcal{H}_{so} & 0 \\[2mm]
c^*\sqrt{2} & -d^* & -\dfrac{b^*\sqrt{3}}{\sqrt{2}} & \dfrac{b}{\sqrt{2}} & 0 & \mathcal{H}_{so}
\end{array}
\right) \tag{A.1}
$$

The upper left 4×4 section of (A.1) is the four band model Hamiltonian, which neglects the spin split-off bands. The components of (A.1) are:

$$
\mathcal{H}_{hh} = \frac{\hbar^2}{2m}[(\gamma_1 + \gamma_2)(k_x^2 + k_y^2) + (\gamma_1 - 2\gamma_2)k_z^2], \tag{A.2}
$$

$$
\mathcal{H}_{lh} = \frac{\hbar^2}{2m}[(\gamma_1 - \gamma_2)(k_x^2 + k_y^2) + (\gamma_1 + 2\gamma_2)k_z^2],
$$

$$
\mathcal{H}_{so} = \frac{\hbar^2}{2m}\gamma_1(k_x^2 + k_y^2 + k_z^2) + \Delta_{so},
$$

$$
b = \frac{\sqrt{3}\hbar^2}{m}\gamma_3 k_z(k_x - ik_y),
$$

$$
c = \frac{\sqrt{3}\hbar^2}{2m}[\gamma_2(k_x^2 - k_y^2) - 2i\gamma_3 k_x k_y],
$$

$$
d = -\frac{\sqrt{2}\hbar^2}{2m}\gamma_2[2k_z^2 - (k_x^2 + k_y^2)].
$$

In GaAs, the Kohn-Luttinger parameters are $(\gamma_1, \gamma_2, \gamma_3) = (6.85, 2.1, 2.9)$. The split-off energy gap is $\Delta_{so} = 0.341$ eV.

A.2 Strain Hamiltonian H_e

The strain Hamiltonian H_e for the four band model as described in [Bir 74] is

$$\mathrm{H}_e = \begin{pmatrix} f & h & j & 0 \\ h^* & g & 0 & j \\ j^* & 0 & g & -h \\ 0 & j^* & -h^* & f \end{pmatrix}, \tag{A.3}$$

where

$$f = \frac{l+m}{2}(e_{xx} + e_{yy}) + m e_{zz}, \tag{A.4}$$

$$g = \frac{1}{3}\{f + 2[m(e_{xx} + e_{yy}) + l e_{zz}]\},$$

$$h = -\frac{1}{\sqrt{3}}\, n(i e_{xz} + e_{yz}),$$

$$j = \frac{1}{\sqrt{3}}\left[\frac{1}{2}(l - m)(e_{xx} - e_{yy}) - i n e_{xy}\right].$$

In these equations, the constants l, m and n are linked to the deformation potentials a, b and d by

$$a = \frac{l + 2m}{3}, \qquad b = \frac{l - m}{3}, \qquad d = \frac{n}{\sqrt{3}}. \tag{A.5}$$

The values for the deformation potentials of GaAs are taken from [Vurg 01]:

$$a = -1.16 \text{ eV}, \qquad b = -2.0 \text{ eV}, \qquad d = -4.8 \text{ eV}.$$

Appendix B

Sample FlexPDE Input File

The following section contains a working example of a FlexPDE 5 simulation input file. The structure in this simulation is a 3D GaAs/(Ga,Mn)As stripe. Comments marked by curly brackets are ignored by the programm.

TITLE

'3D (100) GaMnAs stripe '

SELECT

```
errlim =0.01        {determines calculation accuracy}
nominmax            {removes markers from contour plots}
painted             {colored contour plots}
```

COORDINATES

```
cartesian3
```

VARIABLES

```
Up                  {displacement vectors}
Vp
Wp
```

DEFINITIONS

```
l = 10              {total stripe length}
w = 1.0             {half width of stripe}
hmn = 0.7           {layer thickness (Ga,Mn)As}
ha = 1.4            {height of etched GaAs}
hsub = 1            {substrate thickness}

Tp                  {temperature value}
```

```
Tga = 0.00            {GaAs temperature}
Tmn = 15              {(Ga,Mn)As temperature}

offset = −1.5e−3 {normalizes strain to relaxed lattice
    constant of (Ga,Mn)As}

C11 = 11.9e11         {elastic moduli of GaAs in dyn/cm^2}
C12 = 5.34e11
C44 = 5.96e11

b = 2.258e8          {see Section 4.3.1}

ex = dx(Up)                              {strain in x−direction}
ey = dy(Vp)
ez = dz(Wp)
exy = 0.5*(dy(Up) + dx(Vp))             {shear strains}
exz = 0.5*(dz(Up) + dx(Wp))
eyz = 0.5*(dz(Vp) + dy(Wp))
Sx = C11*ex + C12*ey + C12*ez− b*Tp     {stress in x−direction}
Sy = C12*ex + C11*ey + C12*ez− b*Tp
Sz = C12*ex + C12*ey + C11*ez − b*Tp
Txy = C44*2*exy                         {shear stresses}
Txz = C44*2*exz
Tyz = C44*2*eyz
```

EQUATIONS

```
Up: dx(Sx) + dy(Txy) + dz(Txz) = 0      {displacement equations}
Vp: dx(Txy) + dy(Sy) + dz(Tyz) = 0
Wp: dx(Txz) + dy(Tyz) + dz(Sz) = 0
```

CONSTRAINTS

```
integral(Up) = 0                        {prevents rigid body motion}
integral(Vp) = 0
integral(Wp) = 0
```

EXTRUSION

```
surface 'substrate bottom' z = 0
layer 'substrate'
surface 'substrate top' z = hsub
layer 'GaAs stripe'
surface 'GaAs top' z = hsub + ha
layer 'GaMnAs stripe'
surface 'GaMnAs top' z = hsub + ha + hmn
```

BOUNDARIES

```
surface 'substrate bottom' value(Up) = 0 value(Vp) = 0 value(
    Wp) = 0  {substrate bottom fixed}

limited region 1     {GaAs substrate base}

 Tp = Tga
 layer 'substrate'
 start(-w-1,-l)
 value(Up) = 0 value(Vp) = 0 line to (-w-1,l) to (w+1,l) to (w
    +1,-l) to close

 limited region 2   {GaAs stripe base}

 Tp = Tga
 layer 'GaAs stripe'
 start(-w,-l)
 line to (-w,l) to (w,l) to (w,-l) to close

limited region 3     {(Ga,Mn)As stripe base}

 Tp = Tmn
 mesh_density = 2
 layer 'GaMnAs stripe'
 start(-w,-l)
 line to (-w,l) to (w,l) to (w,-l) to close
```

PLOTS

```
 grid(x,y,z)
 grid(x+100*Up,y+100*Vp, z+100*Wp) as "3D deformation"
 grid(x+100*Up, z+100*Wp) as "x-z deformation" on y = 0
 vector(Up,Wp) as "x-z displacement" on y = 0

 contour(ex) as "epsilon-x" on y = 0
 contour(ex + offset) as "true epsilon-x" on y = 0 on region 3
 export format "#x#b#z#b#1" frame (-w,hsub+ha,2*w,hmn) file "
    export (100) GaMnAs ex.tbl"
 contour(ex + offset) as "true epsilon-x" on z = hsub+ha+(hmn
    /2)

 contour(ez) as "epsilon-z" on y = 0
 contour(ez + offset) as "true epsilon-z" on y = 0 on region 3
 export format "#x#b#z#b#1" frame (-w,hsub+ha,2*w,hmn) file "
    export true (100) GaMnAs only ez.tbl"
```

```
contour(ey) as "epsilon-y" on y = 0
contour(ey + offset) as "true epsilon-y" on y = 0 on region 3
contour(ey + offset) as "true epsilon-y" on z = hsub+ha+(hmn
    /2)

contour(exy) as "shear strain exy" on y = 0
contour(exz) as "shear strain exz" on y = 0
contour(eyz) as "shear strain eyz" on y = 0

end
```

Bibliography

[Abol 01] M. Abolfath, T. Jungwirth, J. Brum, and A. MacDonald, Phys. Rev. B **63**, 054418 (2001).

[Ahar 98] A. Aharoni, J. Appl. Phys. **83**, 3432 (1998).

[Aker 05] J. Åkerman, Science **308**, 508 (2005).

[Awsc 07] D. D. Awschalom and M. E. Flatté, Nature Physics **3**, 153 (2007).

[Baib 88] a) M. N. Baibich, J. M. Broto, A. Fert, F. Nguyen Van Dau, F. Petroff, P. Etienne, G. Creuzet, A. Friederich, and J. Chazelas, Phys. Rev. Lett. **61**, 2471 (1988); b) G. Binasch, P. Grünberg, F. Saurenbach, and W. Zinn, Phys. Rev. B **39**, 4828 (1989).

[Baxt 02] D. V. Baxter, D. Ruzmetov, J. Scherschligt, Y. Sasaki, X. Liu, J. K. Furdyna, and C. H. Mielke, Phys. Rev. B **65**, 212407 (2002).

[Bieg 90] D. K. Biegelsen, R. D. Bringans, J. E. Northrup, and L. E. Swartz, Phys. Rev. B **41**, 5701 (1990).

[Bir 74] G. L. Bir and G. E. Pikus, *Symmetry and Strain-Induced Effects in Semiconductors*, Wiley, New York (1974).

[Bran 73] W. A. Brantley, J. Appl. Phys. **44**, 534 (1973).

[Call 66] H. B. Callen and E. Callen, J. Phys. Chem. Solids **27**, 1271 (1966).

[Camp 03] R. P. Campion, K. W. Edmonds, L. X. Zhao, K. Y. Wang, C. T. Foxon, B. L. Gallagher, and C. R. Staddon, J. Cryst. Growth **247**, 42 (2003).

[Cohe 94] G. Cohen-Solal, F. Bailly, M. Barbé, J. Cryst. Growth **138**, 68 (1994).

[Cunn 86] J. E. Cunningham, T. H. Chiu, A. Ourmazd, J. Shah, and W. T. Tsang, J. Appl. Phys. **60**, 4165 (1986).

[Deng 08a] R. G. Dengel, *Anisotropiekontrolle in (Ga,Mn)As mittels Elektronenstrahllithograhpie*, Diplomarbeit, Universität Würzburg (2008).

[Deng 08b] R. G. Dengel, C. Gould, J. Wenisch, K. Brunner, G. Schmidt, and L. W. Molenkamp, New J. Phys. **10**, 073001 (2008).

[Diet 00] T. Dietl, H. Ohno, F. Matsukura, J. Cibert, and D. Ferrand, Science **287**, 1019 (2000).

[Diet 01] T. Dietl, H. Ohno, and F. Matsukura, Phys. Rev. B **63**, 195205, (2001).

[Edmo 04] K. W. Edmonds, P. Bogusławski, K. Y. Wang, R. P. Campion, S. N. Novikov, N. R. S. Farley, B. L. Gallagher, C. T. Foxon, M. Sawicki, T. Dietl, M. Buongiorno Nardelli, and J. Bernholc, Phys. Rev. Lett. **92**, 037201 (2004).

[Fuji 87] K. Fujiwara, K. Kanamoto, Y. N. Ohta, Y. Tokuda, and T. Nakayama, J. Cryst. Growth **80**, 104 (1987).

[Goen 05] S. T. B. Goennenwein, S. Russo, A. F. Morpurgo, T. M. Klappwijk, W. van Roy, and J. de Boeck, Phys. Rev. B **71**, 193306 (2005).

[Goul 04] C. Gould, C. Rüster, T. Jungwirth, E. Girgis, G. M. Schott, R. Giraud, K. Brunner, G. Schmidt, and L. W. Molenkamp, Phys. Rev. Lett. **93**, 117203 (2004).

[Goul 08] C. Gould, S. Mark, K. Pappert, R. G. Dengel, J. Wenisch, R. P. Campion, A. W. Rushforth, D. Chiba, Z. Li, X. Liu, W. Van Roy, H. Ohno, J. K. Furdyna, B. Gallagher, K. Brunner, G. Schmidt, and L. W. Molenkamp, New J. Phys., **10**, 055007 (2008).

[Grun 89] M. Grundmann, U. Lienert, D. Bimberg, A. Fischer-Colbrie, and J. N. Miller, Appl. Phys. Lett. **55**, 1765 (1989).

[Hama 04] K. Hamaya, R. Moriya, A. Oiwa, T. Taniyama, Y. Kitamoto, Y. Yamazaki, and H. Munekata, Jpn. J. Appl. Phys. **43**, L306 (2004).

[Haya 01] T. Hayashi, Y. Hashimoto, S. Katsumoto, and Y. Iye, Appl. Phys. Lett. **78**, 1691 (2001).

[Hein 95] H. Heinke, S. Einfeldt, B. Kuhn-Heinrich, G. Plahl, M. O. Möller, and G. Landwehr, J. Phys. D: Appl. Phys. **28**, A104 (1995).

[Huem 07] S. Hümpfner, K. Pappert, J. Wenisch, K. Brunner, C. Gould, G. Schmidt, L. W. Molenkamp, M. Sawicki, and T. Dietl, Appl. Phys. Lett. **90**, 102102 (2007).

[Ibac 03] H. Ibach, H. Lüth, *Solid State Physics*, 3rd ed., Springer Verlag (2003).

[IOFFE] NSM Archive, webpage, Ioffe Physico-Technical Institute, <http://www.ioffe.ru/SVA/NSM/Semicond/index.html>.

[Jan 57] J. P. Jan, *Solid State Physics* (Eds: F. Seits, D. Turnbull), Academic Press Inc. New York (1957).

[Kitt 05] C. Kittel, *Introduction to solid state physics*, 8th ed., John Wiley & Sons, Inc. (2005).

[Liu 95] X. Liu, A. Prasad, J. Nishio, E. R. Weber, Z. Liliental-Weber, and W. Walukiewicz, Appl. Phys. Lett. **67**, 279 (1995).

[Liu 05] X. Liu, W. L. Lim, L. V. Titova, M. Dobrowolska, J. K. Furdyna, M. Kutrowski, and T. Wojtowicz, J. Appl. Phys. **98**, 63904 (2005).

[Lutt 55] J. M. Luttinger and W. Kohn, Phys. Rev. **97**, 869 (1955).

[McGu 75] T. R. McGuire and R. I. Potter, IEEE Trans. Magn. **11**, 1018 (1975).

[Myer 06] R. C. Myers, B. L. Sheu, A. W. Jackson, A. C. Gossard, P. Schiffer, N. Samarth, and D. D. Awschalom, Phys. Rev. B **74**, 155203 (2006).

[OHan 00] R. C. O'Handley, John Wiley and Sons, New York (2000).

[Ohno 98] H. Ohno, Science **281**, 951 (1998).

[Olej 08] K. Olejník, M. H. S. Owen, V. Novák, J. Mašek, A. C. Irvine, J. Wunderlich, and T. Jungwirth, arXiv:0802.2080v1 (2008).

[Over 08] M. Overby, A. Chernyshov, L. P. Rokhinson, X. Liu, and J. K. Furdyna, Appl. Phys. Lett. **92**, 192501 (2008).

[Papp 06] K. Pappert, M. J. Schmidt, S. Hümpfner, C. Rüster, G. M. Schott, K. Brunner, C. Gould, G. Schmidt, and L. W. Molenkamp, Phys. Rev. Lett. **97**, 186402 (2006).

[Papp 07] K. Pappert, S. Hümpfner, J. Wenisch, K. Brunner, C. Gould, G. Schmidt, and L. W. Molenkamp, Appl. Phys. Lett. **90**, 062109 (2007).

[Papp 07b] K. Pappert, *Anisotropies in (Ga,Mn)As*, Dissertation, Universität Würzburg (2007).

[Papp 07c] K. Pappert, C. Gould, M. Sawicki, J. Wenisch, K. Brunner, G. Schmidt, and L. W. Molenkamp, New J. Phys. **9**, 354 (2007).

[Papp 07d] K. Pappert, S. Hümpfner, C. Gould, J. Wenisch, K. Brunner, G. Schmidt, and L. W. Molenkamp, Nature Physics **3**, 573 (2007).

[Pota 01] S. J. Potashnik, K. C. Ku, S. H. Chun, J. J. Berry, N. Samarth, and P. Schiffer, Appl. Phys. Lett. **79**, 1495 (2001).

[Reß 98] H. R. Reß, *Neue Messmethoden in der hochauflösendnen Röntgendiffraktometrie*, Dissertation, Universität Würzburg (1998).

[Rüst 03] C. Rüster, T. Borzenko, C. Gould, G. Schmidt, L. W. Molenkamp, X. Liu, T. J. Wojtowicz, J. K. Furdyna, Z. G. Yu, and M. E. Flatté, Phys. Rev. Lett. **91**, 216602 (2003).

[Rüst 05] C. Rüster, C. Gould, T. Jungwirth, J. Sinova, G. M. Schott, R. Giraud, K. Brunner, G. Schmidt, and L. W. Molenkamp, Phys. Rev. Lett. **94**, 027203 (2005).

[Sawi 04] M. Sawicki, F. Matsukura, A. Idziaszek, T. Dietl, G. M. Schott, C. Rüster, C. Gould, G. Karczewski, G. Schmidt, and L. W. Molenkamp, Phys. Rev. B **70**, 245325 (2004).

[Schm 08] B. Schmid, A. Müller, M. Sing, R. Claessen, J. Wenisch, C. Gould, K. Brunner, L. W. Molenkamp, and W. Drube, submitted to Phys. Rev. B (2008).

[Schm 06] M. Schmidt, *Electronic and Magnetic Properties of Bound Hole States in (Ga,Mn)As*, Diplomarbeit, Universität Würzburg (2006).

[Scho 01] G. M. Schott, W. Faschinger, and L. W. Molenkamp, Appl. Phys. Lett. **79**, 1807 (2001).

[Scho 03] G. M. Schott, G. Schmidt, L. W. Molenkamp, R. Jakiela, A. Barcz, and G. Karczewski, Appl. Phys. Lett. **82**, 4678 (2003).

[Scho 04] G. M. Schott, *Molekularstrahlepitaxie und Charakterisierung von (Ga,Mn)As Halbleiterschichten*, Dissertation, Universität Würzburg (2004).

[Schu 04] C. Schumacher, A. S. Bader, T. Schallenberg, N. Schwarz, W. Faschinger, L. W. Molenkamp, and R. B. Neder, J. Appl. Phys. **95**, 5494 (2004).

[Shen 97] A. Shen, Y. Horikoshi, H. Ohno, and S. P. Guo, Appl. Phys. Lett. **71**, 1540 (1997).

[Tang 03] H. X. Tang, R. K. Kawakami, D. D. Awschalom, and M. L. Roukes, Phys. Rev. Lett. **90**, 107201 (2003).

[Thei 03] T. N. Theis and P. M. Horn, Phys. Today **56**, 44 (2003).

[Vurg 01] I. Vurgaftman, J. R. Meyer, and L. R. Ram-Mohan, J. Appl. Phys. **89**, 5815 (2001).

[Wang 05] K. Wang, M. Sawicki, K. Edmonds, R. Campion, S. Maat, C. Foxon, B. Gallagher, and T. Dietl, Phys. Rev. Lett. **95**, 217204 (2005).

[Welp 03] U. Welp, V. Vlasko-Vlasov, X. Liu, J. Furdyna, and T. Wojtowicz, Phys. Rev. Lett. **90**, 167206 (2003).

[Welp 04] U. Welp, V. K. Vlasko-Vlasov, M. Menzel, H. D. You, X. Liu, J. K. Furdyna, and T. Wojtowicz, Appl. Phys. Lett. **85**, 260 (2004).

[Weni 07] J. Wenisch, C. Gould, L. Ebel, J. Storz, K. Pappert, M.J. Schmidt, C. Kumpf, G. Schmidt, K. Brunner, and L.W. Molenkamp, Phys. Rev. Lett. **99**, 077201 (2007).

[West 60] F. G. West, Nature **188**, 129 (1960).

[Wund 06] J. Wunderlich, T. Jungwirth, B. Kaestner, A. C. Irvine, A. B. Shick, N. Stone, K.-Y. Wang, U. Rana, A. D. Giddings, C. T. Foxon, R. P. Campion, D. A. Williams, and B. L. Gallagher, Phys. Rev. Lett. **97**, 077201 (2006).

[Xian 05] G. Xiang, A. W. Holleitner, B. L. Sheu, F. M. Mendoza, O. Maksimov, M. B. Stone, P. Schiffer, D. D. Awschalom, and N. Samarth, Phys. Rev. B **71**, 1307 (2005).

Publications

- **J. Wenisch**, C. Gould, L. Ebel, J. Storz, K. Pappert, M. J. Schmidt, C. Kumpf, G. Schmidt, K. Brunner, and L. W. Molenkamp, *Control of Magnetic Anisotropy in (Ga,Mn)As by Lithography-Induced Strain Relaxation*, Phys. Rev. Lett. **99**, 077201 (2007).

- **J. Wenisch**, L. Ebel, C. Gould, G. Schmidt, L. W. Molenkamp, and K. Brunner, *Epitaxial GaMnAs layers and nanostructures with anisotropy in structural and magnetic properties*, J. Cryst. Growth **301-302** 638-641 (2007).

- K. Pappert, S. Hümpfner, C. Gould, **J. Wenisch**, K. Brunner, G. Schmidt, and L. W. Molenkamp, *A non-volatile-memory device on the basis of engineered anisotropies in (Ga,Mn)As*, Nature Physics **3**, 573 (2007).

- K. Pappert, S. Hümpfner, **J. Wenisch**, K. Brunner, C. Gould, G. Schmidt, and L. W. Molenkamp, *Transport Characterization of the Magnetic Anisotropy of (Ga,Mn)As*, Appl. Phys. Lett. **90**, 062109 (2007).

- S. Hümpfner , K. Pappert, **J. Wenisch**, K. Brunner, C. Gould, G. Schmidt, and L. W. Molenkamp, *Lithographic Engineering of Anisotropies in (Ga,Mn)As*, Appl. Phys. Lett. **90**, 102102 (2007).

- K. Pappert, C. Gould, M. Sawicki, **J. Wenisch**, K. Brunner, G. Schmidt, and L. W. Molenkamp, *Detailed transport investigation of the magnetic anisotropy of (Ga,Mn)As*, New J. Phys. **9**, 354 (2007).

- M. Ghali, T. Kuemmell, R. Arians, **J. Wenisch**, S. Mahapatra, K. Brunner, and G. Bacher, *Electrical manipulation of spin injection into single InAs quantum dots*, Journal of Superconductivity and Novel Magnetism **20**, 413-416 (2007).

- M. Ghali, R. Arians, T. Kuemmell, G. Bacher, **J. Wenisch**, S. Mahapatra, and K. Brunner, *Spin injection into a single self-assembled quantum dot in a p-i-n II-VI/III-V structure*, Appl. Phys. Lett. **90**, 093110 (2007).

- C. Gould, S. Mark, K. Pappert, R. G. Dengel, **J. Wenisch**, R. P. Campion, A. W. Rushforth, D. Chiba, Z. Li, X. Liu, W. Van Roy, H. Ohno, J. K. Furdyna, B. Gallagher, K. Brunner, G. Schmidt, and L. W. Molenkamp, *An extensive comparison of anisotropies in MBE grown (Ga,Mn)As material*, New J. Phys. **10**, 055007 (2008).

- R. G. Dengel, C. Gould, **J. Wenisch**, K. Brunner, G. Schmidt, and L. W. Molenkamp, *Lateral magnetic anisotropy superlattice out of a single (Ga,Mn)As layer*, New J. Phys. **10**, 073001 (2008).

- B. Schmid, A. Müller, M. Sing, R. Claessen, **J. Wenisch**, C. Gould, K. Brunner, L. W. Molenkamp, and W. Drube, *Surface segregation of interstitial manganese in $Ga_{1-x}Mn_xAs$ studied by hard X-ray photoemission spectroscopy*, Phys. Rev. B **78**, 075319 (2008).

- M. Ghali, T. Kuemmell, **J. Wenisch**, K. Brunner, and G. Bacher, *Electrical charging of a single quantum dot by a spin polarized electron*, Appl. Phys. Lett. **93**, 073107 (2008).

Acknowledgements

Lebenslauf

Jan Wenisch

geboren in Würzburg am 10. Mai 1980

09/86 – 03/88	Besuch der Grundschule Estenfeld
04/88 – 07/90	Besuch der Grundschule Gerbrunn
09/90 – 06/99	Besuch des Deutschhaus-Gymnasiums in Würzburg Abschluss: Abitur
09/99 – 09/00	Zivildienst beim Bayerischen Roten Kreuz, Kreisverband Würzburg
11/00 – 08/03	Studium Physik (Diplom), Julius-Maximilians-Universität Würzburg
08/03 – 08/04	Studium Physik (Master of Science), University at Albany, State University of New York, USA Abschluss: Master of Science (Physics)
seit 11/04	Promotionsstudium am Lehrstuhl EP3 der Julius-Maximilians-Universität Würzburg Betreuer: Prof. K. Brunner